Vortex-Assisted Mixing in Microscale Flows

A Thesis Submitted
In Partial Fulfilment of the Requirements
for the Degree of

DOCTOR OF PHILOSOPHY

by

Dhananjay Kumar
(206103011)

Department of Mechanical Engineering
Indian Institute of Technology Guwahati
Guwahati - 781039, India
December 2024

भारतीय प्रौद्योगिकी संस्थान गुवाहाटी
Indian Institute of Technology Guwahati

Department of Mechanical Engineering, Indian Institute of Technology Guwahati, Guwahati - 781039, India.

Declaration

I hereby certify that the information reported in the dissertation “**Vortex-Assisted Mixing in Microscale Flows**” is entirely my own research, performed under the guidance of Dr. Pranab Kumar Mondal. Any part of this work has not earlier been submitted for the award of any degree, diploma, associate-ship, fellowship or its equivalent to any University or Institution. I have not violated any copyright and plagiarism law. All text and figures are my own.

5th December 2024

Dhananjay Kumar
Roll No. 206103011
Department of Mechanical Engineering,
Indian Institute of Technology Guwahati,
Guwahati – 781039, Assam,
India.

Department of Mechanical Engineering, Indian Institute of Technology Guwahati, Guwahati - 781039, India.

Certificate

It is certified that the work contained in this thesis entitled **"Vortex-Assisted Mixing in Microscale Flows"** submitted by Dhananjay Kumar to the Indian Institute of Technology Guwahati for the award of the degree of Doctor of Philosophy has been carried out under my supervision in the Department of Mechanical Engineering, Indian Institute of Technology Guwahati. This work has not been submitted elsewhere for the award of any other degree or diploma.

5th December 2024

Dr. Pranab Kumar Mondal
Associate Professor
Department of Mechanical Engineering,
Indian Institute of Technology Guwahati,
Guwahati – 781039, Assam,
India.


भारतीय प्रौद्योगिकी संस्थान गुवाहाटी
Indian Institute of Technology Guwahati

To my family, especially my parents,

For their boundless love, unwavering support, and patience.

ACKNOWLEDGEMENT

I would like to take this opportunity to extend my heartfelt gratitude to many individuals who provided invaluable assistance during my doctoral studies at IIT Guwahati. I am truly grateful for their unwavering support and guidance throughout the various stages of my research endeavors.

Important of all, I want to express my deepest and most sincere gratitude to my supervisor, Dr. Pranab Kumar Mondal, for his invaluable guidance, inspiration, and timely advice. Working with him was a privilege, engaging in discussions on various academic and non-academic subjects, and collaborating on diverse problems and methodologies. The multitude of ideas and concepts he shared acted as true catalysts, accelerating my research progress and contributing to the development of this distinctive dissertation. I am confident that the incorporated solution methodologies, diverse concepts, and non-intuitive insights presented in this dissertation meticulously reviewed by him will resonate scientifically and garner recognition from professionals in the field. Additionally, I would like to express my utmost gratitude to my doctoral committee members, namely Prof. Amaresh Dalal, Dr. Bhaskar Kumar, and Dr. Pankaj Mishra, for their valuable suggestions and for shedding light on various aspects that may have been unintentionally overlooked in my work. The research undertaken during my PhD journey served as a significant learning experience, and for that, I am indebted to Dr. P. Kaushik (Formerly, Department of Mechanical Engineering, NIT Trichy) for their guidance in clarifying doubts, addressing questions, and resolving ambiguities. Additionally, I would like to acknowledge the support of the Prime Minister Research Fellowship (PMRF) from the Ministry of Education, Government of India, which enabled me to carry out this research work.

I extend my gratitude to my lab (Microfluidic and Microscale Transport Processes Lab) seniors, batchmates, and juniors for their unwavering support and motivation, both in my work and personal challenges. Throughout these years, the memories of hostel life have been enriched by the camaraderie with close friends such as Pankaj Kumar, Sudhanshu Singh, Sunit Sarkar, Harshal Srivastava, and Udit Sharma, among others. Additionally, I would like to express my thanks to Dr. Harsad Gaikwad (PhD, IIT Guwahati, Alexander von Humboldt Fellow, Bayreuth, Bavaria, Germany) and Dr. Sumit Kumar Mehta (Department of Mechanical Engineering, PhD, NIT Silcher, NPDF, IIT Guwahati, India) for their valuable contributions to the analysis conducted for Chapter 1 and Chapter 4 of this dissertation.

Most importantly, I express profound gratitude to my family for their understanding of my dedication to this work and for willingly sacrificing their demands on my time. None of my accomplishments would have been possible without their unwavering love and patience. I am forever thankful for their consistent presence as a source of love, concern, support, and strength throughout these years.

Dhananjay Kumar

Abstract

Microscale mixing in fluidic devices offers several advantages, including reduced sample volume, portability, cost-effectiveness, safe handling of hazardous materials, compact size, and biodegradability. Efficient mixing is crucial for various microfluidic processes, particularly in biochemical and medical diagnostics. Several studies investigated in this thesis focus on enhancing vortex-assisted mixing in microfluidic devices through both passive and active approaches. The challenge lies in achieving efficient mixing in the confined space of microfluidic/nanofluidic pathways, which has led to exploring secondary flows to boost advection over molecular diffusion. This involves implementing passive methods, such as introducing inlet swirl, and active methods, like applying an external electrical field, all within the constraints of a narrow-fluidic channel. The dissertation outlines objectives and analyzes each application in detail across respective chapters.

The first problem explores the mixing of constituent components in a narrow fluidic cylindrical channel under swirling flow conditions. The analytical solution for the flow field, obtained through the separation of variables method, is validated using numerical simulations. The swirl velocity profile, dependent on Reynolds number (Re), shows exponential decay along the channel length. Numerical solutions for the species transport equation, considering Peclet numbers ranging from 10^2 to 10^4, are coupled with the swirl velocity for $0.1 \le \mathrm{Re} \le 100$. Increasing Reynolds number induces complete fluid rotation, resulting in engulfment flow and significantly enhancing mixing efficiency. Continuing from our prior study of the second problem, we introduce a tangential (swirl) velocity at the inlet to facilitate effective mixing of inelastic non-Newtonian fluids or solutes at the outlet. This consideration incorporates the non-linear viscous effects inherent in shear-thinning and shear-thickening fluids, utilizing the power-law model. Through numerical solutions of the species transport equation, coupled with the analytically determined swirl velocity, we illustrate that the combination of inlet swirl and shear-thinning fluid properties enhances advection-dominated mixing. Furthermore, higher Reynolds numbers contribute to increased advection dominance, resulting in engulfment flow, chaotic convection, and improved mixing efficiency.

The third problem explores the mixing of soft biofluids within a narrow fluidic device influenced by electroosmotic vortices generated by patterned soft polyelectrolyte

layers (PEL) that modulate the electrical double effect. We employ numerical solutions to the transport equations describing solute mixing in the chosen setup and assess the shear-induced kinetics of binary aggregation in the deployed soft matter system. The interplay of forces arising from fluid rheology and PEL's geometric parameters significantly impacts the size and strength of developed vortices, consequently affecting mixing strength in a non-trivial manner. Our investigation demonstrates that higher shear-thinning behavior of constituent components coupled with a larger extent of PEL structure results in enhanced solute mixing (>90%). Furthermore, we estimate the characteristic time of binary aggregation kinetics, crucial for analyzing the mixing of biofluids containing biomolecules, based on the parameters employed in this analysis. The results indicate that an increase in the shear-thinning behavior of solutes leads to a decrease in the characteristic time of binary aggregation kinetics.

In the fourth problem, we investigate non-Newtonian vortex characteristics in a microchannel influenced by a pH-sensitive polyelectrolyte layer (PEL) modulated electroosmotic effects. Using a finite element method-based numerical solver, the developed mathematical framework considers the impact of solution bulk pH (pH_b) and ionic concentration on zeta potential. Across varying pH_b and rheological parameters, the analysis covers PEL space charge density, net body force, and flow patterns. The study reveals that distinct net electrical body force patterns lead to specific flow structures, influencing flow rate and mixing efficiency. Protonic exchange dominance in basic and acidic PEL groups results in pH-dependent net electrical body force, influencing vortex direction and flow rates. Different flow pattern regimes emerge with pH_b ranging from 3 to 11. At pH_b around 4, mixing efficiency is nearly 100% at lower Carreau numbers, exceeding 90% for higher diffusive Peclet numbers in highly acidic liquids. These findings hold significant implications for designing microfluidic/nanofluidic devices for specific pH_b values in mixing and transporting non-Newtonian liquids.

List of Abbreviations and Symbols

Abbreviations

CFD	Computational Fluid Dynamics
DH	Debye-Hückel
DNA	Deoxyribonucleic Acid
EDL	Electric Double Layer
EOF	Electroosmotic Flow
FVM	Finite Volume Method
GCI	Grid Convergence Index
LOC	Lab-on-a-Chip
MP	Mixing Performance
NP	Nernst-Planck
NS	Navier-Stokes
PB	Poisson-Boltzmann
PEL	Polyelectrolyte Layer
pH	Potential of Hydrogen
pH_b	Bulk solution pH
PL	Polymeric Layer
RBC	Red Blood Corpuscle
TMSC	Micro T-Mixer with Swirl-Inducing Inlets and a Rectangular Constriction
μTAS	Micro Total Analysis Systems

Latin symbols

a_i	Coefficients of strength of convection- diffusion
$C \in C_{A,B,1,2}$	Concentration of the uncharged species or liquid (A or B or 1or 2)

C_0	Concentration of the uncharged species in unmixed state
C_∞	Concentration of the uncharged species in the mixed state
Cu	Carreau number
D	Ionic diffusion coefficient of the electrolyte ions
$\mathbf{D}$	Deformation rate tensor or strain-rate tensor
D_0	Molecular Diffusion Coefficient of the Constituent Species
d_p or t_p	Thickness of polyelectrolyte layer
E or E_{ref}	Reference electric field
e	Charge of an electron
F	Faraday’s constant
F_d	Darcy’s frictional drag force
H	Micromixer half height
K_A or K_B	Equilibrium constants
L	Characteristic length scale
L_p	PEL patch length
n	Non-Newtonian fluid behavior power-law index or flow- behavior index according to Carreau model
N_A	Avogadro’s constant
(n_r, n_θ, n_z)	Number of grid points in the r, θ and z direction, respectively Number
p	Fluid pressure
Pe_I	Ionic Peclet number
Pe	Peclet number
R	Characteristics radius of cylindrical channel domain
Re	Reynolds number
(r, θ, z)	Location in cylindrical system
r_t	Transition radius (forced to free vortex)
S	Swirl number

$S(z)/S(0)$	Swirl intensity
T	Absolute temperature
t_c	Characteristic time for shear-induced binary aggregation kinetics
$\mathbf{u}=(u_r, u_\theta, u_z)$	Velocity field in the cylindrical channel domain
$\mathbf{u}=(u, v, w)$	Velocity field in the rectangular channel domain
u_{av}	Average axial flow velocity at the inlet of the channel
u_{HS}	Helmholtz-Smoluchowaski velocity
(V, W, U)	Non-dimensional velocity scale in cylindrical channel domain w.r.t (r, θ, z) directions.
(x, y, z)	Location in cartesian coordinate system
z_i	Valency of ions

Subscripts

p	Polyelectrolyte layer
ref	Reference

Greek symbols

σ_{PEL}	pH-tunable space charge density of the polyelectrolyte
ε_0	Electrical permittivity of the free space
ε_r	Relative permittivity of the electrolyte
$\varepsilon_{r,p}$	Relative permittivity of the polyelectrolyte
$\overline{\eta}(\dot{\gamma})$	Apparent viscosity for Carreau model
η_m or η	Mixing efficiency
η_{rm}	Relative Mixing efficiency

$\dot{\gamma}$	Second invariant of rate of deformation tensor for Carreau model
Γ_A or Γ_B	Number of polyelectrolyte group per nm^2
κ	Debye-Hückel parameter of electrolyte layer
κ_p	Debye-Hückel parameter of polyelectrolyte layer
λ	Time parameter for Carreau model
$\lambda_{i=n,m}$	Eigen values
μ_e	Effective/Apparent viscosity of the fluid in case of power-law model
μ_{eo}	Electroosmotic mobility
μ_0	Flow consistency index in case of power-law model or zero shear rate viscosity for Carreau model
$\bar{\mu}_\infty$	Infinity shear rate viscosity for Carreau model
Φ	Applied external electric potential field
ρ	Density of the fluid or electrolyte
$\mathbf{S}$	Strain rate tensor
Ψ	Induced electrostatic potential field
Ψ_{ref} or ζ	Reference EDL potential or Zeta potential
Θ_ε	Ratio of relative permittivity of polyelectrolyte to electrolyte
$\boldsymbol{\tau}_{ij}$	Deviatoric stress tensor
$\varpi = \Phi_{ref}/\Psi_{ref}$	Ratio of reference external potential to the reference EDL potential

Contents

List of Figures

List of Tables

CHAPTER 1

Introduction and Literature Review

1.1 Microfluidics Overview

The remarkable progress in the fabrication and utilization of micro-electro-mechanical systems (MEMS) in the last decade has surpassed our understanding of the unconventional physics that govern the operation and production of small devices (Gad-el-Hak, 1999). A thorough comprehension of these physics is essential for designing, optimizing, fabricating, and operating improved MEMS devices. MEMS devices are characterized by their sizes, which are less than 1 mm but greater than 1 micron, and they integrate electrical and mechanical components manufactured using integrated circuit batch-processing technologies. The emergence of a novel field and a broad range of applications, termed "microfluidics", has been driven by the necessity to comprehend flow characteristics at this newly defined length scale. Microfluidics involves studying fluids, whether liquid or gas confined within microscale dimensions, typically within microchannels (P. Tabeling, 2007). The versatility of utilizing the microscale comes from its numerous advantages over the traditional macroscale. These benefits encompass - cost-effectiveness (Stone et al., 2004), portability (Tian and Finehout, 2008), minimal sample consumption (Burns et al., 1998; Atencia and Beebe, 2005), rapid analysis (Chou et al., 1999), and the ability to explore physical, chemical, and biological analyses, incorporating flow metering, mixing, reactions, separation processes, and detection, as

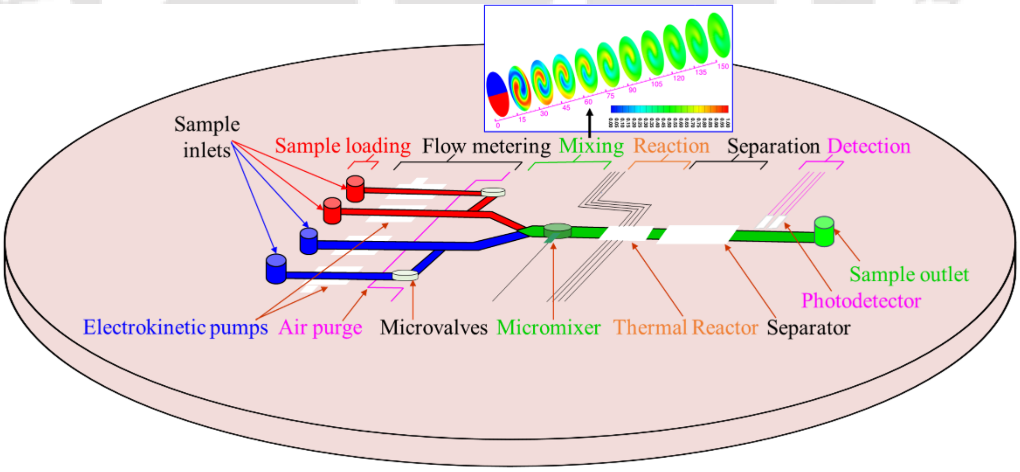

Figure 1.1: Schematic showing an integrated laboratory-on-a-chip system designed for conducting miniaturized biological and chemical analysis facilitating flow metering, mixing, reactions, separation processes, and detection in a scaled-down format.

illustrated in Fig. 1.1 (Sammarco and Burns, 1999; Losey et al., 2001). While the applications of microfluidic devices vary widely, they commonly require efficient mixing, as shown in Fig. 1.1, which is a crucial stage in numerous microfluidic processes (Chang and Yeo, 2010).

1.2 Micromixing Overview

Mixing in microfluidic devices is the process of achieving uniform concentration when different concentrations of fluid flow through a channel, whether as single or multiple components. This phenomenon is familiar in our daily lives; when we combine two or more liquids, we naturally stir them, a seemingly simple process. The need for mixing arises in diverse scenarios, such as homogenizing solutions during chemical reactions (Stroock et al., 2002), blending solutions containing macromolecules like Deoxyribonucleic acid (DNA) (Burns et al., 1998; Ottino and Wiggins, 2004), and combining different liquid samples containing enzymes and proteins in biological processes (Beebe et al., 2002; Hessel et al., 2005; Harnett et al., 2008). In microdevices, efficient mixing is essential due to their small scale. It is vital for various applications, ensuring uniformity and enhancing the performance of processes such as chemical reactions, analyses, and other fluid-based functionalities (Stroock et al., 2002). Microdevices enable the manipulation of small sample quantities, particularly when dealing with expensive, hazardous, or limited materials, such as DNA (DeMello, 2006). Additionally, microdevices demonstrate the capability for high-quality separation and swift detection processes, reducing analysis time. Their compact size, portability, and disposability further enhance their appeal. Moreover, microfluidic devices, including micromixer devices, can be seamlessly integrated with other processes within a single device (Whitesides, 2006; Streets and Huang, 2013). These collective advantages underscore the significance of developing microfluidic devices for practical applications. However, to fully harness these benefits, it is imperative to design efficient devices with effective processes, including the crucial aspect of mixing, as previously established (Jensen, 1998).

The primary objective of this project is to enhance mixing in microfluidic devices using both passive and active approaches. This involves introducing inlet swirl and applying an external electrical field to stir the fluid, creating chaos perpendicular to the flow direction in a narrow-fluidic channel. The goal is to achieve vortex-assisted convective mixing in a short length. The ongoing discussion includes a comprehensive literature review highlighting the latest advancements and benchmarks in these applications. As we conclude this chapter, a concise overview will be provided, summarizing the objectives and organizational structure of the thesis.

1.2.1 A Brief Review of the Inlet Swirl

Swirl is characterized as the movement of bulk fluid in a twisting or spiraling pattern, often represented by the tangential velocity component upon entry into a pipe as shown in Fig. 1.2 (Greitzer et al., 2007; Sheikholeslami et al., 2015). In microchannel-based fluid flow devices, particularly in small channels and tubes, understanding the transport properties is crucial. The introduction of swirl is a traditional method to enhance transport in tubes, with applications in devices such as cyclones for solid-liquid-gas separation, geophysical flows such as tornadoes, swirl atomizers, swirl combustion devices, and heat and mass transfer enhancement (Hay and West, 1975; Pati et al., 2013; Chan et al., 2019). Typically, swirling or rotating flows in engineering applications are axisymmetric and can be studied without considering the azimuthal direction (Greitzer et al., 2007). While swirl flows are typically observed in straight pipes, managing the decay of swirl along the pipe's length presents a challenge (Shtern, 2018). This challenge arises from the intricate interplay between vortex breakdown and flow stability, including the re-stabilization of the flow as the Reynolds number increases, leading to the formation of a vortex breakdown region (Chan et al., 2019). In the vortex T-mixer design (Ansari et al., 2012; Balasubramaniam et al., 2017), both inflows enter the outlet channel tangentially, generating a swirling flow characterized by a predominant vortex structure that diminishes downstream in the outlet channel. This decay is primarily attributed to wall effects, including friction between the pipe wall and fluid, as well as the viscosity of the fluid. Maintaining sufficient swirl intensity is essential for applications requiring enhanced fluid transport and increased heat transfer rates (Yu and Kitoh, 1994; Shtern, 2018; Kumar et al., 2020).

Regarding this aspect, there is a considerable number of literature available on the utilization of swirling flow for transport, particularly documented in the 1900s for macroscale systems. In the early 1950, Talbot (1954) conducted both theoretical and experimental investigations on laminar swirling flows by introducing swirl into a cylindrical duct with superimposed Poiseuille flow. Talbot employed the perturbation

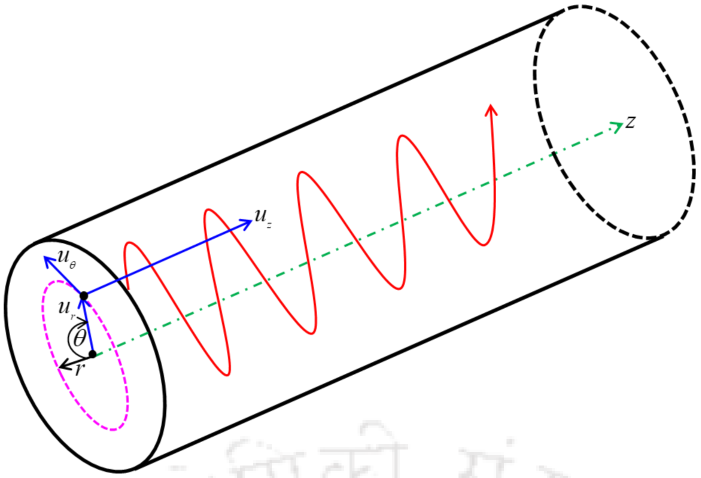

Figure 1.2: Schematic showing the pipe's swirling flow(Greitzer, Tan and Graf, 2007; Shtern, 2018) with in a cylindrical coordinate system (r, θ, z) having radial (u_r), azimuthal (u_θ), and tangential (u_z) velocity components, respectively.

- method to address radial velocity components, and his experimental findings demonstrated good agreement with the theoretically predicted swirl decay rates. Further, Kreith and Sonju, (1965) determined the decay of swirl in fully developed turbulent flow in a pipe through their analytical solution. The analytical results, while neglecting axial diffusion terms contributed by a swirl velocity, were the first to showcase the swirl's dependence on Reynolds number and axial location, to the best of our knowledge. Researchers employed both numerical (Kiya et al., 1971) and experimental (Kitoh, 1991) methods to analyse swirl flow in both laminar and turbulent conditions. They observed the downstream decay of swirl, attributed to wall friction, referred to as swirl intensity. This intensity was found to exhibit an exponential decrease along the flow downstream. The swirl velocity profile was segmented into core, annular, and wall regions, revealing a combination of forced and free vortex behaviors (Reader-Harris, 1994). The researchers also established that the rates of swirl decay are directly proportional to the friction factor, swirl intensity, and Reynolds number (Yu and Kitoh, 1994; Parchen and Steenbergen, 1998; Bali, 1998). In recent publications, researchers have employed curve-fitting techniques to derive a comprehensive swirl decay equation for laminar flow in pipes (Ayinde, 2010). Yao and Fang (2012) presented the most generalized analytical expression for swirl decay in laminar flow pipes, addressing three different cases: swirl (using Rankine vortex) superimposed with parabolic flow, slug flow, and slug flow with diffusion (Greitzer et al., 2007; Shtern, 2018). The resulting analytical expression for the swirl velocity profile depends on parameters such as Reynolds number, pipe axial distance, transition radius, and swirl intensity. In a prior study, Kumar et al., (2020) conducted an analytical investigation of swirl flow in a microtube under slip conditions by superimposing the Rankine vortex (Parchen and Steenbergen, 1998) with the parabolic flow. Their findings indicated that slip conditions enhance swirl effects by delaying the decay rate, consistent with the parameters considered by Yao and Fang, (2012) in their analysis.

In the design of devices, particularly micro-scale ones like micromixers, micro-separators, and micro-combustors, swirl plays a crucial role (Hay and West, 1975; Greitzer et al., 2007; Shtern, 2018). These microscale devices, with tube diameters in the micron range, exhibit low Reynolds numbers and laminar flow. To promote mixing in such scenarios, the introduction of swirl components in velocity becomes imperative. Swirl-induced micromixing plays a significant role in microfluidic systems, where precise control over small fluid volumes is essential. Its application extends to various fields, including Lab-on-a-Chip (LOC) devices, biomedical diagnostics, DNA analysis and sequencing, point-of-care testing, as well as a diverse range of applications in healthcare, chemistry, and environmental monitoring (Cortes-Quiroz et al., 2010; Matsunaga and Nishino, 2014; Cortes-Quiroz et al., 2014; Cortes-Quiroz et al., 2017; Zhang and Luo, 2018).

1.2.2 A Brief Review of electric double layer and Electrokinetic Phenomena

When a solid surface, such as glass or fused silica, comes into contact with an electrolytic solution, it undergoes charging due to the dissociation of protonated carboxylate groups (Masliyah and Bhattacharjee, 2006). This results in the formation of a charged layer at the surface, with hydrated counterions from the electrolytic solution being adsorbed, creating a layer of approximately 0.1 nm thickness known as the Stern layer (Karniadakis et al., 2005). Beyond the Stern layer, ions become mobile and move within the fluid, influenced by thermal energy and electric attraction, forming what is referred to as the diffused layer. Together, the Stern and diffused layers constitute the electric double layer (EDL). Within the EDL, electrolytes segregate into two categories: coions, carrying the same charge as the charged surface, and counterions, carrying the opposite charge. The term ‘electric double layer’ arises from the presence of two sublayers: the Stern layer containing immobile counterions and the Gouy-Chapman layer (or diffuse layer) encompassing mobile counterions (Hunter, 1981; Masliyah and Bhattacharjee, 2006). Figure 1.3 illustrates a typical EDL formed on the charged surface, depicting the Stern layer surrounding immobile counterions and the diffuse layer enveloping mobile counterions. Far from the Stern layer, the zeta potential decreases to zero as the density of counterions approaches zero. In this state of electroneutrality, counterions coexist with coions, defining the region known as the electroneutral region. The electric double layer (EDL) initiates from the charged surface and dissipates near the electroneutral region. For steady-state, the ionic distribution in EDL, neglecting the finite size ions, can be obtained from the solution of the Nernst–Planck equation given as (Karniadakis et al., 2005):

$$-\vec{\nabla}\cdot\left(D_{i\pm}\vec{\nabla}n_{\pm}+\frac{D_{i\pm}}{RT}z_{\pm}Fn_{\pm}\vec{\nabla}\psi\right)+\vec{\mathbf{u}}\cdot\vec{\nabla}n_{\pm}=0 \tag{1.1}$$

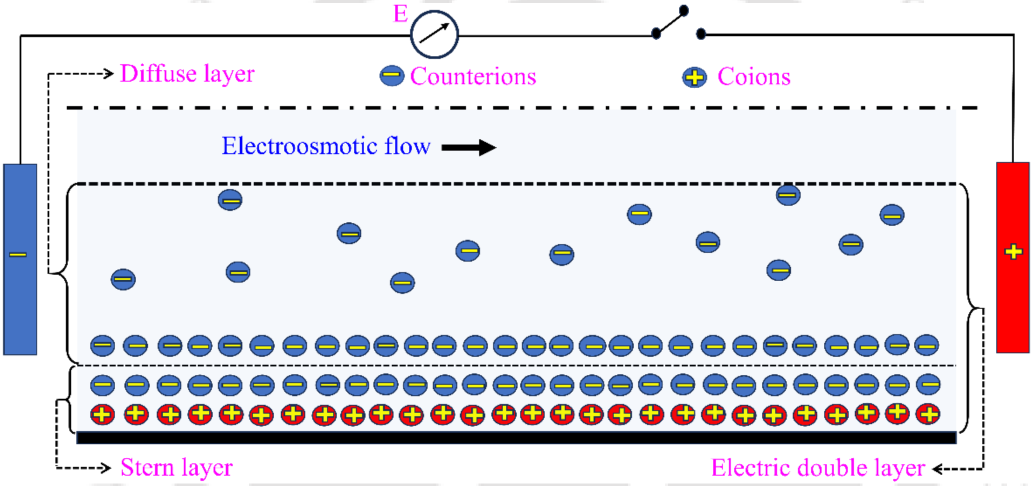

Figure 1.3: Schematic showing the working principle of the electroosmotic flow generation phenomenon.

In this context, the symbols $z_{\pm}$, $D_{i\pm}$, R, T, ε, ψ, F, n_{+} and n_{-} represent the valency of ions, ionic diffusion coefficients, universal gas constant, absolute reference temperature, electrical permittivity of the medium, EDL potential, Faraday constant, and ionic concentration of counterions and coions, respectively. Neglecting convective effects, the distribution of ions conforms to the Boltzmann distribution, expressed as follows (Karniadakis et al., 2005):

$$n_{\pm}=n_{o}\exp\left(\mp\frac{z_{\pm}e\psi}{k_{B}T}\right) \tag{1.2}$$

Here, n_{o}, e, and k_{B} represent the bulk ionic concentration, the charge on a single electron, and the Boltzmann constant, respectively. It's important to note that the classical Poisson-Boltzmann distribution of ions remains applicable in scenarios of dilute solutions and negligible ion size. Nevertheless, in cases where the surface charge density is substantial and the channel's characteristic length scale is minimal, the hydrated ions' length scale might become comparable to the channel dimension (Storey et al., 2008). Assuming negligible ion convection, the Boltzmann analogy can be employed to determine the distribution of both counterions and coions within the specified bounds of the EDL (Hunter, 1981; Masliyah and Bhattacharjee, 2006).

Electrokinetic phenomena occur when efforts are made to mobilize counterions within the electric double layer, particularly in the diffuse layer (Masliyah and Bhattacharjee, 2006). The two commonly used methods to induce counterion motion involve externally applied electric fields and pressure gradients across the channel. While both mechanisms facilitate the movement of counterions through the channel, they result in distinct consequences.

Electroosmotic flow is induced by applying an external electric field across the channel, which generates a Lorentz force proportional to the field strength. This force mobilizes counterions from the electric double layer, especially the diffuse layer. The hydrodynamic resistance, influenced by fluid viscosity, causes the ions to diffuse towards the bulk of the fluid, resulting in a net flow of the fluid through the channel. By adjusting the applied field, one can control the movement of counterions and thus the direction of flow. This phenomenon, commonly referred to as electroosmotic flow or EOF (Masliyah and Bhattacharjee, 2006), is extensively utilized in bio micro-electro-mechanical systems (MEMS) to enhance flow control in applications such as mixing, separation, and pumping small liquid samples (Aboelkassem, 2023). Electroosmotic flow in microfluidic channels is favored over pressure-driven flow due to its noise-free operation, lack of moving parts, portability, and integrability (Nguyen and Wu, 2005; Hessel et al., 2005). The schematic representation of the working principles of electroosmotic flow is illustrated in Fig. 1.3.

1.2.3 Limitations and Solutions of the Electrokinetic Phenomena

Researchers have reshaped the conventional operational principles of various applications through electrokinetic phenomena. However, the escalating demands for cutting-edge applications and microscale systems necessitate significant modifications in these principles. Specifically, when referring to “intrinsic aspects,” we highlight the “electric double layer” (EDL) and its formation method. The typical approach to EDL formation, commonly utilized in electrokinetic phenomena, faces limitations, including restricted flow controllability and a lack of bio-lubrication effects. Addressing these limitations individually to achieve optimal functionality in modern applications requires straightforward solutions. However, integrating these aspects into a single analytical domain remains challenging unless considering grafted polyelectrolyte layers as an option. In this context, we propose the utilization of a soft polyelectrolyte layer as a viable solution to overcome the aforementioned limitations (Das et al., 2015).

It is crucial to highlight that the polyelectrolyte layer, with its protein-like structure, acts as a protective cushion for vital samples such as Deoxyribonucleic acid (DNA) or proteins. This protection helps prevent their degradation, a common issue in rigid narrow-fluidic channels. Due to this property, the polyelectrolyte layer has played a significant role in various biological and chemical applications, even beyond non-electrokinetic (Das et al., 2015). Recognizing this potential, there is an opportunity to explore the impact of these smart layers in electrokinetically assisted clinical and pathological applications. This includes their role in facilitating the transport of biofluids through rectangular narrow-fluidic channels and promoting the mixing of co-injected streams of biological or chemical species. This avenue of research holds promise for addressing current challenges and advancing the field.

The investigation into mixing is designed to establish practical design guidelines for effectively blending liquid samples in microfluidic devices. Additionally, the present work seeks to enhance understanding of vortex-assisted passive and active mixing techniques that have not been thoroughly explored. The subsequent section will provide concise introductions to the applications under analysis, outlining their working principles and highlighting prevalent drawbacks. To ensure a cohesive discussion, these introductions will be complemented by a comprehensive review of archived literature, encompassing recent developments in each application.

1.3 A Quick Overview of Archived Literature

In the previous section, we discussed the significance and potential practical applications of an efficient micromixer in microfluidics. However, achieving effective mixing in these devices poses challenges due to specific conditions associated with their length and time scale. In this chapter, we delve into the applications where the utilization of swirl inlet and polyelectrolyte layer (PEL) can enhance mixing to the desired level. We conducted a comprehensive literature review to understand recent advancements in both passive and active mixing approaches, with a specific focus on vortex-assisted methods. Because the applications we consider are diverse, the identified drawbacks and deficiencies vary for each. To streamline the presentation, we discuss the current attempts proposed to address the mixing challenges associated with each application. Finally, this chapter concludes with a summary of the literature review findings, contributing to a thorough understanding and the definition of research objectives.

1.3.1 Swirl Modulated Micromixing: Passive Approach

When a fluid surpasses a critical Reynolds number and experiences a sudden expansion in a conduit's cross-sectional area, it manifests local separation from the wall due to the adverse pressure gradient. This leads to the creation of a vortex pair that frames the entrance to the expansion (Alleborn et al., 1997). Modifying the geometry of the channel cross-section to create a vortex pair can generate a pronounced swirling flow structure, effectively enhancing fluid mixing (Huang et al., 2017). In the aspect of achieving effective mixing efficiency, various passive mixer have been developed, such as T, Y shaped channels, commonly referred to as planar mixers, as well as three-dimensional serpentine, Square wave mixer, Herringbone mixers etc. These mixers aim to enhance mixing efficiency through stretching, folding, and break-up processes (Wang et al., 2003; Nguyen and Wu, 2005).

In the realm of vortex-driven or swirl-driven passive micromixing, Engler et al., (2004) were pioneers in exploring mixing within a passive T-mixer. They introduced a classification system defining three distinct regimes in micromixers based on the Reynolds number: stratified flow (Re = 7), vortex flow (Re = 60), and engulfment flow (Re = 199). In the stratified flow regime, two fluids remain separated by a thin interface, resulting in poor mixing efficiency. Vortex flow is characterized by the formation of a counter vortex, while engulfment flow involves the entanglement of fluid species due to the presence of a strong vortex. Therefore, better mixing of liquid samples is achieved in this regime at higher Reynolds number. Experiments and numerical studies focusing on the mixing of liquid samples in a T-mixer at higher Reynolds numbers revealed that rapid mixing occurs at higher flow rates (Re > 400). This phenomenon can be attributed to the generation of vortices and secondary flows, responsible to enhance mixing efficiency

(Wong et al., 2004). A numerical modelling conducted by Jin et al., (2006) on the mixing of two fluids using a swirl micromixer, where the fluids involved in the mixing process were water and glycerol. The study classified mixing as cost-effective when the Reynolds number exceeded 500. Specifically, the considered Reynolds number of 1300 was identified as optimal for cost-effective mixing due to the enhanced generation of swirl flow, leading to an increased interface between the two fluids. One of the articles also corroborated the superior efficacy of three-dimensional (3D) passive mixers compared to planar passive micromixers. This is attributed to the 3D structure's ability to generate enhanced vortices and secondary flow. The study indicated that the engulfment regime was achieved at relatively lower Reynolds numbers (Re = 10 to 70) in the case of 3D passive mixers (Ansari et al., 2012). In the realm of passive micromixers, the focus on leveraging swirl for improved mixing has been underscored, with Matsunaga and Nishino, (2014) making a substantial contribution. This enhancement was particularly observed in micromixers with rectangular cross-sections and three-dimensional L-shaped structures featuring serpentine patterns. Through a numerical exploration of a T-mixer equipped with two protrusions in the inlet channels, they unveiled a remarkable mixing enhancement exceeding twice that of a typical T-mixer. This improvement can be traced back to the presence of obstacles in the inlet channels, which serve to narrow and redirect fluid streams, prompting them to enter the T-junction at varying vertical levels. The resulting intertwining of these streams gives rise to a vortex flow within the mixing channel. Their study spanned Reynolds numbers ranging from 20 to 150, revealing that the introduction of swirl in the inlet channels significantly enhances mixing efficiency. Cortes-Quiroz and colleagues (Cortes-Quiroz et al., 2010; Cortes-Quiroz et al., 2014; Cortes-Quiroz et al., 2017; Zhang and Luo, 2018) conducted a series of studies on 3D T-mixers, emphasizing their enhanced mixing capabilities. In the initial work (Cortes-Quiroz et al., 2010), they introduced a 3D T-mixer with unique features such as half-depth inlet channels and varied positioning, demonstrating improved mixing quality compared to planar-type T-mixers. Subsequent research (Cortes-Quiroz et al., 2014) confirmed significantly higher mixing levels in the 3D T-mixer over a typical T-mixer, with lower pressure drop and shear stress in the outlet channel within a Reynolds number range of 10–250. Further investigations (Cortes-Quiroz et al., 2017) explored the impact of the mixing channel's aspect ratio, revealing that widening the channel substantially improved mixing performance. The latest research by Zhang and Luo, (2018) introduced novel 3D micro T-mixers with swirl-inducing inlets and rectangular constriction (TMSC) to enhance fluid mixing. Numerical analysis showed that the TMSC design outperformed other micromixers across Reynolds numbers from 10 to 70, particularly at Re = 70, where the mixing index reached about 91.8%. This highlights the effectiveness of combining rectangular constriction and swirl-inducing inlets for achieving high mixing performance at a short distance. Huang et al., (2017) recently investigated micromixing in a specially designed microchannel aimed at inducing swirl, utilizing square and T-shaped cross sections. The modification of the channel cross-section aimed to create a robust swirl structure, enhancing fluid mixing. Computational simulations revealed efficient mixing at low Reynolds numbers (0.01–10), corresponding to mean velocities of 0.000081 to 0.081 m/s, with a hydrodynamic diameter of 120 μm. Balasubramaniam et al., (2017) investigated the enhancement of mixing performance in spiral micromixers with diverse cross-sectional geometries (trapezoidal, semi-circular, square, and rectangular) and varying hydraulic diameters. The formation of Dean vortices was experimentally observed along the micromixer length using confocal microscopy and compared with simulation results within the specified operating range of Reynolds number ($20 < Re < 277$). The study concluded that semi-circular and trapezoidal cross-section microchannels exhibited the highest mixing quality due to their enhanced swirling strength. Khaydarov et al., (2018) investigated flow regimes within micromixers employing a chicane mixing geometry. Computational Fluid Dynamics (CFD) modelling revealed two distinct effects during the convective mixing process: swirling and recirculation. The research observed that the convective mixing in vortex flow exhibited a considerable extent of combination comparable to that seen in stratified flow. Additionally, Dundi et al., (2021) introduced swirl velocity at entrances of T junction microchannels to enhance amalgamation. Numerical findings revealed that an inverse swirl orientation at entrances led to a quicker initiation of the engulfment regime, improving mixing in the Reynolds number range of 66 to 180. At Reynolds numbers exceeding 266, maintaining the same swirl orientation at entrances facilitated effective swapping of samples at the junction point, resulting in a substantial increase in mixing. In particular, the inverse swirl orientation showed a notable improvement of 300% to 500% in the mixing index within the Reynolds number range of 160 to 180. Conversely, the same swirl orientation demonstrated a 30% to 70% increase in the mixing index in the Reynolds number range of 266 to 372 when compared to a T junction without swirl. In a recent study, researchers investigated the mixing quality of fluids in a microchannel incorporating a cylindrical section with swirl flow (Lobasov et al., 2020). The results revealed that with a growing number of segments, there is a simultaneous increase in both mixing quality and pressure drop within the Reynolds number range of 1 to 300.

The preceding discussions highlight the substantial impact of vortex-induced phenomena in microchannels on mixing performance. It is imperative to emphasize that existing literature indicates a noteworthy observation: the influence of vortices along the microchannel diminishes as one progresses towards the middle section, thereby impacting the overall mixing efficiency of the channel. To delve into the intricacies of this phenomenon, our attention is directed towards examining vortex flow specifically, convective mixing initiated by swirl inlet in a narrow fluidic channel.

1.3.2 Electric Field Modulated Micromixng: Active Approach

The need for minimal volumes of bio-samples and biofluids in micro total analysis on Lab-on-a-Chip (LOC) platforms has led researchers to explore various aspects of micromixing (Chew et al., 2007). Active mechanisms, which involve hindering fluid flow and utilizing external sources like electroosmotic flow, demonstrate rapid and effective mixing, particularly in applications such as microarrays, DNA sequencing, sample preparation, analysis, cell separation, detection, and environmental monitoring (Nguyen and Wu, 2005). Active techniques, incorporating additional elements like local impedance and electroosmotic flow, expedite the generation of vortices in flow passages, contrasting with the time-consuming nature of passive methods. Over the past two decades, EOF-assisted mixing has gained considerable attention among various active methods, addressing a pivotal aspect explored in the present thesis.

The literature (Chang and Yang, 2008; Banerjee et al., 2019) establishes that electrokinetically driven flows in micro confined spaces lead to improved mixing. Due to the significantly small diffusion coefficient of many common fluids in micro-domains, the diffusive Peclet number becomes notably large. For such fluids, the dominant mixing mechanism is convective, achieved through the formation of recirculation zones or chaotic flow (Kumar et al., 2006). In the realm of electroosmotic mixing, patterning mixer walls with alternating positive and negative charges proves beneficial in creating recirculation zones through the induction of two types of flow streams (Biddiss et al., 2004; Hadigol et al., 2011). This patterned charged surface can be manufactured using the soft lithography technique (Duffy et al., 1998; O’Brien et al., 2003). Patterned zeta potential patches at channel walls emerge as the predominantly utilized technique in EOF-assisted mixing methods, leading to a qualitatively improved vortical flow (Qian and Bau, 2002; Hadigol et al., 2011; Loucaides et al., 2012; Ebrahimi et al., 2014; Nayak, 2014; Basati et al., 2019). The enhancement of patterned patch-modulated fluidic functionalities can be further improved by taking into account additional factors. For instance, as discussed in the study by Hadigol et al., (2011) the pseudo-plastic behavior exhibited by non-Newtonian fluids, particularly for dilatant fluids, results in higher flow velocities, a notable aspect to consider. In many instances, the increased fluid velocity leads to the formation of significant vortex configurations within the flow passage. Biddiss et al., (2004) experimentally investigated the effect of surface charge heterogeneity on mixing characteristics in a T-shaped microchannel, reporting a 22 to 68% increase in mixing efficiency with induced circulation by surface charge patterning for a given range of external electric field. Banerjee et al., (2018) numerically examined the effects of corrugation by mounting blocks and patterned surface charges on electroosmotic mixing. They observed that an increase in surface potential enhances both mixing efficiency and flow rate. Besides, mixing is more effective when blocks are configured with patches compared to the case of blocks between patches on opposite surfaces. While larger recirculation zones enhance mixing efficiency (Hadigol et al., 2011), it adversely affects the flow rate, an undesirable outcome for rapid mixing (Sánchez et al., 2018). Considering point charges provides accurate results for electroosmotic micromixing only at lower surface potentials, necessitating the consideration of finite ion size effects using the steric effect at higher zeta potentials. Yazdi et al., (2015) investigated the impact of finite ion size on mixing characteristics in a Y-shaped electroosmotic micromixer with higher zeta potential (50 to 250 mV), reporting a 35% and 49% reduction in mixing length.

In the realm of narrow-fluidic assays, the periodic application of a transverse electric field introduces changes to the mixing dynamics by inducing local vortices, as observed in studies by Pacheco, (2008) and Krishnaveni et al., (2017). These investigations suggest that employing patterned zeta potential patches or impedance-inducing solid structures, such as a conducting link, leads to the development of distinct vortical flow configurations, offering a dynamic approach to achieve optimal mixing efficiency. Consequently, the manipulation of flow dynamics through the periodic patterning of the polyelectrolyte layer and polymer layer is anticipated to reveal unique aspects, including the formation of vortices, extended retention time of species, and enhanced mixing efficiency (Gaikwad et al., 2020). The distinctive features of polyelectrolyte layers offer the opportunity to enhance various challenging functionalities by manipulating their controllable physical and chemical properties (Das et al., 2015; Brilliantov et al., 2016). These enhancements primarily arise from the local and confined impact of the electric double layer (EDL) on the underlying hydrodynamics. A significant portion of biofluids and bio-samples exhibit non-Newtonian behavior, prompting numerous investigations into the electroosmotic mixing of such fluids (Usefian et al., 2019; Banerjee and Nayak, 2019; Alipanah et al., 2021). Thus, employing patterned polyelectrolyte layers to modulate electrokinetic effects for improving the micromixing of non-Newtonian fluids presents a novel proposition in small-scale transport processes. Surprisingly, this potential application remains largely unexplored in the current literature.

The driving force behind this research is to address the limitations associated with the micromixers mentioned earlier. Within the microfluidics domain, there exists a significant need for approaches that facilitate both gentle passive and active micromixing. The exploration into mixing aims to establish design principles for efficiently combining liquid samples in microfluidic devices. This research delves into two underexplored mixing techniques, focusing on achieving short mixing times, minimal downstream mixing distances, simplistic designs, low energy consumption, mixing efficiency surpassing 90%, and a straightforward control system.

1.4 Exploring Gaps in Existing Literature: Physical Perspectives

Addressing the mixing challenges in microdevices has been the subject of extensive research since the inception of microfluidics in the 1990s. Various mixing techniques have been explored to tackle these issues, achievable through either active or passive techniques (Nguyen and Wu, 2005; Hessel et al., 2005; Lee et al., 2011). Active mixing requires an external energy source to induce mixing, employing methods such as ultrasound, acoustic forces, bubble-induced vibrations, electrokinetic instabilities, periodic flow rate variations, magneto-hydrodynamics, small impellers, integrated microvalves, and pumps. On the other hand, passive mixing relies on concepts like geometric variations in microchannels, introducing obstacles, using flow energy as pumping power, leveraging hydrostatic potentials, among other approaches, to achieve efficient mixing. One noteworthy passive technique is chaotic-based mixing, which generates eddies in the flow patterns, creating high specific interfaces along the lateral direction. This leads to increased mixing through advection, making it a cost-effective method with significant potential in micro Total Analysis Systems (μTAS).

However, microfluidic mixing is a complex undertaking, presenting numerous challenges. One such challenge is the scale of the system, where the reduced length scale of micromixers, coupled with a high surface-volume ratio, significantly influences fluid patterns. Another complication arises from the interplay between viscous and inertial forces, with viscous forces prevailing over inertial forces at the micro scale, amplifying the intricacy of the mixing process (Kirby, 2010). Despite ongoing efforts to develop effective micromixers, the challenge of achieving efficient mixing at low Reynolds numbers (Re) in microdevices persists (Purcell, 1977). Existing mixing techniques face challenges in achieving effective mixing at low Reynolds values, where molecular diffusion plays a crucial role. Additionally, microchannels often exhibit high Peclet numbers (Pe) (Stroock et al., 2002), indicating a dominance of convection over transverse diffusion. In these scenarios, fluid flow tends to follow a straight path from the inlet to the outlet, limiting the potential for diffusion. This undermines the advantages of miniaturization and the lab-on-a-chip concept. To address these issues, significant research has been dedicated to devising strategies for achieving rapid laminar flow mixing in microfluidic systems. Consequently, researchers are consistently proposing new alternatives in the pursuit of finding a viable and practical solution to the persistent mixing problem.

Addressing micromixing challenges within the low Reynolds (Re) and high Peclet (Pe) number regimes poses a complex endeavor (Villermaux et al., 2008). Our research is dedicated to achieving Vortex-assisted convective mixing in microchannels by employing a dual strategy involving both passive and active methods. In the realm of passive mixing, we delve into a cylindrical channel configuration featuring an inlet swirl to initiate the necessary tangential fluid movement for creating a vortex and achieving effective mixing. The dynamics of a vortex, encompassing its formation, transport, decay, and its impact on mixing within engineering systems/devices across various spatiotemporal scales, are considered crucial. However, ensuring the sustainability of this characteristic throughout the flow becomes a critical factor, particularly in the context of macro/microscale transport. This innovative design enhances advection-dominated mixing efficiently. On the other hand, the active approach involves the utilization of a narrow-fluidic channel with walls coated using a soft polyelectrolyte layer, which holds significant importance in applications involving electrokinetic phenomena, specifically electroosmotic flow. In this active method, advection-dominated mixing is accomplished by applying an external electric field to induce electroosmotic flow along the axial direction. This process promotes increased advection flow, thereby facilitating the desired level of mixing.

1.5 Aim of the Present Work and Problem Definitions

The literature review underscores the extensive rationale supporting the undertaking of this research. Exploring the existing amount of work reveals a substantial volume of research in microfluidic mixing, encompassing theoretical, experimental, and numerical approaches by various researchers over the years. The main aim of this project is to investigate methods to improve mixing in microfluidic devices through passive and active means. This entails introducing inlet swirl as a passive approach and applying an external electrical field as an active method, all within a narrow-fluidic channel. In the active approach, a soft polyelectrolyte layer coats the walls, minimizing the degradation of biological samples during transportation. This design aims to achieve effective mixing with minimal external energy consumption. The relevance of this approach is particularly notable in applications dealing with biofluids and electrokinetic phenomena, such as electroosmotic flow (EOF). A persistent challenge faced by researchers is achieving efficient mixing in a microchannel within limited space, necessitating the incorporation of secondary flows to enhance advection strength over molecular diffusion. These identified gaps and challenges serve as compelling justifications for further exploration in this specific research domain.

Drawing upon the insights derived from the literature review and recognizing the gaps highlighted in the preceding sections, we move forward to articulate the objectives for this thesis. These objectives are intricately tailored to address the specific applications discussed, aiming to accomplish advection-dominated mixing within a short time and length scale. In an effort to tackle the aforementioned challenges, the following research objectives are delineated for this study.

1.5.1 *Effective solute mixing of a Newtonian fluid within a cylindrical narrow fluidic channel, specifically in the presence of an inlet swirl*

Our first objective focuses on investigating the flow of Newtonian fluids through a narrow cylindrical fluidic channel. This involves solving the Navier-Stokes (NS) equation to derive analytical expressions for both axial and tangential (or swirl) velocities. To address the numerical solution of the scalar species transport equation, we integrate the analytically derived velocity fields. Following this, we conduct a thorough analysis of the effectiveness of solute mixing, considering the inlet swirl responsible for the bulk rotation of the fluid in the tangential direction. This analysis involves a comprehensive evaluation that includes both qualitative and quantitative assessments. It explores a defined set of parameters, such as Reynolds number and Peclet number, with a specific emphasis on practical applications.

1.5.2 *Effective solute mixing of a non-Newtonian fluid within a cylindrical narrow fluidic channel, specifically in the presence of an inlet swirl*

The second objective extends the initial investigation by incorporating non-Newtonian fluids. This entails solving the Navier-Stokes (NS) equation with a focus on deriving analytical expressions for axial and tangential (or swirl) velocities using the power-law scheme. Additionally, we integrate the derived velocity field expressions into the scalar species transport equation and solve it numerically. Subsequently, a comprehensive examination of the effectiveness of solute mixing is conducted, encompassing both qualitative and quantitative assessments. In this analysis, the prominent role of inlet swirl becomes evident in achieving efficient mixing, attributed to the bulk rotation of fluid in the tangential direction. This effect is particularly pronounced with an increase in shear-thinning fluid compared to shear-thickening fluid. The assessment covers a specific set of parameters, emphasizing their practical applications, which include considerations of Reynolds number and the power-law index.

1.5.3 *Effective solute mixing of non-Newtonian fluid through the modulation of electroosmotic vortices using a soft polyelectrolyte layer*

In the third objective, we employed numerical methods to explore the transport and mixing behaviours of biofluids exhibiting non-Newtonian characteristics. This study explores the impact of polyelectrolyte layer (PEL)-modulated electrostatics, fluid rheology, and frictional drag on biofluids. The expectation is a notable rise in flow velocity due to electroosmotic actuation, counteracted by increased frictional drag potentially reducing flow velocity. Specifically, the research examines the influence of patterned PEL structures on vortical flow and associated mixing phenomena. The study conducts various analyses with different patterns under the same set of parameters, focusing on practical applications and interpreting the implications of each configuration. Furthermore, the research investigates how the PEL affects mixing length and the initiation of recirculation zones to achieve better mixing within a short length scale in the given problem.

1.5.4 Effective solute mixing of non-Newtonian fluid through the modulation of electroosmotic vortices using a pH-dependent soft polyelectrolyte layer

The fourth objective investigated here extends the third by introducing a pH-dependent soft polyelectrolyte layer (PEL) structure within the narrow fluidic channel while maintaining the effects of fluid rheology. This investigation delves into the combined impact of pH-dependent PEL-modulated electrostatics, fluid rheology, and solution bulk pH (pH_b) on biofluids. The primary goal is to explore the characteristics of a non-Newtonian vortex influenced by a pH-sensitive PEL modulated electroosmotic effect in a microchannel. The study specifically focuses on the influence of pH-sensitive PEL structures on vortical flow and associated mixing phenomena. Utilizing various analyses with different patterns under consistent parameters, the research emphasizes practical applications and interprets the implications of each configuration. Ultimately, the study's findings may significantly influence the design of microfluidic devices tailored for mixing and transporting non-Newtonian liquids at specific pH_b values.

After outlining the objectives of the thesis, the following section provides a detailed explanation of how these objectives are organized into distinct problems, followed by a description of the corresponding work conducted to address each problem.

1.6 Outline of the Thesis

The current dissertation is organized into six primary chapters. The initial chapter introduces the topic of interest, provides a literature review, and establishes objectives specific to each considered application. Subsequent chapters (two to five) delve into the addressed problems. The epilogue summarizes our findings and conclusions from each chapter, while also outlining the scope for future work.

The key points addressed in each chapter are summarized as follows:

- Chapter 2 focuses on the impact of swirl flow, specifically vorticial flow, on the mixing of two similar Newtonian fluids in a narrow cylindrical tube. The study considers low Reynolds number transport and high Peclet number, solving for fully developed flow and incorporating the Rankine vortex to derive the expression for the swirl velocity field. The obtained analytical velocity field expression is then used in the numerical solution of the scalar species transport equation, employing an in-house developed finite volume method.

- Moving on to Chapter 3, a novel swirl-assisted mixing technique is proposed for a narrow cylindrical channel, exploring the influence of vorticial flow on the mixing of non-Newtonian fluids under laminar flow conditions. The chapter analytically derives the swirl velocity profile by combining fully developed flow with the Rankine vortex condition at the channel inlet. The rheology of non-Newtonian fluids is described using Ostwald's de'Waele power-law model, and the governing equations for the defined computational domain are numerically solved with an in-house developed finite volume method.

- Chapter 4 introduces a novel electroosmotic flow assisted mixing technique in a patterned-soft narrow-fluidic channel. The study investigates the impact of a PEL-modulated interfacial electrostatics and pressure-driven bulk flow on the flow field and mixing characteristics of non-Newtonian solutes in a micromixer. Transport equations are solved using the finite element-based numerical solver COMSOL Multiphysics, focusing on the flow of non-Newtonian Carreau fluids through a narrow fluidic channel with a patterned PEL-PL patch at its inner-wall surfaces. The chapter emphasizes the influence of physical and geometrical parameters on mixing dynamics.

- In Chapter 5, a novel electroosmotic flow assisted mixing technique is proposed in a pH-dependent patterned-soft narrow-fluidic channel. The study thoroughly examines electroosmotic flow and species mixing characteristics of non-

Newtonian fluids in pH-dependent polyelectrolyte-grafted soft microchannels. The transport equation, following the Carreau model, is numerically solved within the framework of COMSOL Multiphysics. The study considers the effect of protonic exchange with polyelectrolyte groups, pH and ionic concentration-dependent zeta potential, and highlights the consequential influence of formed vortices on mixing dynamics.

- Finally, Chapter 6 draws important conclusions based on the inferences from the preceding chapters and outlines the scope for future work within the context of the present thesis theme.

Chapter 2

Effective solute mixing of a Newtonian fluid within a cylindrical narrow fluidic channel, specifically in the presence of an inlet swirl

The present study is driven by the aim to explore the impact of vortices, specifically swirl, on mixing. Our investigation carries out the study in two stages. In the primary stage, we employ an analytical approach to derive the swirl velocity field. This involves superimposing a Rankine vortex onto an axially fully developed flow. Subsequently, we utilize the obtained velocity field to numerically solve the species transport equation. This numerical solution is achieved through the implementation of a finite volume-based, in-house developed code. With the results in hand, we thoroughly discuss both the qualitative and quantitative aspects of mixing between two fluids in a decaying swirling laminar pipe flow.

2.1 Problem Description and Mathematical Formulation

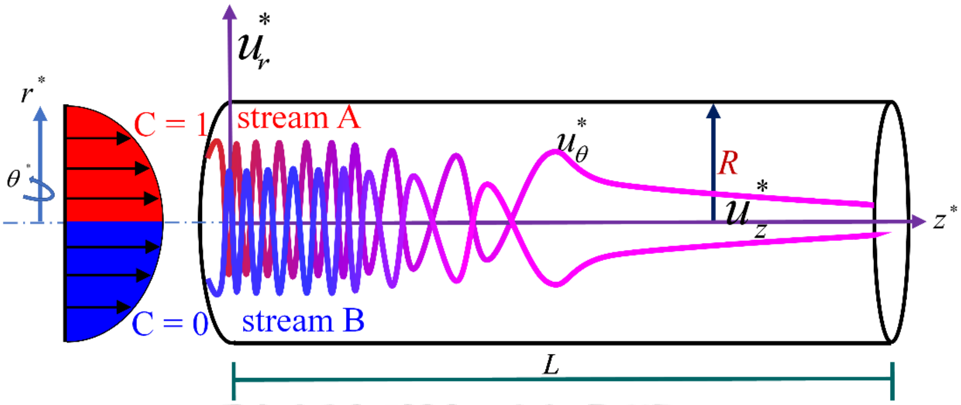

Figure 2.1: A schematic representation of the fluid flow configuration with initial concentration 1 and 0 at the upper and lower domain at the inlet of pipe.

In the present study, we consider a small cylindrical channel with characteristic radius R and length L. The cylindrical coordinate system is defined such that r^* corresponds to the channel's radius, z^* to the axis of the tube, and θ^* to the azimuthal (or tangential) direction. The velocity components u_r^*, u_θ^* and u_z^* are aligned with these respective coordinates, as illustrated in Fig. 2.1. We study the mixing of two fluid streams, A (colored red) and B (colored blue), which share similar thermo-physical properties, as illustrated in Fig. 2.1 (Gaikwad et al., 2020). In our analysis of species transport, we assume that the initial concentration of fluid A is 1, while that of fluid B is 0. The dye, representing the tractor species, is associated with stream A, characterized by a diluted concentration, and it is intended to mix with the pure liquid in stream B (Cosentino et al., 2015). To evaluate the mixing efficiency, stream A, containing the diluted concentration, is introduced at the upper half of the inlet, while stream B is introduced at the bottom half of the inlet. Utilizing this information, we simplify the governing equation for the fluid flow of both species, treating them as a single fluid system.

2.1.1 Governing equations

The governing equations for fluid flow depicted in Fig. 2.1 correspond to the three-dimensional Navier-Stokes (NS) equations. These equations describe mass, momentum, and species transport in cylindrical coordinates with component of velocity u_r^*, u_θ^* and u_z^*, considering incompressible and laminar flow. The formulations are expressed as follows (Deen, 2016):

Continuity equation:

$$\frac{\partial \rho}{\partial t}+\frac{1}{r^*}\frac{\partial(\rho r^* u_r^*)}{\partial r^*}+\frac{1}{r^*}\frac{\partial(\rho u_\theta^*)}{\partial \theta^*}+\frac{\partial(\rho u_z^*)}{\partial z^*}=0 \tag{2.1}$$

r^* - momentum equation:

$$\begin{aligned}&\frac{\partial u_r^*}{\partial t}+u_r^*\frac{\partial u_r^*}{\partial r^*}+u_\theta^*\frac{1}{r^*}\frac{\partial u_r^*}{\partial \theta^*}+u_z^*\frac{\partial u_r^*}{\partial z^*}-\frac{u_\theta^{*2}}{r^*}=\\&-\frac{1}{\rho}\frac{\partial p}{\partial r^*}+\frac{\mu}{\rho}\left[\frac{1}{r^*}\frac{\partial}{\partial r^*}\left(r^*\frac{\partial u_r^*}{\partial r^*}\right)+\frac{1}{r^{*2}}\frac{\partial^2 u_r^*}{\partial \theta^{*2}}+\frac{\partial^2 u_r^*}{\partial z^{*2}}-\frac{u_r^*}{r^{*2}}-\frac{2}{r^{*2}}\frac{\partial u_\theta^*}{\partial \theta^*}\right]+g_r\end{aligned} \tag{2.2}$$

θ^* - momentum equation:

$$\begin{aligned}&\frac{\partial u_\theta^*}{\partial t}+u_r^*\frac{\partial u_\theta^*}{\partial r^*}+u_\theta^*\frac{1}{r^*}\frac{\partial u_\theta^*}{\partial \theta^*}+u_z^*\frac{\partial u_\theta^*}{\partial z^*}+\frac{u_r^* u_\theta^*}{r^*}=\\&-\frac{1}{\rho}\frac{1}{r^*}\frac{\partial p}{\partial \theta^*}+\frac{\mu}{\rho}\left[\frac{1}{r^*}\frac{\partial}{\partial r^*}\left(r^*\frac{\partial u_\theta^*}{\partial r^*}\right)+\frac{1}{r^{*2}}\frac{\partial^2 u_\theta^*}{\partial \theta^{*2}}+\frac{\partial^2 u_\theta^*}{\partial z^{*2}}-\frac{u_\theta^*}{r^{*2}}+\frac{2}{r^{*2}}\frac{\partial u_r^*}{\partial \theta^*}\right]+g_\theta\end{aligned} \tag{2.3}$$

z^* - momentum equation:

$$\begin{aligned}&\frac{\partial u_z^*}{\partial t}+u_r^*\frac{\partial u_z^*}{\partial r^*}+u_\theta^*\frac{1}{r^*}\frac{\partial u_z^*}{\partial \theta^*}+u_z^*\frac{\partial u_z^*}{\partial z^*}=\\&-\frac{1}{\rho}\frac{\partial p}{\partial z^*}+\frac{\mu}{\rho}\left[\frac{1}{r^*}\frac{\partial}{\partial r^*}\left(r^*\frac{\partial u_z^*}{\partial r^*}\right)+\frac{1}{r^{*2}}\frac{\partial^2 u_z^*}{\partial \theta^{*2}}+\frac{\partial^2 u_z^*}{\partial z^{*2}}\right]+g_z\end{aligned} \tag{2.4}$$

Scalar Species Transport Equation:

$$\frac{\partial C^*}{\partial t}+u_r^*\frac{\partial C^*}{\partial r^*}+u_\theta^*\frac{1}{r^*}\frac{\partial C^*}{\partial \theta^*}+u_z^*\frac{\partial C^*}{\partial z^*}=D_0\left[\frac{1}{r^*}\frac{\partial}{\partial r^*}\left(r^*\frac{\partial C^*}{\partial r^*}\right)+\frac{1}{r^{*2}}\frac{\partial^2 C^*}{\partial \theta^{*2}}+\frac{\partial^2 C^*}{\partial z^{*2}}\right] \tag{2.5}$$

Here, u_r^*, u_θ^* and u_z^* are the velocity components in the r^*, θ^* and z^* directions respectively. μ is the dynamic viscosity of the fluid, P^* is the fluid pressure, ρ is the density of the fluid, C^* is the species concentration and D_0 is the molecular diffusion coefficient of the constituent species.

2.1.2 Analytical solution of fluid flow equations

To streamline the governing equations, we make the assumptions that the flow is steady, axis-symmetric, and fully developed in the axial direction. Under these physically justified assumptions, the simplified governing equations for fluid flow, considering the components of velocity u_r^*, u_θ^* and u_z^*, can be expressed as follows (Kumar et al., 2020):

Continuity equation:

$$\frac{1}{r^*}\frac{\partial(\rho r^* u_r^*)}{\partial r^*} = 0 \tag{2.6}$$

r^* -momentum equation:

$$\frac{u_\theta^{*2}}{r^*} = \frac{1}{\rho}\frac{\partial p^*}{\partial r^*} \tag{2.7}$$

θ^* -momentum equation:

$$u_z^*\frac{\partial u_\theta^*}{\partial z^*} = \frac{\mu}{\rho}\left[\frac{1}{r^*}\frac{\partial}{\partial r^*}\left(r^*\frac{\partial u_\theta^*}{\partial r^*}\right) - \frac{u_\theta^*}{r^{*2}} + \frac{\partial^2 u_\theta^*}{\partial z^{*2}}\right] \tag{2.8}$$

z^* -momentum equation:

$$\frac{1}{\rho}\frac{\partial p^*}{\partial z^*} = \frac{\mu}{\rho}\left[\frac{1}{r^*}\frac{\partial}{\partial r^*}\left(r^*\frac{\partial u_z^*}{\partial r^*}\right)\right] \tag{2.9}$$

Based on the initial justified assumption, the simplified continuity Eq. (2.6) implies that the radial component of velocity is uniformly zero across the entire domain, a consequence of assuming impermeable walls. Subsequently, the governing equation in the radial direction (Eq. 2.7) establishes a relationship between the radial pressure gradient and the swirl (tangential) velocity component, a topic elaborated in the subsequent sections. Incorporating the radial velocity constraint and the axis-symmetric condition, the governing momentum equation in the tangential direction simplifies to Eq. (2.8), wherein the diffusion terms provide the leverage to analyze physical phenomena at lower velocities. Considering all the aforementioned assumptions, the governing equation for momentum in the axial direction is further simplified to Eq. (2.9). It is noteworthy that the axis-symmetry of the flow stems from the constant thermo-physical properties of the two fluids involved. While the species concentration Eq. (2.5) does not exhibit axis-symmetry, its simplified form is presented in the following section for ease of discussion in addressing the problem at hand.

The boundary conditions on the tube wall $(r^* = R)$ follows no-slip boundary condition for the axial velocity. The symmetry boundary condition is invoked for the axial velocity at the axis $(r^* = 0)$. The same may be written as $u_z^*(R) = 0$, $\partial u_z^* / \partial r^*|_{r^*=0} = 0$. From the discussion on swirl decay in introduction section, conveys, that the magnitude of swirl velocity, u_θ^* is very small when compared to axial velocity along the domain length. With this assumption, the pressure gradient in radial direction is negligible as compared to the pressure gradient in the axial direction as seen from Eq. (2.7). Therefore, Eq. (2.7) loses significance due to its small magnitude compared to Eq. (2.9) and there is no need to solve the equation separately. This results in $p^* \approx p^*(z)$, which enables us to solve the axial momentum Eq. (2.9) as a regular Hagen-Poiseuille flow condition. In such case, axial velocity in the cylindrical channel is given as:

$$u_z^* = 2u_{av}\left[1-\left(\frac{r^*}{R}\right)^2\right] \tag{2.10}$$

Here, u_{av} is the average flow velocity in the microchannel. At the inlet of the channel, swirl flow is superimposed with fully developed flow, where the condition for swirl flow can be obtained by Rankine vortex at the inlet (Reader-Harris, 1994; Bali, 1998; Greitzer et al., 2007; Shtern, 2018; Kumar et al., 2020). Therefore, swirl velocity profile at the inlet,$u_\theta^*(0, r^*) = u_{\theta,i}^*(r^*)$, can be represented as follows:

$$u_\theta^*(0,r^*) = \begin{cases} u_{\theta,i,\max}^* \dfrac{r^*}{r_t^*}, r^* \le r_t^* \text{ and } u_{\theta,i,\max}^* \dfrac{r_t^*\left(R-r^*\right)}{r^*\left(R-r_t^*\right)}, r^* \ge r_t^* \end{cases} \tag{2.11}$$

Note that, r_t^* is the dimensional transition radius that represents the occurrence of transition from forced $(r^* \le r_t^*)$ to free vortex $(r^* \ge r_t^*)$ at the channel inlet. In order to solve the momentum equation in tangential direction, apart from no-slip and axis symmetric condition, one more boundary condition is required to handle the axial diffusion of radial velocity component. As the axial length of the pipe is very large when compared to the radius $(r^* \ll L^*)$, we can consider diffusion due to radial velocity at the outlet of the pipe is negligible and the considered boundary conditions, given as:

$$u_\theta^*(z^*,R) = 0, u_\theta^*(z^*,0) = 0, u_\theta^*(L^*,r^*) = 0 \tag{2.12}$$

2.1.3 Non-dimensional form of equations

We next take an effort to cast the system of still relevant governing equations (ones that are not trivially satisfied) and the respective boundary into its dimensionless form. Now, to frame the governing equations and boundary conditions in a non-dimensional form, we define the set of non-dimensional variables as follows:

$$r=\frac{r^*}{R},\ \mathrm{z}=\frac{z^*}{R},\ L=\frac{L^*}{R},\ W(z,r)=\frac{u_\theta^*}{u_{av}},\ \mathrm{V}=\frac{u_r^*}{u_{av}},\ U(r)=\frac{u_z^*}{u_{av}},\ r_t=\frac{r_t^*}{R}\ \text{, and } \mathrm{Re}=\frac{\rho u_{av}R}{\mu}$$

Here, *r* and *z* represent non-dimensional radial and axial coordinate; *V*, *U*(*r*), *W*(*z*, *r*) are the non-dimensional radial, axial and tangential velocity; r_t and L, represents the non-dimensional transition radius and the channel length. In the aspect of investigating flow phenomenon, we define non-dimensional Reynolds number, Re, based on average velocity and the radius of the pipe.

Using the non-dimensional variables, we intend to solve the governing momentum Eq. (2.8) in θ-direction, which is represented in a non-dimensional form in Eq. (2.13).

$$(\mathrm{Re})U\frac{\partial W}{\partial z}=\left[\frac{1}{r}\frac{\partial}{\partial r}\left(r\frac{\partial W}{\partial r}\right)-\frac{W}{r^2}+\frac{\partial^2 W}{\partial z^2}\right] \tag{2.13}$$

2.1.4 Dimensionless form of velocity fields

To couple the axial velocity and solve Eq. (2.13), the expression for the dimensionless form of the axial velocity field can be derived from Eq. (2.10). This is expressed as:

$$U=\frac{u_z^*}{u_{av}}=2\left[1-\left(\frac{r^*}{R}\right)^2\right]=2\left[1-r^2\right] \tag{2.14}$$

The dimensionless boundary conditions associated with Eq. (2.13) as follows:

$$W(0,r)=u_{\theta,i}^*(r^*)/u_{av},\ W(L\rightarrow\infty,r)\rightarrow 0,\ W(z,0)=0,\ W(z,1)=0 \tag{2.15}$$

Eq. (2.13) is solved using the variable separation method along with their respective derived boundary conditions mentioned in Eq. (2.15). Hence, the obtained swirl velocity profile in non-dimensional form is:

$$W(z,r)=\sum_{n=1}^{\infty}\frac{C_n\exp\left(\left(-0.5\right)z\left(\sqrt{\mathrm{Re}^2+4\lambda_n}-\mathrm{Re}\right)\right)\exp\left(-\lambda_n r^2/\sqrt{2}\right)L\left(\lambda_n/2\sqrt{2},-1,\sqrt{2}\lambda_n r^2\right)}{r} \quad (2.16)$$

The above solution given by Eq. (2.16) is a form of the Sturm-Liouville problem (Kaplan, 1981; Andrews and Phillips, 2003), which gives a series solution. Here, $L(a,b,r)$ is known as the generalized Laguerre function and is given by LaguerreL[n,k,r] = $L_n^k(r)$ (Arfken and Weber, 1999). Using the boundary conditions $W(z,1)=0$, the eigen values λ_n are calculated using the equation $L\left(\lambda_n/2\sqrt{2},-1,\sqrt{2}\lambda_n\right)=0$ and the first twenty of which are tabulated in Table 2.1. At the inlet, swirl velocity profile is assumed as a Rankine vortex, the dimensionless form of which is given below (Greitzer et al., 2007; Shtern, 2018):

$$W(0,r)=\left\{\frac{u_{\theta,i,\max}}{u_{av}}\frac{r}{r_t},r\le r_t \text{ and } \frac{u_{\theta,i,\max}}{u_{av}}\frac{r_t\left(1-r\right)}{r\left(1-r_t\right)},r\ge r_t\right. \quad (2.17)$$

The value C_n in Eq. (2.16) is calculated by using the orthogonality condition for the Eigen-functions by the Sturm-Liouville theorem (Kaplan, 1981) along with the swirl velocity inlet condition described by Eq. (2.17);

$$C_n=\frac{\int_0^1 W(0,r)\exp\left(-\lambda_n r^2/\sqrt{2}\right)L\left(\lambda_n/2\sqrt{2},-1,\sqrt{2}\lambda_n r^2\right)\left(1-r^2\right)dr}{\int_0^1\left[\exp\left(-\lambda_n r^2/\sqrt{2}\right)L\left(\lambda_n/2\sqrt{2},-1,\sqrt{2}\lambda_n r^2\right)/r\right]^2 r\left(1-r^2\right)dr} \quad (2.18)$$

At this point, it is crucial to highlight that our study incorporates the additional effect of axial diffusion of swirl velocity, denoted by $\partial^2 W/\partial z^2$, a factor that was previously neglected in the work of Yao and Fang, (2012). Consequently, in our investigation, we conduct a comparative analysis of our results with those obtained by Yao and Fang, (2012).

In pursuit of quantifying the swirl intensity ($S(z)/S(0)$) along the channel, we define a dimensionless number called swirl number, $S(z)$. It is defined as the ratio of the axial flux of angular momentum to the axial flux of axial momentum at a particular axial cross-section following Reader-Harris; it may be mathematically defined as (Reader-Harris, 1994):

$$S(z)=\int_0^R u_z^* u_\theta^* r^{*2} dr^* \Big/ R\int_0^R u_z^{*2} r^* dr^* = \int_0^1 UWr^2 dr \Big/ \int_0^1 U^2 r dr \tag{2.19}$$

Using Eq. (2.16) and (2.17) in Eq. (2.19), the analytical expression of the ratio of swirl intensity in Eq (2.19) at a cross-section to the swirl intensity at inlet is given by:

$$\frac{S(z)}{S(0)}=\frac{\sum_{n=1}^{\infty} C_n \exp\left[(-0.5)z\left(\sqrt{\mathrm{Re}^2+4\lambda_n}-\mathrm{Re}\right)\right]\int_0^1 \exp\left[-\lambda_n r^2/\sqrt{2}\right] L\left(\lambda_n/2\sqrt{2},-1,\sqrt{2}\lambda_n r^2\right)2r\left(1-r^2\right)dr}{\int_0^1 W(0,r)U(r)r^2 dr} \tag{2.20}$$

Having obtained the analytical expression for velocity profiles, we quantify the mixing performance between the two fluids in the next sub-section. First, we obtain the spatial distribution of the species concentration in the channel domain and then the mixing efficiency.

n	λ_n	n	λ_n
1	3.269732	11	17.438559
2	6.114707	12	20.267603
3	8.948451	13	23.096475
4	11.779382	14	25.925236
5	14.609230	15	28.753922
6	17.438559	16	31.582555
7	20.267603	17	34.411149
8	23.096475	18	37.239714
9	25.925236	19	40.068257
10	28.753922	20	42.896782

Table 2.1: The first twenty eigenvalues ($\boldsymbol{\lambda_n}$) for the generalized Laguerre function.

2.2 Numerical description of species Transport equation

So far, the scalar species transport equation given in Eq. (2.5) has not been simplified. Retaining all the previous assumptions, except for axis-symmetry, since the two fluids occupy distinct halves of the pipe at the inlet, the simplified governing species transport equation is expressed as follows:

$$u_r^* \frac{\partial C^*}{\partial r^*} + u_\theta^* \frac{1}{r^*} \frac{\partial C^*}{\partial \theta^*} + u_z^* \frac{\partial C^*}{\partial z^*} = D_0 \left[\frac{1}{r^*} \frac{\partial}{\partial r^*} \left(r^* \frac{\partial C^*}{\partial r^*} \right) + \frac{1}{r^{*2}} \frac{\partial^2 C^*}{\partial \theta^{*2}} + \frac{\partial^2 C^*}{\partial z^{*2}} \right] \qquad (2.21)$$

Note that, C^* in the above-mentioned equation is the species concentration of fluid and D_0 is the diffusion coefficient of fluid. In the purview of distinguishing the species concentration of constituent fluids in the flow domain, we assign $C^* = 1$ for stream A (red colour) and $C^* = 0$ for stream B (blue colour), as shown in Fig. 2.1. To non-dimensionalize Eq. (2.21), we define the dimensionless concentration $C = C^*/C_0$, where C_0 is the initial concentration of stream A. Additionally, for the investigation of diffusion phenomena, we introduce a dimensionless number known as the Peclet number; $\mathrm{Pe} = u_{av} R / D_0$, based on the average velocity. Therefore, the non-dimensional form of the species transport equation can be expressed as follows:

$$V \frac{\partial C}{\partial r} + \frac{W}{r} \frac{\partial C}{\partial \theta} + U \frac{\partial C}{\partial z} = \frac{1}{\mathrm{Pe}} \left[\frac{1}{r} \frac{\partial}{\partial r} \left(r \frac{\partial C}{\partial r} \right) + \frac{1}{r^2} \frac{\partial^2 C}{\partial \theta^2} + \frac{\partial^2 C}{\partial z^2} \right] \qquad (2.22)$$

Where, the Peclet number (Pe) in above equation is defined as the ratio of convection strength to diffusion strength. In order to have rigid numerical model with increase or decrease in Peclet number, Pe, we have used power scheme to obtain better approximate solution. The short description on power law scheme is mentioned in following discussion.

In the aspect of understanding the underlying phenomenon of mixing assisted by vorticial flow, in our study, we solve three dimensional, steady, laminar and incompressible, species transport equation using in-house finite volume method. The swirl velocity (tangential) and axial velocity profile obtained from analytical framework, is used to solve the governing species transport equation. The non-dimensional form of boundary condition associated with the species transport Eq. (2.22) in (r, θ, z) direction is mentioned in Eq. (2.23a-c).

$$\text{in } r\text{-direction: } \left.\frac{\partial C}{\partial r}\right|_{r=0} = 0 \quad \text{and} \quad \left.\frac{\partial C}{\partial r}\right|_{r=1} = 0 \qquad (2.23a)$$

$$\text{in } \theta\text{-direction: } C_{(\theta=0)} = C_{(\theta=2\pi)}; \left.\frac{\partial C}{\partial \theta}\right|_{\theta=0} = \left.\frac{\partial C}{\partial \theta}\right|_{\theta=2\pi} \qquad (2.23b)$$

$$\text{in } z\text{-direction: } C\big|_{z=0} = \begin{cases} 1, & 0 < \theta < \pi, \text{fluid A} \\ 0, & \pi < \theta < 2\pi, \text{fluid B} \end{cases} \quad \text{and} \quad \left.\frac{\partial C}{\partial z}\right|_{z=L} = 0 \qquad (2.23c)$$

Note that, in the z direction, at the inlet i.e., at $z = 0$, the concentration of fluids A and B is specified, and at the outlet i.e., at $z = L$ (>> 1), the fully mixed condition is considered. The values of species concentration at the inlet i.e., $C_{0,A} = 1$ (for fluid A) and $C_{0,B} = 0$ (for fluid B) respective to the domains $\theta \in [0, \pi]$ and $\theta \in [\pi, 2\pi]$ represent the typical mixing assay wherein the continuous flow of biological fluid like blood or DNA carried fluid gets infused with the chemical drug/reagent or another fluid which is rich in biologically entities such as RBCs, white cells etc (Suzuki et al., 2004).

In the next section of the paper, we discuss a numerical framework for solution of Eq. (2.22) along with its appropriate boundary conditions mentioned in Eq. (2.23a-c).

2.2.1 Description of model using Power-Law Scheme

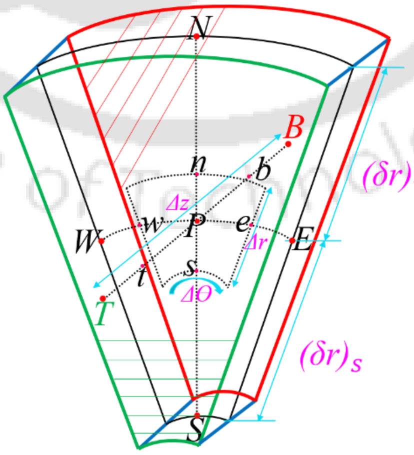

Figure 2.2: Control volume for 3D cylindrical coordinates grid system along three mutual perpendicular direction.

The species transport equation, as mentioned in Eq. (2.22), is discretized using the finite volume approach (Patankar, 1980; Patankar, 1981). Fig. 2.2 illustrates the control volume around point *P* delineated by the dashed line in a three-dimensional cylindrical coordinate system along the radial (*r*), azimuthal (θ) and axial (*z*) directions. The control volume is centered around the grid point *P*, and its neighboring grid points are designated as north (*N*), south (*S*), east (*E*), west (*W*), top (*T*), and bottom (*B*). The corresponding faces of the control volume are labeled as *n*, *s*, *e*, *w*, *t*, and *b*, representing the north, south, east, west, top, and bottom faces, respectively. The nomenclature introduced in Fig. 2.2 illustrates the changes in the radial, azimuthal, and axial directions as Δr, $\Delta\theta$ and Δz, respectively. In the radial direction, the variations between the grid point *P* and *N* are indicated by $(\delta r)_n$, and between *S* and *P* by $(\delta r)_s$. The solution of the species transport Eq. (2.22) is implemented using the finite volume method with a power-law scheme, incorporating the boundary conditions specified in Eq. (2.23a-c).

The final discretized equation using the Power-Law scheme and stated boundary conditions without any source term for Eq. (2.22) is written as (Patankar, 1980; Patankar, 1981):

$$a_P C_P = a_N C_N + a_S C_S + a_E C_E + a_W C_W + a_T C_T + a_B C_B \tag{2.24}$$

Where, a_i represent the coefficients of strength of convection- diffusion, $a_P = \sum a_i$ and C_i represent the species concentration at respective grid points. The coefficients of strength of convection-diffusion a_i are given as:

$$a_i = \begin{cases} a_N = D_n \left\llbracket 0, \left(1 - \frac{0.1|F_n|}{D_n}\right)^5 \right\rrbracket + \llbracket 0, -F_n \rrbracket,\ a_S = D_s \left\llbracket 0, \left(1 - \frac{0.1|F_s|}{D_s}\right)^5 \right\rrbracket + \llbracket F_s, 0 \rrbracket \\ a_E = D_e \left\llbracket 0, \left(1 - \frac{0.1|F_e|}{D_e}\right)^5 \right\rrbracket + \llbracket 0, -F_e \rrbracket,\ a_W = D_w \left\llbracket 0, \left(1 - \frac{0.1|F_w|}{D_w}\right)^5 \right\rrbracket + \llbracket F_w, 0 \rrbracket \\ a_T = D_t \left\llbracket 0, \left(1 - \frac{0.1|F_t|}{D_t}\right)^5 \right\rrbracket + \llbracket 0, -F_t \rrbracket,\ a_B = D_b \left\llbracket 0, \left(1 - \frac{0.1|F_b|}{D_b}\right)^5 \right\rrbracket + \llbracket F_b, 0 \rrbracket \end{cases} \tag{2.25a-f}$$

Note that, $F_i = (\mathrm{Pe} \times V_i \times A_i)$ represent the coefficients of strength of convection with velocity (V_i) and area (A_i) vector and $D_i = (A_i/\Delta r_i)$ is strength of molecular diffusion. Using Eq. (2.25a-f), the concentration at each face is calculated by using discretized Eq. (2.24).

2.2.2 Description of numerical framework for mixing

To comprehend the underlying phenomenon of mixing facilitated by vorticial flow, our study involves the numerical solution of the species transport equations, as expressed in Eq. (2.22), utilizing an in-house finite volume code in parallel mode. For the simulations, we used workstation having the specifications as follows: 8 cores with 16 logical processor, ram 32 GB and base speed 3.41 GHz. The discretized form of Eq. (2.24) is employed, taking into account the specified boundary conditions from Eq. (2.23a-c).

At this stage, we introduce the mixing efficiency (η_m) a metric designed to quantify the extent of mixing across the domain. The mixing efficiency is calculated to provide insight into the degree of mixing within the channel at any given cross-section. It serves as a valuable tool for characterizing and explaining the mixing states in the channel and is defined for a cross-section as follows (Wang et al., 2015; Gaikwad et al., 2020):

$$\eta_m(z)=\left[1-\left(\int_A \left|C_i(r,\theta,z)-C_\infty\right| dr d\theta \Big/ \int_A \left|C_0(r,\theta)-C_\infty\right| dr d\theta\right)\right]\times 100\% \qquad (2.26)$$

Here, C_∞ in Eq. (2.26) represents the concentration of species at a perfectly mixed state and is equal to 0.5. We would like to mention that C_0 = 1 in the upper half domain and C_0 = 0 in the lower half domain at the inlet of the channel as shown in Fig. 2.1. Note that, η_m in Eq. (2.26) having zero value implies no mixing of the two fluids and a value of unity implies a completely mixed state.

2.3 Analytical and Numerical Results benchmarking

Before discussing the findings of the present analysis, we benchmark our analytical velocity profiles with the results reported in existing literature (Yao and Fang, 2012) and numerical (ANSYS Fluent 2021 R1) results. To keep our analysis, within in the limit of comparing, we set the ranges of non-dimensional numbers as observed by various researchers (Rezk et al., 2012; Matsunaga and Nishino, 2014; Cortes-Quiroz et al., 2017; Zhang and Luo, 2018; Ansari et al., 2018; Zhang et al., 2019). Therefore, throughout our study, we vary the Reynolds number (0.1 to 200) and Peclet number (~10^2 to 10^4) as mentioned above. Along with this, we vary the transition radius of Rankine vortex between 0.6 to 0.9. First, we demonstrate the validation of obtained analytical swirl velocity profile and further proceed our discussion on grid performance analysis for the solution of the species transport equation.

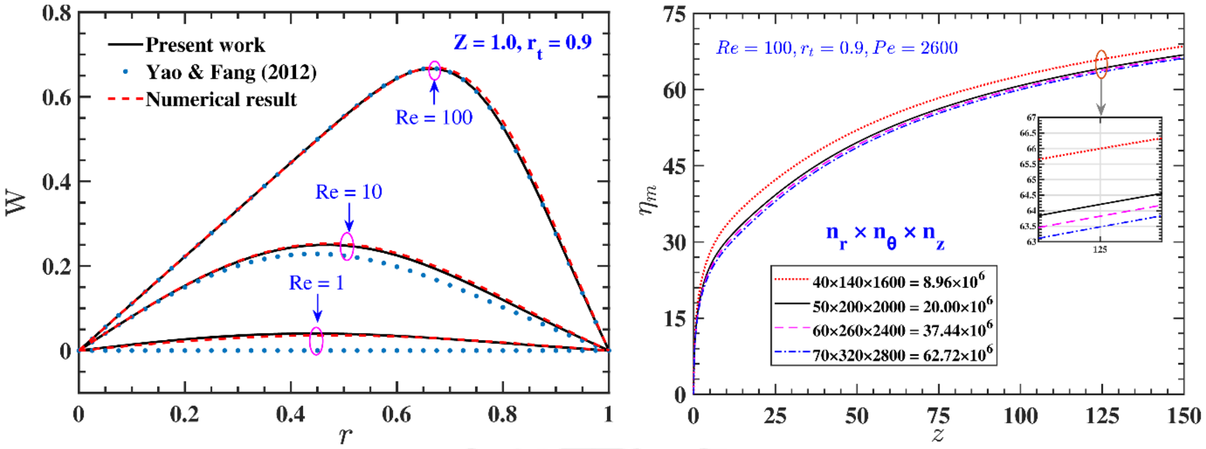

(a) (b)

Figure 2.3: (a) Plots show the model benchmarking of the present work with the results reported in the analytical work of Yao and Fang, (2012) and with the three-dimensional numerical simulation (ANSYS) results. (b) Plots show the grid independence test carried for total number of finite volumes varying from $n_r \times n_\theta \times n_z$ = 9 million to 63 million. The efficiency plot does not change after $n_r \times n_\theta \times n_z = 37.44\times10^6$ and therefore the same is considered to generate the results in the subsequent sections. The values of the other parameters considered for these plots are: (a) $\mathrm{Re}=1,\ 10,\ 100;\ r_t=0.9$ (b) $\mathrm{Re}=100,\ r_t=0.9,\ \mathrm{Pe}=2600$.

In this investigation, the efficacy of the approach delineated in sub-section 2.1.4 is evaluated through an analytical comparison of the velocity profile linked to the solution derived in the aforementioned sub-section with the findings presented by Yao and Fang, (2012) for Reynolds number (Re) equal to 100 at the axial position z = 1 with a transition radius $r_t = 0.9$. Additionally, we undertake a comparative analysis between our analytical findings and the results obtained numerically through three-dimensional simulation using ANSYS Fluent 2021 R1 in parallel mode. For this set of simulation, we have used the same workstation as mentioned above. This comparison is based on a total of 12081477 control volumes and residuals set at 10^{-7}. The purpose of this verification process is to validate the accuracy of the analytical solutions presented in this study, which incorporate the axial diffusion of swirl momentum as described in Eq. (2.16). The comparison results are presented in Fig. 2.3(a). In Fig. 2.3(a), it is evident that the velocity trend in the present study closely follows the results reported by Yao and Fang, (2012) at Re = 100.

Our present analytical results, obtained from Eq. (2.16), exhibit a closer match with the outcomes of the three-dimensional computational framework (ANSYS Fluent 2021 R1), especially at lower Reynolds numbers. This alignment is particularly noticeable in Fig. 2.3(a), where, in the absence of axial diffusion, the swirl velocity magnitude is nearly zero at $\mathrm{Re}=1$. However, when considering axial diffusion of swirl momentum (as shown in Fig. 2.3(a)), the swirl velocity demonstrates a significant non-zero value. Notably, this modified behavior due to the consideration of axial diffusion of swirl momentum distinguishes our results from the work of Yao and Fang, (2012). For lower Reynolds numbers, our analytical framework, incorporating axial flux of swirl momentum, excels in predicting the swirl velocity profile compared to the results of Yao and Fang, (2012) (as depicted in Fig. 2.3(a)), demonstrating a closer match with the three-dimensional numerical (ANSYS Fluent 2021 R1) solution. This improved agreement between our work and the simulated (3D) results, as observed in Fig. 2.3(a), is primarily attributed to the low Reynolds number regime considered in studying the transport phenomena and the relatively short axial length over which swirl decays completely. These findings suggest that the present analytical framework performs better for smaller tubes where Reynolds numbers are typically low, particularly in the context of flow and mixing applications (Suzuki et al., 2004; Dittrich and Manz, 2006; Jeong et al., 2010).

Additionally, in an effort to conserve computational cost and time in the current analysis, we integrate the obtained analytical velocity field (Eq. 2.16) to numerically solve the species transport Eq. (2.22). To ensure the credibility of the numerical results for the species transport problem, we conduct a grid independence test on our in-house finite volume code. The grid performance analysis, depicted in Fig. 2.3(b), involves the consideration of four sets of grids; $n_r \times n_\theta \times n_z$ = (40×140×1600), (50×200×2000), (60×260×2400) and (70×320×2800), where n_r, n_θ, and n_z are number of finite volumes in r, θ and z direction; we have plotted the mixing efficiency η_m along z for each set in Fig. 2.3(b). The other parameters considered for this test are: $\mathrm{Re} = 100$, $\mathrm{Pe} = 2600, r_t = 0.9$. From Fig. 2.3(b), it can be observed that the change in $n_r \times n_\theta \times n_z$ beyond $(60 \times 260 \times 2400)$ does not change the value of η_m significantly (ref. inset of Fig. 2.3(b)). Following this observation, in the subsequent analysis the mesh size with $n_r \times n_\theta \times n_z = (60 \times 260 \times 2400)$ is used.

2.4 Results and Discussion

In the introduction section, it has been highlighted that mixing efficiency in microchannels can be enhanced by generating vortices through either active or passive means. Researchers generally agree that the introduction of vortices along the mixing channel promotes chaotic mixing, facilitating efficient blending of two fluids within a shorter length scale and reduced residence time. It's noteworthy that the generated vortices in the mixing channel typically do not propagate throughout the entire channel; instead, they dissipate somewhere from the inlet. Therefore, to comprehend vortex-assisted mixing in a microchannel, we have developed a semi-analytical model coupled with the numerical framework outlined in Sections 2.1 and 2.2. The focus of the present work revolves around understanding the rate of change in Rankine vortex strength, represented henceforth by the swirl number parameter, along the flow direction and its impact on mixing. This is achieved by varying parameters such as Reynolds number (Re), Peclet number (Pe), Inlet Swirl number ($S(0)$), and transition radius (r_t).

2.4.1 Attributes of swirl by altering the parameters

Previous works by the researchers (Kaushik et al., 2012; Pati et al., 2013; Pati and Kumar, 2019) have indicated that the initial swirl number significantly influences swirl decay, regardless of the Reynolds number. Generally, swirl is categorized as strong or weak based on whether the swirl number is greater than or less than 1. To maintain the dominance between angular momentum and axial momentum, our study consistently considers the inlet swirl number to be 0.8, 1.0, and 1.2. Swirl number one value signifies an equal contribution of axial and angular momentum conditions at the inlet, as the swirl number is defined as the ratio of angular momentum flux to axial momentum flux. Any change in swirl intensity throughout our study reflects a compromise between these two factors. In our investigation, we briefly discuss the expected swirl velocity profile. According to the axis-symmetric and no-slip boundary conditions applied in the present study, the swirl velocity should be zero at the axis and wall. In Section 2.1, the swirl velocity is defined as a Rankine vortex, a combination of forced (core region) and free (annulus region) vortex, determined by a critical transition radius. Fundamentally, forced vortex represents rotational flows where the fluid rotates like a solid body, while free vortex corresponds to irrotational flows where the tangential velocity varies inversely with distance from the vortex's center. Pertaining to this condition, downstream, we anticipate the swirl velocity profile to exhibit a core region where the swirl velocity variation is linear in the radial direction. The swirl velocity profile should reach its maximum value, after which it starts to decrease outward along the radial direction in the outer region.

Before delving into the impact of the velocity field on mixing characteristics, it is crucial to discuss the velocity field and flow profile. The augmented flow induced by vortices plays a pivotal role in enhancing mixing characteristics. In this context, we briefly explore the behavior of the flow field, emphasizing the modified behavior resulting from the consideration of axial diffusion of swirl momentum, which distinguishes the present work from that of Yao and Fang, (2012). Furthermore, at the inlet, we set the swirl number, defined as the ratio of axial flux of angular momentum to axial flux of axial momentum, 0.8 to 1.2.

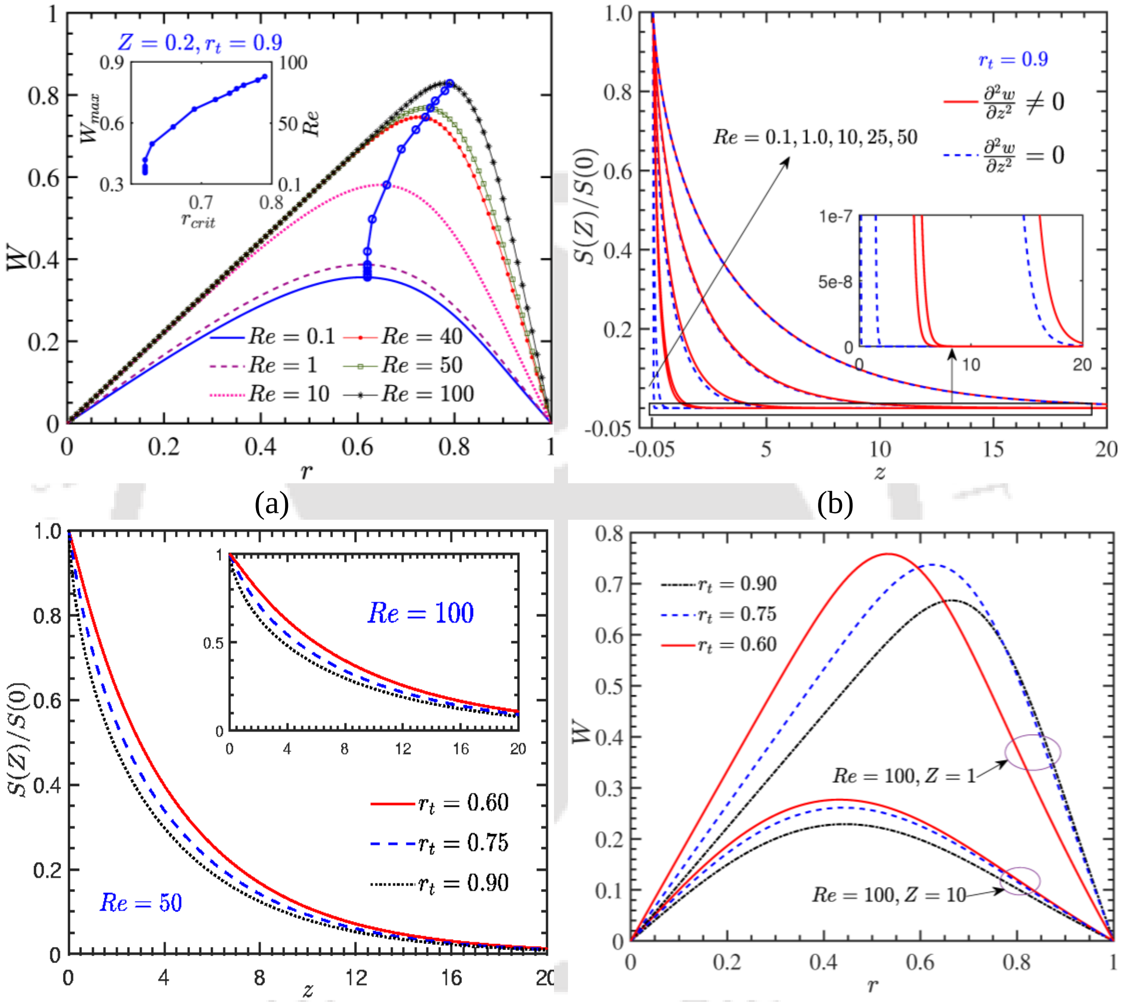

(a) (b)

(c) (d)

Figure 2.4: (a) Plots show the effect of Reynolds number on the critical transition radius for $r_t = 0.9$. The inset shown in figure (a) depicts the parabolic nature of the W_{max} variation with respect to critical transition radius. The values of Reynolds number considered for this analysis are: $\mathrm{Re} = 0.1, 1, 10, 40, 50, 100$. Plots in figures (b) and (c) respectively show the influence of Re and r_t on the swirl intensity. The values of parameters considered for this analysis are: (b) $\mathrm{Re} = 0.1, 1, 10, 25, 50$; $r_t = 0.9$ and (c) $\mathrm{Re} = 50$; $r_t = 0.60, 0.75, 0.90$. The inset in figure (b) show the zoomed in view of the $\mathrm{Re} = 0.1, 1, 10$ and also, inset in figure (c) show the variation of transition radius at $\mathrm{Re} = 100$. (d) Plots show the influence of the transition radius on the swirl velocity. The variation in transition radius is obtained here by considering different values of r_t *viz.*,$0.60, 0.75, 0.90$; $\mathrm{Re} = 100$.

The variation of swirl velocity profile along the radial direction of the channel is depicted in Fig. 2.4(a) for Re ranging between 0.1 to 100 and transition radius at the inlet

$r_t = 0.9$ at an axial location $z = 0.2$. It can be seen from Fig. 2.4(a) that the swirl velocity is a function of Re; increasing the value of the Reynolds number (beyond Re = 25), diminishes the effect of axial diffusion on the swirl velocity profile [see Fig. 2.3(a)]. The analytical swirl velocity profile shown in Fig. 2.4(a) is found to possess similar nature like experimental velocity profile as reported in literature (Bali, 1998). Increasing the Reynolds number tends to decrease the importance of diffusion terms as the inertia forces start to dominate and therefore, the present analytical result works better for lower Reynolds number transport as compared to the result reported by Yao and Fang, (2012). We note that at lower Reynolds numbers, the slow flow causes the diffusion of zero flow momentum from the pipe wall further into the flow field and we see lower values of peak dimensionless swirl velocities at smaller values of Re as observed in Fig. 2.4(a). On comparing Figs. 2.4(a) and 2.4(d), we observe that swirl velocity for Re = 100 and $r_t = 0.9$ is larger near the inlet section i.e., $z = 0.2$ compared to $z = 1$ and 10 [see Fig. 2.4(d)]; this phenomenon is the swirl decay.

Swirl decay is quantified in Figs. 2.4(b) and 2.4(c) by showing the variation of swirl intensity $S(z)/S(0)$ along the flow direction. The salient feature of considering axial diffusion of swirl momentum reveals a longer length required for complete decay of swirl, particularly at low Reynolds numbers [see inset of Fig. 2.4(b)]. For cases with higher Reynolds number condition, say $\text{Re} = 25$ and 50, because of higher axial velocity, swirl velocity penetrates deeper into the tube before complete decay. Having discussed the effect of Reynolds number on swirl velocity profile and swirl decay, we discuss the effect of dimensionless transition radius at the inlet (r_t), used to classify the Rankine vortex on swirl decay. The effect of parameter r_t is shown in Fig. 2.4(c) and we observe higher swirl decay length for lower r_t. This effect is true for both Reynolds numbers considered i.e., $\text{Re} = 50$ and $\text{Re} = 100$ [see inset of Fig. 2.4(c)]. Fig. 2.4(d) shows the variation in swirl velocity profile for different inlet transition radius at higher Reynolds number $\text{Re} = 100$. The fig. reveals the effect of decay of swirl momentum, where the peak moves closer to the axis of the pipe as the flow progresses downstream, due to the dominant viscous effects close to the pipe wall.

2.4.2 Attributes of swirl in mixing: Quantitative aspects

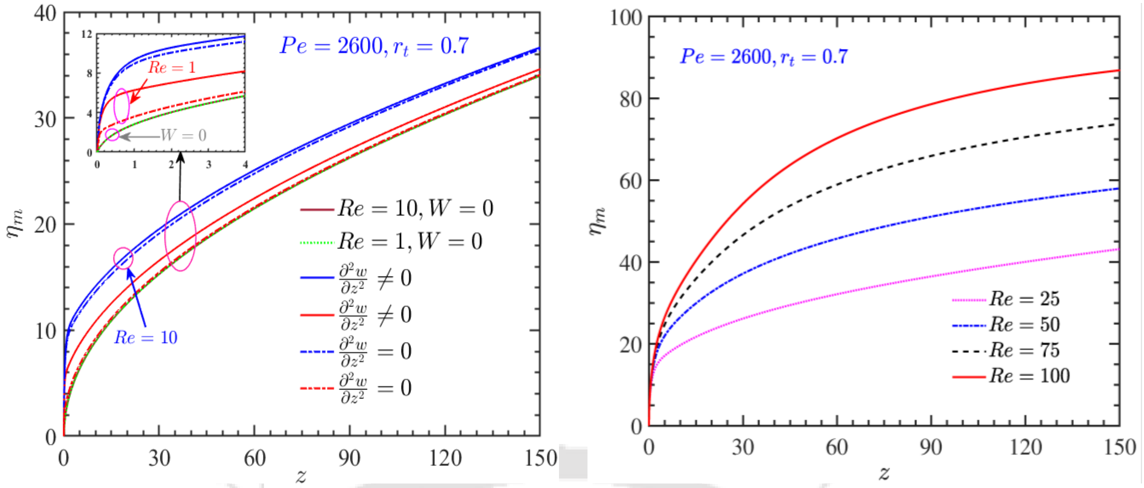

(a) (b)

Figure 2.5: (a) Plots show the influence of swirl velocity on the mixing efficiency over the total channel domain for different values of Reynolds number, Re $= 1, 10$, where $W = 0$ represents no swirl condition, $\partial^2 W/\partial z^2 \neq 0$ and $\partial^2 W/\partial z^2 = 0$ represent swirl with and without axial diffusion. The inset in figure (a) shows the zoomed in view of the Re $= 1, 10$ (b) Plots show the effect of Reynolds number on the mixing efficiency over the total channel length. The values of Re considered for this analysis are: Re $= 25, 50, 75$ and 100. The values of other parameters considered for the plots (a) and (b) are: Pe $= 2600, r_t = 0.7$.

Having elucidated the distinct effects of swirl velocity on flow dynamics, explicitly differentiating our present results from the discussion by Yao and Fang, (2012), we now redirect our focus to the influence of swirl velocity on mixing characteristics.

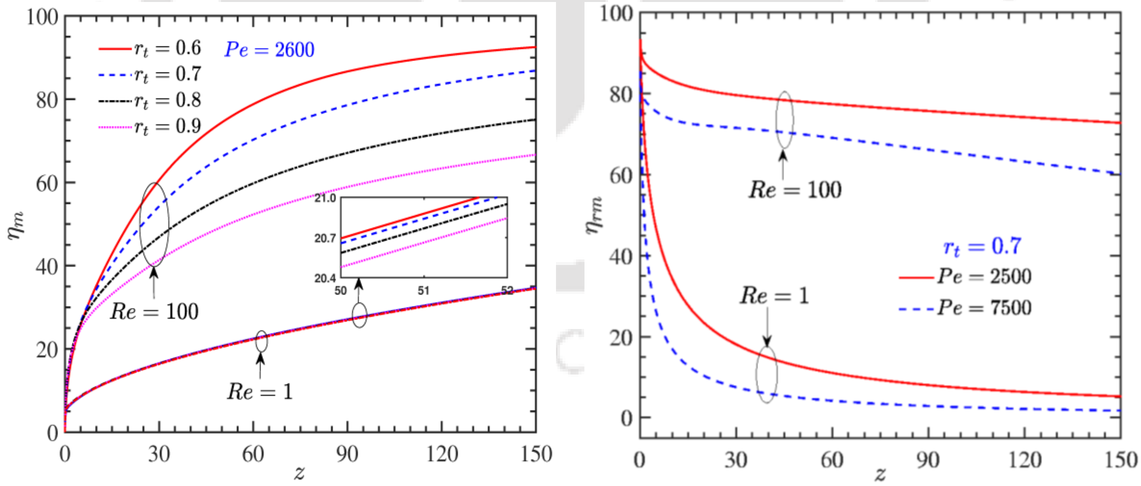

(a) (b)

Figure 2.6: Plots in figure (a) show the influence of transition radius r_t on the mixing efficiency over the total channel length and for Re $= 1$ and 100. The transition radius r_t is varied from 0.6 to 0.9 and the value of Peclet number, Pe $= 2600$. Plots in figure (b) showcase the relative mixing efficiency of channel for Re $= 1$ and 100, $r_t = 0.7$, Pe $= 2500$ and 7500.

The previous research by Bothe, et al., (2006), extensively characterized the mixing regimes in T-shaped micromixers, drawing conclusions that the mixing behavior varies significantly in each regime based on the Reynolds number. In the subsequent discussion, we delve into the impact of swirl decay on the mixing efficiency across the channel. Building upon the earlier discussion in subsection 2.4.1 regarding swirl velocity, where axial diffusion plays a crucial role in preventing swift decay of swirl momentum, especially at lower Reynolds numbers, we will now explore the qualitative aspects of mixing based on the obtained results. The effect of Reynolds number on mixing efficiency is illustrated in Figs. 2.5(a) and 2.5(b). A higher value of Reynolds number corresponds to increased mixing efficiency downstream of the channel, while maintaining a constant Peclet number $(\mathrm{Pe}=2600)$ and transition radius $(r_t = 0.7)$. Notably, a sudden increase in efficiency near the inlet is observed when the flow is assisted by swirl with axial diffusion (see Fig. 2.5(a)), particularly compared to scenarios without axial diffusion and without swirl at lower Re (=1, 10). For very small Reynolds numbers (Re ~ 1), a significant change in mixing efficiency is observed at the channel inlet when axial diffusion of swirl momentum is considered (see inset Fig. 2.5(a)). It is noteworthy that at Re = 10, considering axial diffusion of swirl momentum yields a mixing efficiency of 35% at the channel outlet. For slightly higher Reynolds numbers, it is observed that after the swirl has decayed, the mixing efficiency tends to remain higher than the case without swirl, attributed to the larger contact area between the two fluids. Fig. 2.5(b) demonstrates significantly higher mixing efficiency downstream for higher Reynolds numbers. Furthermore, at an axial location z, increasing Re from 10 to 100 results in the same efficiency of 35%, while shortening the channel length by 93.33%. Additionally, comparing Re = 10 and Re = 100 for a particular axial length, say $z=50$, the mixing efficiency in the case of $\mathrm{Re}=100$ is significantly higher.

It is important to understand the influence of inlet transition radius r_t on the efficiency of mixing as the flow proceeds through the channel and this is precisely plotted in Fig. 2.6(a) for $\mathrm{Re} = 1$ and 100. Decreasing the value of r_t, causes the efficiency of mixing to increase at the outlet of channel, shown in Fig. 2.6(a). Since transition radius does not have much influence on flow properties of low Reynolds number cases, we see distinct curves with slightly high $\mathrm{Re}(= 100)$ as seen in Fig. 2.6(a). To interpret the effect of swirl separately from the influence of molecular diffusion on the mixing, we define relative mixing parameter, defined as:

$$\eta_{rm}(z) = \left[\frac{\eta_m(z)|_W - \eta_m(z)|_{W=0}}{\eta_m(z)|_W} \right] \tag{2.27}$$

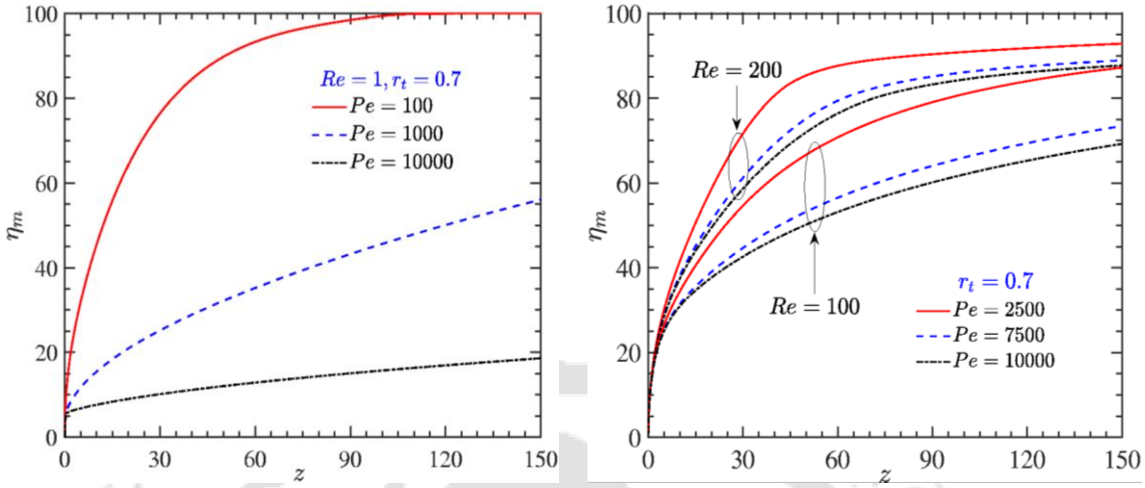

(a) (b)

Figure 2.7: Plots in figures (a)-(b) show the influence of Reynolds number and Peclet number on the mixing efficiency over the total channel length. The values of Reynolds number, Transition radius and Peclet number considered for these plots are: (a) $\mathrm{Re} = 1, r_t = 0.7, \mathrm{Pe} = 10^2, 10^3, 10^4$ (b) $\mathrm{Re} = 100$ and $200, r_t = 0.7, \mathrm{Pe} = 2500, 7500, 10000$.

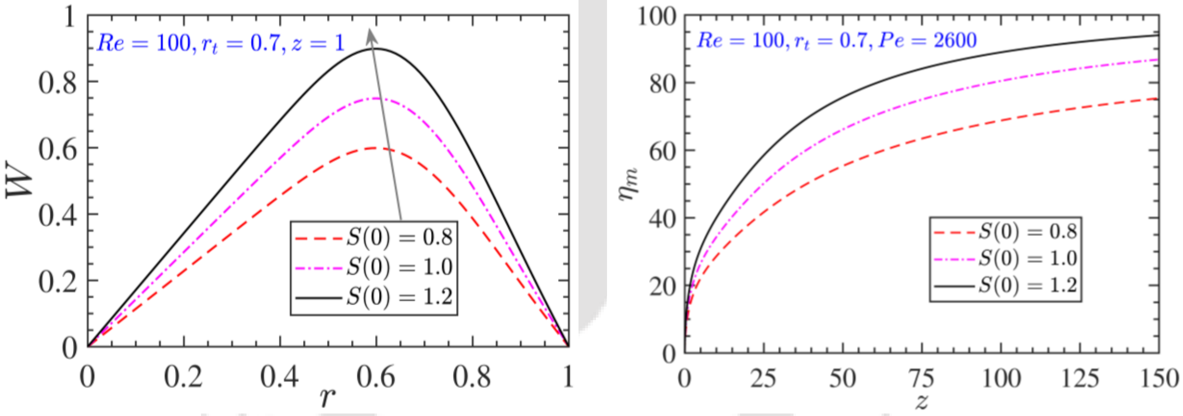

(a) (b)

Figure 2.8: The plots in figure (a) shows the swirl velocity profiles and in figure (b) shows the mixing efficiency along the channel length, for different values of inlet swirl number $S(0)$ = 0.8, 1.0, 1.2. The values of other parameters considered are: Re = 100, z = 1, r_t = 0.7, and Pe = 2600.

Relative mixing parameter along the length is shown in Fig. 2.6(b). This parameter is able to provide a scaled magnitude of the importance of swirl in mixing. We observe a 5 to 10% increase in mixing efficiency, for the Peclet numbers considered, when decaying swirl velocity is introduced into the flow field even at lower $\mathrm{Re}(= 1)$ as observed in Fig. 2.6(b). This figure also systematically verifies that the initial swirl velocity given to the flow moves the two fluids sufficiently enough to increase the surface area of contact between them, which causes higher mixing efficiency to persist further downstream even after the inlet swirl has completely decayed. Therefore, we infer that the mixing length for achieving complete mixing can be significantly reduced just by the addition of swirl velocity, despite its decay.

As molecular diffusion plays a significant role in mixing, we plot the Peclet number ranging from 10^2 to 10^4, for different Reynolds numbers in Figs. 2.7(a)-(b). While the primary focus of the study is to investigate the influence of convective effects on mixing performance, it is crucial to highlight that showcasing the possibility of achieving better mixing even in low Peclet number cases is of great importance. The effect of molecular diffusion is too significant -to be ignored in the discussion. From the earlier discussion, we established that convective effects dominate at higher Reynolds numbers up to a certain length of scale along the flow direction from the inlet. Further downstream, the mixing performance becomes solely dependent on molecular diffusion. Comparing the plots in Figs. 2.7(a) and 2.7(b), at a lower Reynolds number $(\mathrm{Re}=1)$, the efficiency of mixing is higher at lower Peclet numbers, as the strength of molecular diffusion increases with a decrease in Peclet number. In flows without swirl, the complete responsibility for mixing is carried out by molecular diffusion. In the present case, for Reynolds numbers of 100 and 200, we do not observe a significant reduction in mixing efficiency despite increasing the Peclet number from 2500 to 10000, as seen in Fig. 2.7(b). At higher Reynolds numbers, the lackluster mixing performance due to weak molecular diffusion may be overcome by introducing swirl at the inlet.

Further, Fig.2.8 shows the effect of inlet swirl number $S(0)$ on the swirl velocity and the mixing efficiency η_m. The inlet swirl number $S(0)$ considered for generating variation in these quantities W and η_m are 0.8, 1.0 and 1.2, where the other parameters are: Re = 100, z = 1, r_t = 0.7. For Fig.2.8(b), the value of Pe is 2600. In Fig.2.8, we observe that the swirl velocity, and mixing performance in terms of the mixing efficiency increases with an increment in the swirl number $S(0)$. The swirl number with its increasing magnitude augments the contribution of azimuthal momentum and reduces that of the axial momentum in the flow field. Therefore, with an increment in swirl number $S(0)$, the magnitude of swirl velocity (i.e., the velocity in the azimuthal direction) increases as shown in Fig.2.8(a). As seen in Fig.2.8(b), the effect of such increasing swirl velocity with swirl number $S(0)$ is found to be influencing the species transport phenomena or mixing as well. For higher values of the inlet swirl number for which the higher swirl velocity is obtained, the retention time of both candidate species for the given length of the channel increases and therefore, enhances the mixing efficiency to 95 % at $S(0)$ (= 1.2) as observed in Fig.2.8(b). Whereas in another case for which $S(0)$ is small ~ 0.8 or the axial momentum is quite higher as compared to the case of $S(0)$ (= 1.2), the candidate species nearly flush out of the channel leaving themselves partially mixed.

2.4.3 Attributes of swirl in mixing: Qualitative aspects

Contour plots depicting the concentration (C) obtained through our in-house finite volume code are shown in Figs. (2.9) and (2.10). Here, $C = 0$ and $C = 1$ denote the two unmixed fluids at the inlet, represented by blue and red colors, respectively. At the perfectly mixed state (depicted by the light green color), the concentration magnitude is close to 0.5. At lower Re, strong viscous effects prevent a complete revolution of fluids in the azimuthal direction. Instead, a small angular twist of the interface between the two fluids is observed. After this small twist, the swirl completely decays, and further mixing downstream occurs due to molecular diffusion. The Rankine vortex at the inlet rotates the interface of the two fluids differently at various radial locations, causing an elongation of the interface before the swirl has decayed. This elongation increases the surface area of contact between the two fluids, enhancing molecular diffusion. Even in the case of Re = 10, as shown in Fig. 2.9(b), fluid streams at the inlet are not subjected to complete rotation; instead, they are twisted to an angle greater than that of Re=1, as shown in Fig. 2.9(a). The efficiency of mixing at the outlet of the channel $(z = 150)$ for $\mathrm{Re} = 1$ and 10 is around 30% and 33%, respectively. The small increase is attributed to a slight increase in elongation of the interface between the two fluids. The contour plots shown in Fig. 2.10 depict the characteristics of swirl at a high Reynolds number $(\mathrm{Re} = 50,\ 100)$. At higher Reynolds numbers, there is sufficient inertia in the bulk fluid to rotate some radial locations of fluids either partially (180°) or completely (360°). The complete rotation at some radial locations causes stretching and folding of the fluid in bulk, leading to higher mixing downstream, as revealed in Fig. 2.10. Particularly at higher Re=100, as shown in Fig. 2.10(b), we observe an engulfment between the constituent fluids. Therefore, we may note that the complete rotation of the flow structure, especially when inertial effects dominate (i.e., higher Re), increases the contact surface between the fluids and strongly augments mixing. Having qualitatively

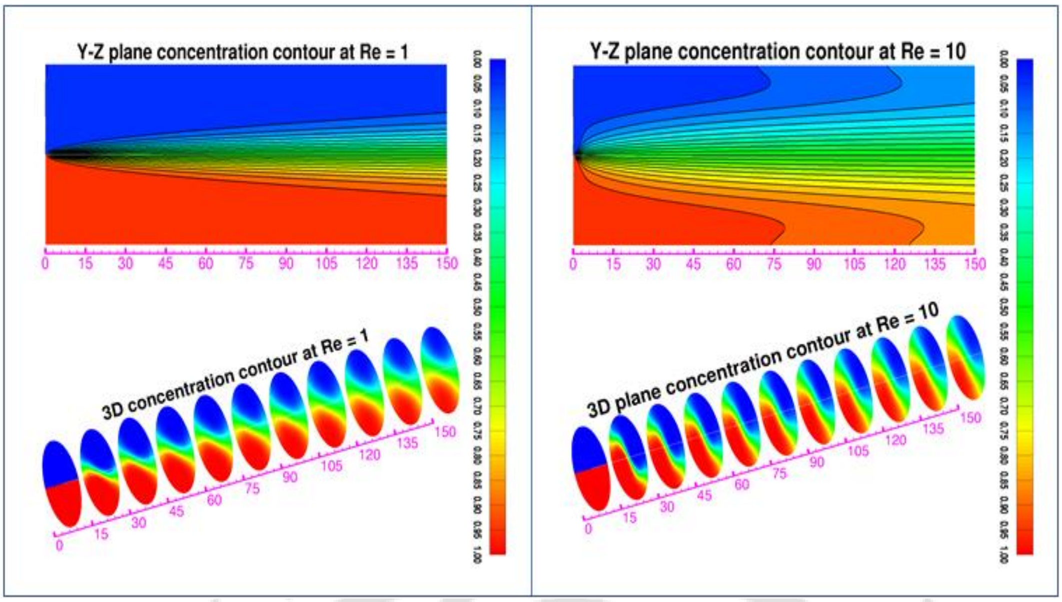

(a) (b)

Figure 2.9: Contour plot of concentration C at lower Reynolds number (a) Re = 1 and (b) Re = 10. The values of parameters considered for this figure are: $\mathrm{Pe} = 2600;\ r_t = 0.7$.

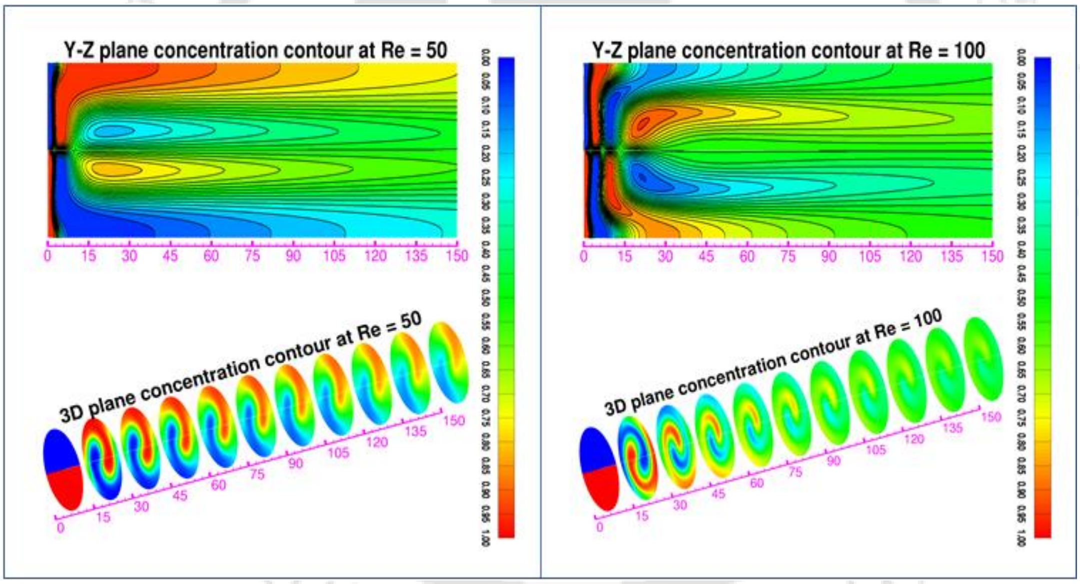

(a) (b)

Figure 2.10: Contour plot of concentration C at for higher Reynolds number (a) Re = 50 and (b) Re = 100. The values of parameters considered for this figure are: $\mathrm{Pe} = 2600;\ r_t = 0.7$.

- understood the effect of swirl on mixing, let's delve into the quantification of mixing. The swirl flow shears away from the fluid near the wall and increases the contact area of the fluid by approximately two times, as observed from the contour plots depicting the folding layer of fluid over another when compared with Re = 50. At z = 30, it can be inferred that the fluid undergoes another half rotation and then follows the same structure, with diffusive forces taking over through to the outlet of the channel. From the above-mentioned contour plots, one can also observe the stretching of fluid near the wall and axis at two different axial positions. As the fluid streams are subjected to a combination of tangential and axial velocity, we can demarcate the flow near the wall and the axis. Therefore, with the help of inferences obtained from the above discussion, we can critically comment that the rotation of the flow structure helps reduce the diffusion path and increases the contact surface between the fluids. From the swirl and axial velocity profiles, we can conclude that the fluid near the axis moves slowly due to strong swirl (rotation of fluid), signifying that the residence time of fluid is higher at the core of the tube. Therefore, we can assert that the mixing length for achieving complete mixing can be significantly reduced even when the swirl has decayed.

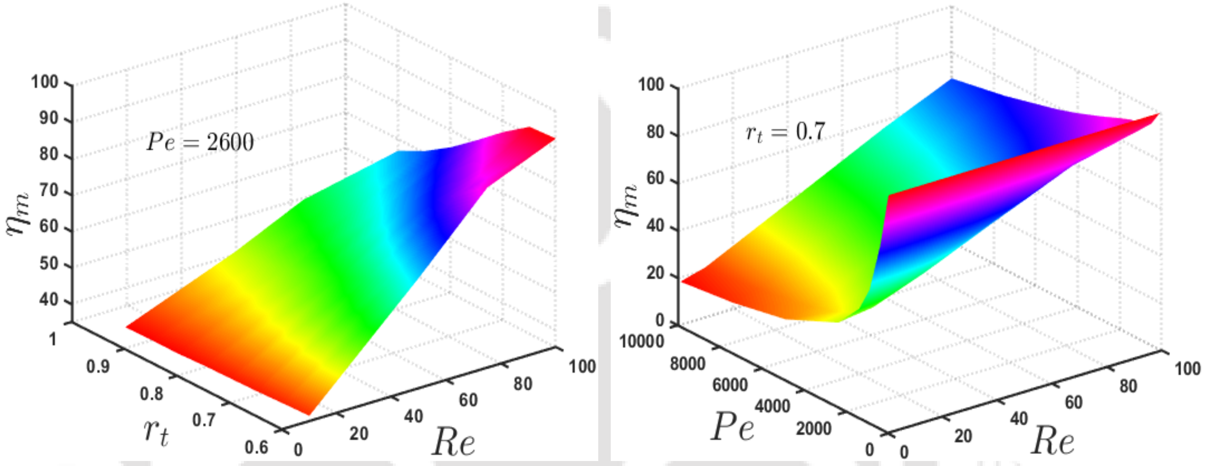

(a) (b)

Figure 2.11: 3D surface plot of mixing efficiency at the outlet of channel by varying the Re, r_t and Pe. For these plots, the values of parameters considered are: (a) Pe $= 2600$ and (d) $r_t = 0.7$.

To gain comprehensive insights into the mixing phenomenon influenced by various parameters such as Re, Pe and r_t, Figs. 2.11(a)-(b) present three-dimensional plots illustrating the variation in the efficiency of mixing at the outlet with respect to the parameters studied. From Fig. 2.11(a), it can be concluded that for a fixed value of Peclet number (Pe = 2600), decreasing the transition radius along with increasing the Reynolds number results in an increase in mixing efficiency, and vice versa. Similarly, Fig. 2.11(b) shows that for a fixed value of transition radius (r_t = 0.7), decreasing the Peclet number along with increasing Reynolds number leads to an increase in mixing efficiency, and vice versa. Fig. 2.11(a) provides comprehensive data for selecting the right swirl profile at the inlet to achieve the best mixing performance, while Fig. 2.11(b) offers a rough idea of the expected mixing when the Reynolds number and molecular diffusion strength are known.

2.4.4 Attributes of inlet swirl on transition mixing

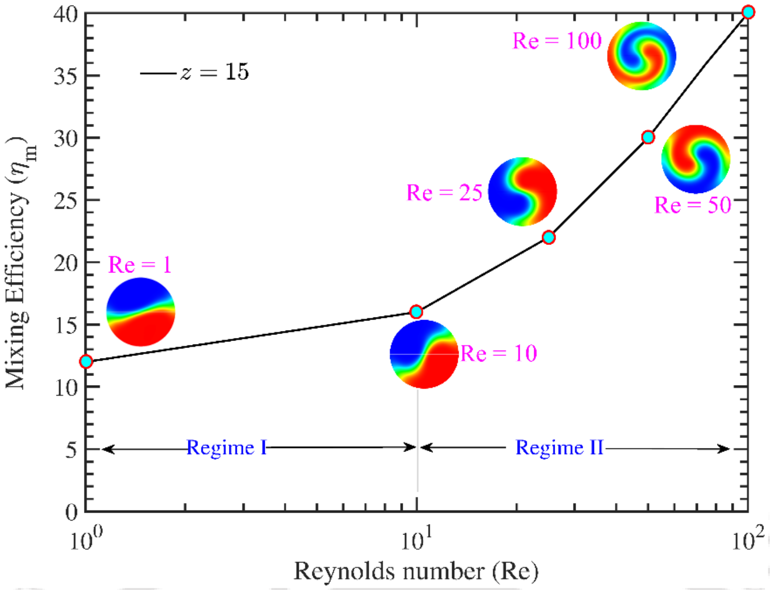

Figure 2.12: The plots in figure show the mixing transition with Reynolds number at an axial position of 15. Here, at Re = 10 divide the mixing based on inlet swirl in two regimes named as regime I and regime II to show the effect of molecular diffusion and chaotic convection, respectively. The values of other parameters considered are: $r_t = 0.7$, Pe = 2600.

In the present study, it is crucial to discuss the effect of Reynolds number on the transition in mixing, as illustrated by the concentration contours inset in Fig. 2.12. The transition is a consequence of the appearance and development of small-scale three-dimensional swirl motions in the flow field with Reynolds number, where the large excursions correspond to large vortex structures responsible for achieving convective-based mixing in shorter lengths (Breidenthal, 1981). The mixing transition based on vortex formation with inlet swirl is divided into flow regimes I and II. In regime I, mixing is achieved based on molecular diffusion attributed by the Peclet number, which follows a linear trend and is qualitatively shown by the inset concentration contours (see Fig. 2.9) at Re = 1 and 10. In regime II, a transition in mixing is observed, wherein the mixing product increases by an order of magnitude with Re > 10, following a non-linear trend with the convection as Re increases, as shown through the inset contours (Re = 25, 50, and 100) in Fig. 2.12. The concentration contours at Re = 25 conveys that convection-based mixing is dominant over molecular diffusion (see Fig. 2.4(b)), where the bulk fluid gets rotated by 90° and vortex starts to form. The effect of swirl on vortex formation is clearly shown through the inset contours of concentration. Above the transition, the amount of mixing is seen to be dependent on Reynolds number, and it is responsible for generating strong vortices that achieve chaotic-based mixing with swirl inlet.

2.5 Summary

In this study, a novel approach for achieving efficient vortex-induced mixing in a narrow fluidic cylindrical channel is proposed, emphasizing the impact of inlet swirl on convection under laminar flow conditions. The study reveals that how swirl flow affects the mixing of two similar fluids in a narrow cylindrical channel under low Reynolds number conditions. We analytically derive axial and swirl velocity profiles and use them to numerically solve the species transport equation for concentration distribution. Our exploration considers the impact of swirl and key parameters, including Reynolds number (Re ~ 0.1-10^2), Peclet number (Pe ~ 10^2-10^4), and transition radius of swirl velocity at the inlet r_t ~ 0.6-0.9), on mixing performance. The swirl velocity is found to rotate the bulk fluid tangentially, promoting efficient mixing through vortex formation normal to the flow direction. The role of swirl in rotating fluid structures and increasing contact surface area between fluids is demonstrated to be responsible for vortex-induced mixing within a short length scale from the channel inlet. Increasing Reynolds number and decreasing transition radius are identified as factors amplifying swirl magnitude, influenced by heightened radial pressure gradient and reduced wall shear stress. The study explores the effect of axial diffusion on swirl, revealing a longer decay rate length for larger Reynolds numbers and lower transition radius conditions. The study reveals that the inlet swirl has a significant influence, leading to the domination of convection in determining mixing strength. Specifically, a given inlet swirl, an increase in Reynolds number (Re) and a decrease in the transition radius at the channel inlet create conditions favourable for chaotic convection in the chosen pathway. Outcomes indicate that at lower Reynolds numbers (Re $\leq$ 10), molecular diffusion dominates mixing, whereas at higher Reynolds numbers (Re > 10), chaotic convection becomes a significant contributor. Furthermore, for Re $\geq$ 25, the role of molecular diffusion diminishes due to reduced fluid residence time. The study establishes that the addition of swirl velocity significantly reduces the length of the fluidic configuration required for efficient mixing, even after the complete decay of swirl in higher Reynolds number cases. The analysis underscores the influence of Reynolds and Peclet numbers on mixing efficiency, with molecular diffusion dominating at lower Reynolds numbers and chaotic convection playing a substantial role at higher Reynolds numbers. As Reynolds number further increases, molecular diffusion becomes insignificant, contributing valuable insights into vortex-assisted mixing in microfluidic confinement.

Chapter 3

Effective solute mixing of a non-Newtonian fluid within a cylindrical narrow fluidic channel, specifically in the presence of an inlet swirl

Recent advancements in micro/mini fluidic applications in the medical industry have sparked a growing interest in enhancing transport and mixing of non-Newtonian fluids. Although significant advancements in comprehending micromixing of non-Newtonian fluids, current research remains constrained to spiral or T-shaped rectangular channels. In this study, we conduct a theoretical examination, employing the Ostwald-de-Waele power-law model to derive analytical expressions for velocity fields of non-Newtonian viscoelastic fluid layers. The Navier-Stokes (NS) equations are solved for this purpose, and subsequent mixing considerations involve numerically coupling the obtained analytical velocity fields with the scalar species transport equation. We propose exploring swirl velocity as a passive mixing technique for non-Newtonian fluids, especially under laminar flow conditions. Our focus is on investigating the fundamental principles of decaying swirl and its impact on mixing biofluids. Specifically, we aim to analyze how fluid rheology, shaped by vorticial (swirl) flow in a narrow cylindrical channel, influences the comprehensive mixing process between two similar inelastic non-Newtonian fluids. The outcomes will be used to discuss both qualitative and quantitative aspects of the mixing process in the context of decaying swirl flow within the laminar regime.

3.1 Problem formulation and Mathematical model

In this study, we conduct a theoretical analysis to derive analytical expressions for the velocity fields of a non-Newtonian fluid, employing the Ostwald-de-Waele power-law model to characterize its rheology. We consider the underlying flow within a narrow cylindrical channel. Using the analytically derived velocity fields, we subsequently address the species transport equation to determine the concentration distribution along the chosen fluidic pathway.

3.1.1 Flow Configuration: Geometry and Description

We study the transportation of non-Newtonian fluids through a cylindrical microfluidic pipe with a radius (R) and length (L), as illustrated in Fig. 3.1. The coordinate system, defining the flow with coordinates r, θ, and z corresponding to velocity fields u_r, u_θ and u_z respectively, is attached to the inlet (left centre) of the channel. The inlet cross-sections for the entrances of fluids A and B are denoted by $\theta = [0, \pi]$ and $[\pi, 2\pi]$ respectively. This chosen configuration seems to mimic an application such as blood flow infused with other biological species/reagents or the mixing of a DNA carrier fluid with chemical reagents or fluorescent tracer particles (Cosentino et al., 2015). The concentrations of these fluids, like blood or DNA carrier fluids, are represented by zero concentration $(C_0 = 0)$, while the concentration of tracer particles or chemical reagents is denoted by higher concentration $(C_0 = 1)$ (refer to Fig. 3.1). The use of similar fluids justifies assuming constant thermophysical properties and non-Newtonian fluid behaviour in the underlying analysis.

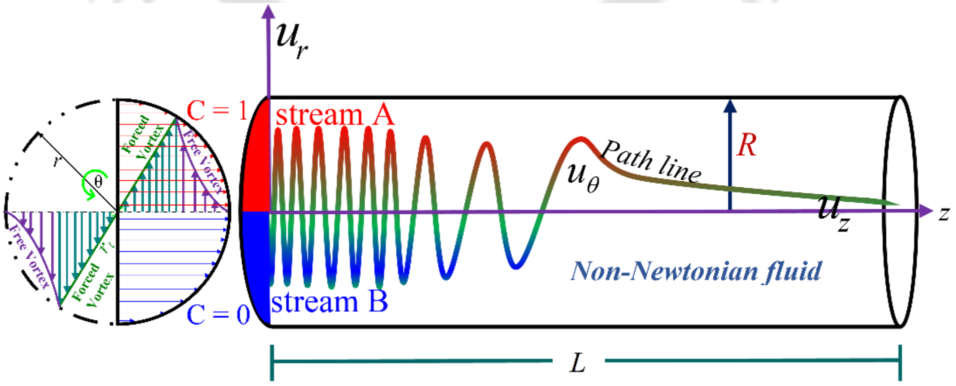

Figure 3.1: Schematic diagram describing the flow of non-Newtonian fluids with initial concentration 1 and 0 at the upper and lower domain at the inlet of pipe. A swirl motion consistent with the Rankine vortex is imposed at the pipe inlet. The coordinate system $(r\text{-}\theta\text{-}z)$ is attached at the centre of the pipe inlet.

Note that the fluids are considered to have same thermophysical properties and, therefore, one set of governing equations is solved for the flow field. Also, the characteristic length scale of the fluidic configurations, typical for biomicrofluidic setup, makes the underlying flow to be in the fully developed laminar regime (Re ~ 1 to 100) (Matsunaga and Nishino, 2014; Kaushik et al., 2022).

3.2 Momentum Transport: Governing Equations

The governing equations for the steady, incompressible, and laminar flow of a non-Newtonian fluid through the selected fluidic configuration, as depicted in Fig. 3.1, can be expressed using the mass and momentum transport equations in a cylindrical coordinate system (Deen, 2016). Here, we present the continuity and momentum transport equations in vectorial form to describe the inherent flow:

$$\nabla \cdot \mathbf{u} = 0 \tag{3.1}$$

$$\rho(\mathbf{u} \cdot \nabla)\mathbf{u} = -\nabla p + \nabla \cdot \boldsymbol{\tau} + \rho(\mathbf{g}(r, \theta, z)) \tag{3.2}$$

Note that in the above Eqs. (3.1 ~ 3.2), the velocity vector $\mathbf{u}(r, \theta, z) = u_r \mathbf{i}_r + u_\theta \mathbf{i}_\theta + u_z \mathbf{i}_z$ and $\nabla = (\partial/\partial r)\mathbf{i}_r + (\partial/r\partial\theta)\mathbf{i}_\theta + (\partial/\partial z)\mathbf{i}_z$.

The components of deviatoric stress tensor $(\boldsymbol{\tau})$ in cylindrical coordinate system for incompressible power-law fluid is given as (Bird et al., 2006; Deen, 2016):

$$\tau_{rr} = \mu_e\left(2\frac{\partial u_r}{\partial r}\right), \tau_{\theta\theta} = \mu_e \frac{2}{r}\left(\frac{\partial u_\theta}{\partial \theta} + u_r\right), \tau_{zz} = \mu_e\left(2\frac{\partial u_z}{\partial z}\right), \tau_{r\theta} = \tau_{\theta r} = \mu_e\left(r\frac{\partial}{\partial r}\left(\frac{u_\theta}{r}\right) + \frac{1}{r}\frac{\partial u_r}{\partial \theta}\right), \tau_{\theta z} = \tau_{z\theta} = \mu_e\left(\frac{\partial u_\theta}{\partial z} + \frac{1}{r}\frac{\partial u_z}{\partial \theta}\right), \tau_{zr} = \tau_{rz} = \mu_e\left(\frac{\partial u_z}{\partial r} + \frac{\partial u_r}{\partial z}\right) \tag{3.3}$$

Here, μ_e is the effective viscosity for the power-law fluid and it is given as: $\mu_e = \mu_0\left(\sqrt{0.5(\mathbf{D}:\mathbf{D})}\right)^{n-1}$, where, μ_0 is the flow consistency index; *n* is the power-law index and **D** stands for the deformation tensor defined as: $\mathbf{D} := \nabla\mathbf{u} + (\nabla\mathbf{u})^T$:

$$\mathbf{D} = \frac{1}{2}\begin{bmatrix} \left(2\frac{\partial u_r}{\partial r}\right) & \left(r\frac{\partial}{\partial r}\left(\frac{u_\theta}{r}\right) + \frac{1}{r}\frac{\partial u_r}{\partial \theta}\right) & \left(\frac{\partial u_z}{\partial r} + \frac{\partial u_r}{\partial z}\right) \\ \left(r\frac{\partial}{\partial r}\left(\frac{u_\theta}{r}\right) + \frac{1}{r}\frac{\partial u_r}{\partial \theta}\right) & \frac{2}{r}\left(\frac{\partial u_\theta}{\partial \theta} + u_r\right) & \left(\frac{\partial u_\theta}{\partial z} + \frac{1}{r}\frac{\partial u_z}{\partial \theta}\right) \\ \left(\frac{\partial u_z}{\partial r} + \frac{\partial u_r}{\partial z}\right) & \left(\frac{\partial u_\theta}{\partial z} + \frac{1}{r}\frac{\partial u_z}{\partial \theta}\right) & \left(2\frac{\partial u_z}{\partial z}\right) \end{bmatrix}$$

To solve Eqs. (3.1 ~ 3.2) analytically, we consider the physically justified assumption that the flow is axis-symmetric, with negligible body force, and that it becomes fully developed along the axial direction, i.e., $u_z = u_z(r)$ (Kumar et al., 2020). Additionally, we disregard the body force term. Considering the aforementioned assumptions, the component of flow velocity in radial direction is calculated to be constant using the continuity Eq. (3.1) and proven to be zero ($u_r = 0$) consistent with the no-slip condition at the wall. Taking this radial velocity condition into consideration, we proceed to calculate the velocity components in both the axial and tangential directions. Moving forward with this assumption and utilizing Eq. (3.3), the momentum transport equation in the radial direction simplifies to $\rho\left(u_\theta^2/r\right) = \partial p/\partial r$. This relation establishes the connection between the radial pressure gradient and the tangential velocity component. The derived equation reveals that the radial variation of pressure serves the purpose of supplying the force required to sustain the movement of fluid elements along a circular path within the channel.

Consequently, to solve the momentum transport Eq. (3.2), the physically justified boundary conditions, based on aforementioned discussion and assumptions, in compact form are given as: $u_r = 0$; $\partial u_z/\partial r|_{r=0} = 0$, $u_z(r)|_{r=R} = 0$; $u_\theta(r,z)|_{r=0} = 0$, $u_\theta(r,z)|_{r=R} = 0$. At the inlet ($z = 0$) of considered fluidic configuration, Rankine vortex (Greitzer et al., 2007; Yao and Fang, 2012; Shtern, 2018; Kumar et al., 2020) is imposed to create the swirl, i.e., $u_\theta(r,z)|_{z=0} = \left\{\left(u_{\theta,i,max}\right)\frac{r}{r_t}, r \le r_t \text{ and } \left(u_{\theta,i,max}\right)\frac{r_t(R-r)}{r(R-r_t)}, r \ge r_t\right.$. Here, $u_{\theta,i,max}$ and r_t represent the maximum inlet swirl velocity and transition radius respectively. The dimensional transition radius, denoted as r_t, signifies the point where the transition from forced to free vortex occurs at the channel inlet. Now, in order to solve the azimuthal flow velocity component, the initial step involves solving the axial momentum. Subsequently, the solution obtained for axial momentum is combined or superimposed to derive the tangential velocity component.

3.2.1 Analytical solution of fluid flow equations

By employing the continuity equation ($u_r = 0$), we write the reduced form of the momentum transport Eq. (3.2) in the axial direction with negligible body forces as given below:

$$0 = -\frac{\partial p}{\partial z} + \left[\frac{1}{r}\frac{\partial}{\partial r}(r\tau_{rz})\right] = -\frac{\partial p}{\partial z} + \left[\frac{1}{r}\frac{\partial}{\partial r}\left(r\mu_e\left(\frac{\partial u_z}{\partial r}\right)\right)\right] \tag{3.4}$$

To obtain equation (3.4), we appeal to the components of the deviatoric stress tensor through Eq. (3.3) and use axisymmetric $(\partial/\partial\theta = 0)$ as well as fully developed flow $(u_z = u_z(r))$ assumptions.

In addition, with the order of magnitude analysis, the effective viscosity is derived as: $\mu_e = \mu_0|\partial u_z/\partial r|^{n-1}$ (Sarma et al., 2017). Substituting the value of μ_e and employing the boundary conditions, i.e., $\partial u_z/\partial r|_{r=0} = 0$ and $u_z(r/R = 1) = 0$, respectively, we solve Eq. (3.4) for the expression of axial velocity, which reads as:

$$u_z = \left(\frac{n}{n+1}\right)\left(\frac{R^{n+1}|\Delta p|}{2\mu_0 L}\right)^{\frac{1}{n}}\left[1-\left(\frac{r}{R}\right)^{\frac{n+1}{n}}\right] = \left(\frac{3n+1}{n+1}\right)u_{av}\left[1-\left(\frac{r}{R}\right)^{\frac{n+1}{n}}\right] \tag{3.5}$$

In Eq. (3.5), $u_{av} = \int u_z dA/\int dA = (n/(3n+1))((R^{n+1}|\Delta p|)/(2\mu_0 L))^{\frac{1}{n}}$, represents the average axial flow velocity.

We write the simplified form of Eq. (3.2) using the aforementioned assumptions to obtain the tangential momentum equation as given below:

$$u_z\frac{\partial u_\theta}{\partial z} = \frac{1}{\rho}\left[\frac{1}{r^2}\frac{\partial}{\partial r}(r^2\tau_{r\theta}) + \frac{\partial}{\partial z}(\tau_{\theta z})\right] = \frac{1}{\rho}\left[\frac{1}{r^2}\frac{\partial}{\partial r}\left(r^2\mu_e\left(r\frac{\partial}{\partial r}\left(\frac{u_\theta}{r}\right)\right)\right) + \frac{\partial}{\partial z}\left(\mu_e\left(\frac{\partial u_\theta}{\partial z}\right)\right)\right] \tag{3.6}$$

Employing the previously discussed assumptions and utilizing the deviatoric stress components outlined in Eq. (3.3), we endeavor to express Eq. (3.6) in a reduced form. It is essential to note that Eq. (3.6) represents the reduced version of the tangential momentum equation, achieved through the incorporation of specific assumptions such as axisymmetric flow $(\partial/\partial\theta = 0)$, fully developed flow $(u_z = u_z(r))$, and adherence to the continuity equation $(u_r = 0)$, as discussed in Section 3.2. As evident in Eq. (3.6), the axial diffusion term, i.e., $\partial^2 u_\theta/\partial z^2$, has been omitted. To substantiate this exclusion, an order of magnitude analysis is performed. This analysis introduces swirl motion at the inlet to facilitate enhanced mixing. Despite the imposition of swirl motion, it is observed that the magnitude of tangential velocity (u_θ) remains lesser than the axial velocity (u_z), even in the regime very close to the pipe inlet. Noteworthy is the consideration of L = 120R in this analysis, indicating that $R \ll L$. Consequently, the relatively smaller magnitude of tangential velocity, coupled with the larger axial length, justifies the exclusion of the axial diffusion term. The order of magnitude analysis reveals $\partial^2 u_\theta/\partial z^2 \sim u_\theta/L^2 << 1$, affirming that the magnitude of the axial diffusion term is significantly smaller than the diffusion in the radial direction. In line with this order of magnitude analysis, the axial diffusion term is omitted in Eq. (3.6). Upon substituting the effective viscosity $\mu_e = \mu_0 |\partial u_z/\partial r|^{n-1}$ (Sarma et al., 2017) in Eq. (3.6) (Sarma et al., 2017), the dimensionless form of Eq. (3.6) is derived as follows:

$$K_0 U r^2 \frac{\partial W}{\partial Z} = \left[\frac{\partial}{\partial r}\left(r^{\frac{3n-1}{n}}\right)\left(\frac{\partial W}{\partial r} - \frac{W}{r}\right)\right] \tag{3.7}$$

In Eq. (3.7), the term $K_0 = \mathrm{Re}(-1)^{n-1}(n/(3n+1))^{n-1}$; where Reynolds number, $\mathrm{Re} = \rho u_{av}^{2-n} R^n/\mu_0$. Here, K_0 is analysed under the consideration of real values while varying the power-law index, *n*. The dimensionless variables appearing in Eq. (3.7) are: $U(r) = u_z/u_{av}$; $W(z,r) = u_\theta/u_{av}$; $r \sim r^* = r/R$; $z \sim z^* = z/R$, $r_t \sim r_t^* = r_t/R$; where r_t^* represents the non-dimensional transition radius between forced and free vortex.

To solve Eq. (3.7), which is a non-linear partial differential equation, we apply axisymmetric and no-slip boundary conditions with $W(z, r=0) = 0$ and $W(z, r=1) = 0$, respectively. Note that a rankine vortex is imposed at the inlet (*z* = 0) to create the swirl motion therein. The dimensionless form of Rankine vortex is given by (Greitzer et al., 2007; Yao and Fang, 2012; Shtern, 2018; Kumar et al., 2020):

$$W(z=0,r) = \begin{cases} \frac{u_{\theta,i,max}}{u_{av}} \frac{r}{r_t}, r \le r_t \text{ and } \frac{u_{\theta,i,max}}{u_{av}} \frac{r_t(1-r)}{r(1-r_t)}, r \ge r_t \end{cases} \tag{3.8}$$

In this endeavour, we look for the analytical solution for the tangential velocity component, we employ a method akin to the separation of variables, defining $W(z,r) = (F(z))(G(r))$. This approach allows us to solve the non-linear partial differential equation, Eq. (3.7), and ultimately derive the tangential velocity component.

Further, to obtain the analytical series solution, we consider λ as constant positive real eigen value and make use of the axisymmetric boundary condition (i.e., $W(z,\ 0) = 0$). We obtain the swirl flow velocity $W(z,\ r)$ in terms of eigen values (λ_m; where $m = 1, 2, \ldots \infty$) and by using symbolic notation for function WhittakerM as:

$$\mathrm{WhitM}_{m,n} = \mathrm{WhittakerM}\left[\frac{n\lambda_m\sqrt{3n+1}}{(2(n+1)^{3/2})}, \frac{3n-1}{(2n+2)}, \frac{(2n\lambda_m)r^{\left(\frac{n+1}{n}\right)}\sqrt{3n+1}}{(n+1)^{3/2}}\right].$$

Below we present the swirl velocity profile by utilizing the above notation for the Whittaker function (WhittakerM) as “$\mathrm{WhitM}_{m,n}$” as follows:

$$W(z,r) = \sum_{m=1}^{\infty} C_m \exp(-\lambda_m^2 z/K_0)\left(\mathrm{WhitM}_{m,n}/r\right) \quad (3.9)$$

This representation encapsulates the analytical solution for the tangential velocity component, incorporating the eigenvalues and adhering to the specified boundary conditions. Here, $\mathrm{WhittakerM}(a,b,r)$ is the special function for the solution of Whittaker’s equation. Note that $\mathrm{WhittakerM}(a,b,r)$ is the modified form of the confluent hypergeometric equation and it is defined as:(Whittaker, 1903; Abramowitz and Stegun, 1968) $\mathrm{WhittakerM}(a,b,r) = (\exp(-0.5r))(r^{b+0.5})\, M(b-a+0.5, 1+2b,\ r)$, where $\mathrm{M}(a,b,r) = \sum_{m=0}^{\infty} \frac{(a^m)(r^m)}{(b^m)(m!)}$ is Kummer’s confluent hypergeometric function.

Substituting the value of power-law index $n = 1$, representing a special case of Newtonian fluid, the solution can be written as:

$$W(z,r) = \sum_{m=1}^{\infty} C_m \exp(-(\lambda_m^2)z/\mathrm{Re})\left(\mathrm{WhittakerM}\left[\frac{\lambda_m}{2\sqrt{2}}, \frac{1}{2}, \sqrt{2}\lambda_m r^2\right]\right)/r \quad (3.10)$$

We consider the first thirty (30) eigen values of Eq. (3.9), obtained using no-slip boundary condition, i.e., $W(z,\ r=1) = 0$, to get the convergence of the order 10^{-12} for different values of power-law index (n = 0.8, 1.0, 1.2). Employing this specified boundary condition, i.e., $W(z,\ r=1) = 0$;

$$\sum_{m=1}^{\infty} \mathrm{WhittakerM}\left[\frac{n\lambda_m\sqrt{3n+1}}{(2(n+1)^{3/2})}, \frac{3n-1}{(2n+2)}, \frac{(2n\lambda_m)\sqrt{3n+1}}{(n+1)^{3/2}}\right] = 0$$

We derived the above expression to obtain the eigenvalues. We consider a numerical method, consistent with the iterative approach, to determine the eigenvalues of the function, $f = \sum_{m=1}^{\infty} \mathrm{WhittakerM}\left[\frac{n\lambda_m\sqrt{3n+1}}{(2(n+1)^{3/2})}, \frac{3n-1}{(2n+2)}, \frac{(2n\lambda_m)\sqrt{3n+1}}{(n+1)^{3/2}}\right] = 0$. The method is applied for different values of n, assuming that f is a continuous function. The characteristic function f is considered to possess m real roots as denoted by λ_1, λ_2, ... and λm. The roots of the real-valued function $f = 0$ are determined using the bisection method (Grassia, 2020). In this method, the interval limits [a, b] for first iteration are initially set to lower bound a = 1 and upper bound b = 4. The subsequent finite eigenvalues (λ_i, where i = 1,2,…30) are calculated by ensuring that the condition

$(f(a) \times f(b)) < 0$ is satisfied, indicating that the roots are located within the specified interval. Here, the bisection method is chosen for its simplicity, reliability, and effectiveness in finding isolated single roots in a fixed range. In Table 3.1, we present only the first ten (10) eigen values for different values of power-law index (n = 0.8, 1.2), including n = 1.0 (Newtonian fluid). It may be added here that we undertake an effort to cross-verify our solution methodology, and in doing so, we compare the calculated eigen values for n = 1 with the reported results of Yao & Fang (2012), included in Table 3.1 as well. Important to mention, the calculated eigen values for n = 1.0 conform to those as reported by Yao & Fang (2012). By appealing to Sturm-Liouville theorem (Kaplan 1981), we calculate the value of C_m, a coefficient appearing in Eq. (3.9), by applying the orthogonality condition of the eigen-functions. We establish orthogonality conditions by considering distinct eigenvalues, denoted as λ_m and λ_{m1}. Specifically, when $\lambda_m \neq \lambda_{m1}$, we rely on the Sturm–Liouville theorem (Kaplan 1981), employing a weight function defined as $r\left(1 - r^{(n+1/n)}\right)$, within the interval [0,1]. This weight function ensures orthogonality of the eigenfunctions. The orthogonality condition is expressed as follows:

$$\int_{r=0}^{r=1} \frac{\mathrm{WhittakerM}\left[\frac{n\lambda_m\sqrt{3n+1}}{(2(n+1)^{3/2})}, \frac{3n-1}{(2n+2)}, \frac{(2n\lambda_m)r^{\left(\frac{n+1}{n}\right)}\sqrt{3n+1}}{(n+1)^{3/2}}\right]}{r} \frac{\mathrm{WhittakerM}\left[\frac{n\lambda_{m1}\sqrt{3n+1}}{(2(n+1)^{3/2})}, \frac{3n-1}{(2n+2)}, \frac{(2n\lambda_{m1})r^{\left(\frac{n+1}{n}\right)}\sqrt{3n+1}}{(n+1)^{3/2}}\right]}{r} r\left(1 - r^{\left(\frac{n+1}{n}\right)}\right) dr = 0$$

m	$n = 0.8, \lambda_m$	$n = 1.0, \lambda_m$	$n = 1.2, \lambda_m$
1.	3.43962	3.26973	3.14988
2.	6.72326	6.11470	5.70642
3.	10.00036	8.94845	8.24912
4.	13.27591	11.77938	10.78820
5.	16.55087	14.60923	13.32586
6.	19.82557	17.43855	15.86282
7.	23.10011	20.26760	18.39940
8.	26.37457	23.09647	20.93575
9.	29.64897	25.92523	23.47194
10.	32.92333	28.75392	26.00804

Table 3.1. The first ten eigenvalues for the generalized Whittaker function having values of power-law index, n = 0.8, 1.0, and 1.2.

Utilizing the Sturm-Liouville theorem and the orthogonality of eigenfunctions at $\lambda_m = \lambda_{m1}$, with the inlet condition (3.8), the coefficient C_m mentioned in (3.9) can be obtained as:

$$C_m = \int_{r=0}^{r=1} W(0,r)\left(\mathrm{WhitM}_{m,n}\right)\left(1 - r^{\left(\frac{n+1}{n}\right)}\right) dr \Big/ \left(\int_{r=0}^{r=1} \left[\frac{(\mathrm{WhitM}_{m,n})}{r}\right]^2 r\left(1 - r^{\left(\frac{n+1}{n}\right)}\right) dr\right) \quad (3.11)$$

In order to quantify the intensity of swirl along the channel, we define below in Eq. (3.12) a dimensionless swirl number $S(z)$ as the ratio of the axial flux of angular momentum to the axial flux of axial momentum at a particular cross-section (Reader-Harris, 1994; Alekseenko et al., 1999; Maddahian et al., 2011).

$$S(z) = \int_0^R u_z^* u_\theta^* r^{*2} dr^* \Big/ \left(R \int_0^R u_z^{*2} r^* dr^*\right) = \int_{r=0}^{r=1} U W r^2 dr \Big/ \left(\int_{r=0}^{r=1} U^2 r dr\right) \quad (3.12)$$

Using Eqs. (3.8) and (3.9) in (3.12), the ratio $S(z)/S(0)$, i.e., the ratio of swirl number $S(z)$ at any axial location to the inlet can be obtained as:

$$\frac{S(z)}{S(0)} = \frac{\sum_{m=1}^{\infty} C_m \exp\left(-\lambda_m^2 z/K_0\right) \int_{r=0}^{r=1} \left(\mathrm{WhitM}_{m,n}\right) r \left(1 - r^{\left(\frac{n+1}{n}\right)}\right) dr}{\int_{r=0}^{r=1} W(0,r) r^2 \left(1 - r^{\left(\frac{n+1}{n}\right)}\right) dr} \quad (3.13)$$

After deriving the analytical expressions for both axial and tangential velocity profiles, we proceed to assess the mixing of two fluids/solutes in the following subsection. In this section, we initially determine the spatial distribution of species concentration along the selected fluidic pathway. Subsequently, we compute the associated mixing efficiency for various power-law index values.

3.2.2 Benchmarking of Analytical method and selection of parameters

To substantiate the efficacy of the proposed theoretical framework, we employ a triple benchmarking strategy, as illustrated in Figs. 3.2(a)-(c). In Fig. 3.2(a), we depict the swirl velocity profile derived from our theoretical framework under the limiting case of a Newtonian fluid, where *n* = 1, considering two different Reynolds numbers (Re = 10, 100). This profile is compared with the reported results from Yao and Fang, (2012). The parameters for this plot include z = 1 and r_t = 0.9. Notably, in obtaining the analytical solution for swirl velocity using Eq. (3.10), the values of λ_m, crucial for satisfying the no-slip boundary condition i.e., $W(z, r = 1) = 0$, remain independent of the Reynolds number. It is worth mentioning that analytical solutions for both no-slip and slip cases have been established in the literature (Kumar et al., 2020).

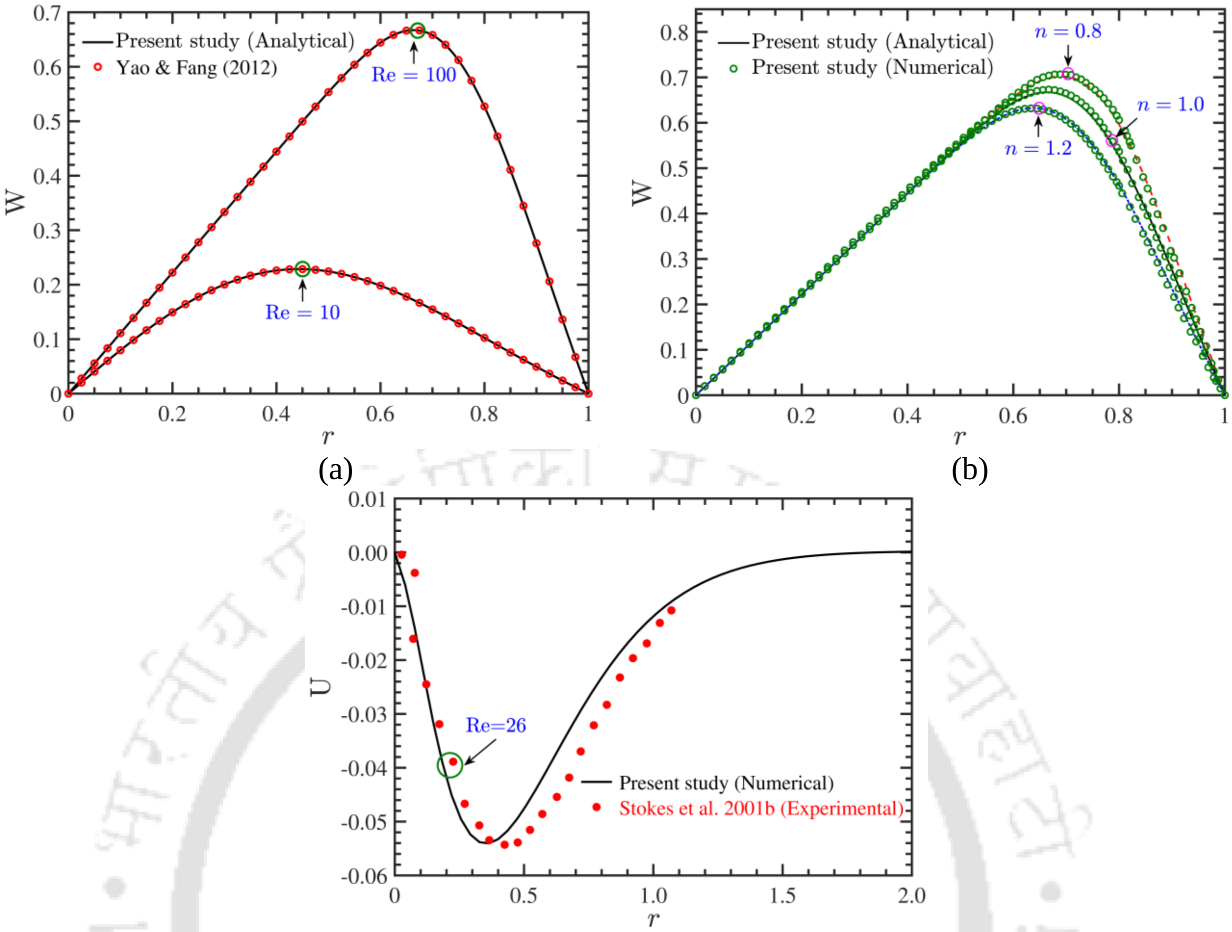

(a)

(b)

(c)

Figure 3.2: Validation of present analytical swirl velocity profile with (a) Yao and Fang, (2012) at Re = 10 and 100 for Newtonian fluid ($n = 1.0$) and (b) with the three-dimensional numerical simulation (ANSYS) results for non-Newtonian fluid at power-law index, $n = 0.8, 1.0, 1.2$. The other parameters considered for validation are: Re = 100, Axial location, $z = 1$ and transition radius, $r_t = 0.9$. (c) Represents the validation of existing experimental results of axial velocity profile and present numerical model at Re = 26 with limiting case for Newtonian fluid, $n = 1$.

To ensure the convergence of our results, we conducted a validation analysis in Fig. 3.2(a) by comparing the eigenvalues obtained from our calculations with those reported by Yao and Fang, (2012) for Re = 10 and 100. This benchmarking effort serves to validate the accuracy and consistency of our results. The close agreement between our present findings and the published results, as observed in Fig. 3.2(a), attests to the efficacy of our proposed analytical model.

Effort has been taken in Fig. 3.2(b) to compare our analytical solutions of flow velocity for different non-Newtonian fluids, including both shear-thinning (n = 0.8) and shear-thickening (n = 1.2) fluids with the corresponding full-scale simulated results. For this validation, we performed three-dimensional simulations employing finite volume framework of ANSYS Fluent 2021 R1 in parallel mode and considering identical flow configuration as chosen in this endeavour. For the simulations, we used workstation having the specifications as follows: 8 cores with 16 logical processor, ram 32 GB and base speed 3.41 GHz. For the plots depicted in Fig. 3.2(b), the other parameters are z = 1, r_t = 0.9 at Re = 100. To ascertain the credibility of the theoretical framework developed in our analysis; precisely, to ascertain the correctness of analytical solutions, obtained considering a few assumptions, we performed another validation to compare analytically obtained of flow velocity for non-Newtonian fluids (shear-thinning, shear-thickening fluids) with the full-scale simulated results. We wish to emphasize that the use of Finite Volume Method (FVM) framework of ANSYS Fluent 2021 R1 is employed in this study to obtain simulated results and subsequently to validate them with the analytical results as presented in Fig. 3.2(b). We obtain a closer match between analytical swirl velocity profiles and the corresponding numerical results for three different values of power-law index (n) of 0.8, 1.0, and 1.2, as shown in Fig. 3.2(b). The comparison analysis presented in Fig. 3.2(b) underscores that our analytical solutions, obtained by considering a few physically justified assumptions, faithfully capture the full-scale (three-dimensional) simulated results. It is imperative to note that the validation of the analytical results through a comparison with full scale numerical simulations using the ANSYS Fluent 2021 R1 underlines the credibility of the proposed analytical framework. For the sake of completeness, we mention here that simulations are performed considering a total number of 12081477 control volumes and assigning residual criteria of 10^{-7} for all the transport variables. As evident from Fig. 3.2(b), analytical calculations obtained for all the values of n (= 0.8, 1.0 1.2) match in a fairly accurate manner with the simulated results.

Furthermore, we undertake an effort in Fig. 3.2(c) to compare the simulated axial velocity profile with the experimental results available in this paradigm (Stokes et al., 2001). It is worth mentioning here that the experimental validation is limited to Newtonian fluid (n = 1.0), while parameters considered are as follows: Re = 26 and r_t = 0.5. Consistent with the experimental configuration as considered by the authors in their study (Stokes et al., 2001), we consider only the Rankine vortex with an angular velocity of 13.04 rad s^{-1} at the inlet. Important to mention, the swirl specified at the inlet has two different configurations over the domain as follows: force vortex structure up to transition radius and free vortex regime afterwards. Depicted variations in Fig. 3.2(c) vouch for a closer as well as consistent match between the experimental and full-scale simulated results without considering the axis-symmetric and fully developed flow.

Our analytical framework, developed for solving the swirl momentum transport, successfully predicts the swirl velocity profile reported by Yao and Fang, (2012) for the specified Reynolds numbers. Notably, our analytical solutions exhibit a close correspondence with full-scale three-dimensional simulated results. This benchmarking effort reinforces the accuracy of our modelling framework, thereby affirming the credibility of the analytical solutions. As endorsed by the benchmarking analyses outlined above, we adopt the analytically derived velocity profile to compute the concentration field in the fluidic pathway, primarily for the purpose of optimizing computational efficiency.

For the present analysis, we consider the range of Reynolds number, Re ~ 1-10^2 and the power-law index, n ~ 0.6-1.4 (Matsunaga and Nishino, 2014; Cortes-Quiroz et al., 2017; Majhi et al., 2023). It may be mentioned here that to analyse the mixing performance in this endeavour, we vary the transition radius ratio from 0.7 to 0.9 by keeping the Peclet number, $\mathrm{Pe}(=2600)$ constant (Rezk et al., 2012).

3.2.3 Results and Discussion: Description of flow field

Researchers have established that vortex generation induces a chaotic interplay between fluid layers, promoting the efficient mixing of two fluids or solutes within a shorter length. This study focuses on comprehending vortex-assisted mixing of non-Newtonian fluids in a confined fluidic channel, employing a developed mathematical model. Our modelling framework combines a semi-analytical approach for solving the momentum transport equation with a finite volume-based numerical method for the species transport equation, as detailed in section 3.2.1. In this analysis, our emphasis lies on examining the rate of change of Rankine vortex strength and its impact on the mixing of two constituent non-Newtonian fluids. The investigation spans a range of pertinent parameters, including Reynolds number (Re), power-law index (n), and transition radius (r_t). Throughout this study, we maintain a constant inlet swirl number of one to prevent any biased assertions regarding the dominance of angular momentum versus axial momentum in this domain.

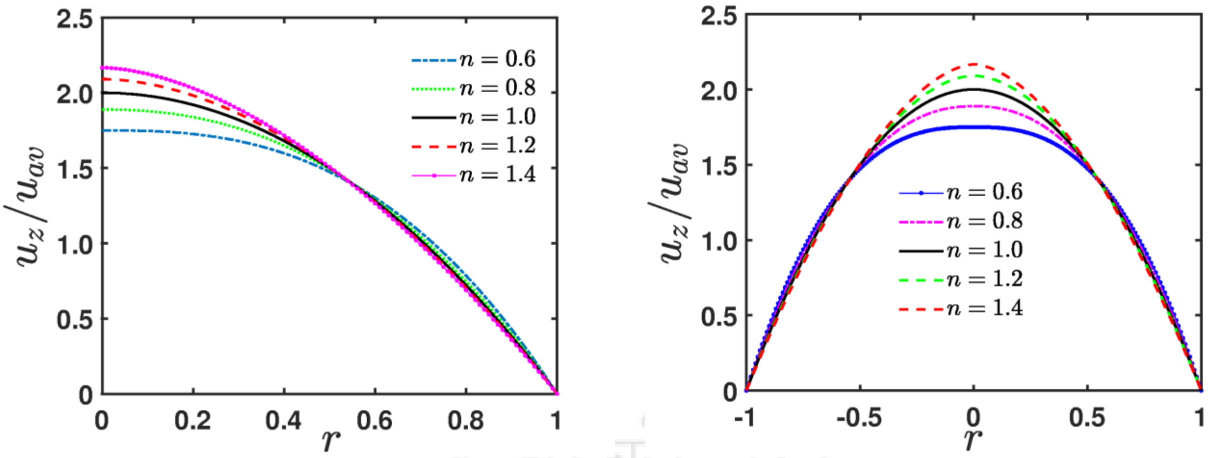

(a) (b)

Figure 3.3: Axial velocity distribution for different value of power-law index in (a) half circle and (b) complete circle.

The final analytical expression presented in Eq. (3.5) reveals that the axial velocity profile is dependent on both rheological properties and radial position. Studying the velocity profile of a Newtonian fluid with a power-law index, *n* = 1, as depicted in Fig. 3.3, it simplifies to a parabolic/Poiseuille profile. In line with the traditional Hagen-Poiseuille flow of a power-law fluid, it is observed that the centerline value of the fully developed axial velocity profile undergoes variations based on the power-law index. As the power law index of the flow decreases, the distinctive top-hat shape of the velocity profile becomes more pronounced for shear-thinning fluids (*n* < 1). Conversely, for shear-thickening fluids (*n* > 1), the velocity profile takes on a sharp-pointed characteristic at the channel centreline, a trend that intensifies with an increase in the fluid's power law index. This divergence from the parabolic shape is a consequence of variations in the viscosity of non-Newtonian fluids across different shear rate zones within the flow. According to Fig. 3.3, it becomes evident that as the power law index approaches Newtonian behavior (*n* = 1), the velocity profiles tend to exhibit a more parabolic shape. The outcomes of this study underscore the significance of laminar flow conditions in a channel, offering a means to calculate a fluid's rheological characteristics and ascertain its velocity distribution.

The influence of swirl velocity becomes apparent in the development of axial flow velocity, with the fully formed state of the flow velocity requiring a longer channel length to be achieved. We initiate our exploration with a description of the swirl velocity profile, as illustrated in Figs. 3.2(a)-(b). Observing Figs. 3.2(a)-(b), it becomes evident that the swirl velocity profile experiences a decrease in the outer region along the outward radial direction after reaching its maximum value.

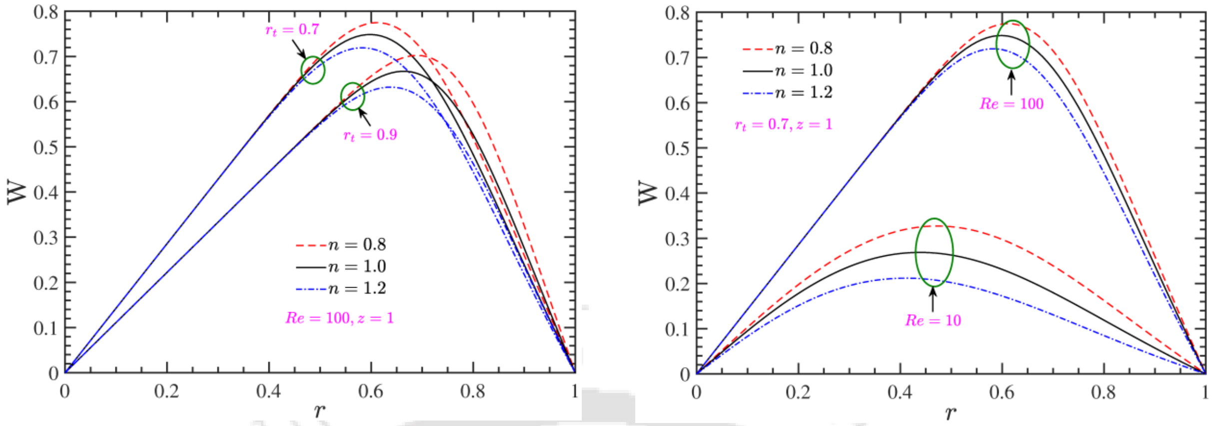

(a) (b)

Figure 3.4: Swirl velocity distribution for different value of power-law index, n = (0.8, 1.0, 1.2); (a) by changing the transition radius from r_t = 0.7 to 0.9 at Re = 100, z = 1 and (b) by changing the Reynolds number from Re = 10 to 100 at transition radius, r_t = 0.7, z = 1.

In the subsequent discussion, which delves into the impact of fluid rheology on swirl velocity profiles, our findings reveal that analytical swirl velocity profiles share characteristics with experimental velocity profiles documented by Kreith and Sonju, (1965), as well as (Bali, (1998) shown in Fig. 3.4 is the variation of the swirl velocity profile in the radial direction of the channel, with changes in the power law index (n) at a specific axial location, where z = 1. The peak magnitude of swirl velocity experiences a more pronounced decrease for fluids with increasing n, attributed to the heightened viscous effect resulting from a larger effective viscosity. In the case of shear-thickening fluids with larger n, the augmented effective viscosity facilitates the transmission of zero momentum from the wall deeper into the pipe, as evident from the radial inward movement of the point of peak velocity. For fluids with higher n, depicted in Fig. 3.4, there is an extended duration for viscous forces to impede the swirl velocity, further contributing to the reduction in the peak magnitude.

Figure 3.4(a) illustrates how the swirl velocity profile deviates significantly for larger values of r_t with change in power-law index close to the inlet of the channel (z = 1). Notably, for a given swirl velocity at the channel's inlet, a shear-thickening fluid (n > 1) exhibits a more pronounced decay of swirl near the inlet compared to a shear-thinning fluid (n < 1). This phenomenon is directly linked to the substantial increase in the effective viscosity of shear-thickening fluids when velocity gradients are significant. We select shear-thinning fluids with n = 0.8, shear-thickening fluids with n = 1.2, and a

Newtonian fluid with n = 1 to investigate the influence of the power-law index on swirl velocity profiles. For blood flow analysis, a commonly used power-law index is applied, specifically n = 0.63 (Mandal et al., 2007). Moreover, the Rankine vortex observed at the inlet serves as a distinctive boundary between the forced and free vortex regions. This is discernible through the radial pressure gradient experienced from the vortex core to the annulus. The transition point, denoted by $r = r_t$, is contingent upon both the swirl velocity and the microtube radius. The shift from the core to the annular region is characterized by variations in the radial pressure gradient, and this transition is pivotal. The swirl velocity profiles for distinct inlet transition radii (r_t = 0.7, 0.9) under the conditions Re = 100 and z = 1 are depicted in Fig. 3.4(a). Building upon the earlier discourse regarding the core ($r < r_t$) and annulus region ($r > r_t$), it is noteworthy that the resultant pressure gradient is attributed to the solid body rotation of the fluid and the influence of wall effects due to shear. While irrotational flow characterizes a perfect free vortex, the fully formed flow boundary condition indirectly introduces shear effects in the free vortex flow field. The boundary layer ensures a velocity gradient in the flow field, with shear effects being prominent close to the wall and gradually diminishing radially towards the axis of the pipe, affecting the free vortex flow. Despite a smooth transition from a forced to a free vortex, it is observed that closer to the inlet, the peak swirl velocity consistently occurs at radii less than the transition radius. This phenomenon is attributed to the frictional impact of the wall on the free vortex region. The magnitude of the swirl velocity increases as the transition radius decreases, maintaining momentum in the radial direction for the fixed value of Re.

Additionally, Fig. 3.4(b) reveals that increasing the Re value, shifts the peak of swirl velocity away from the pipe's axis and alters the transition from a forced to a free vortex, moving it further from the axis. With higher Re values, the competition between the forced core region vortex and the free vortex leads to the peak approaching the wall, influenced by the no-slip boundary condition at the wall, which retards the swirl momentum. As we traverse from a shear-thinning to a shear-thickening fluid, as previously discussed, Fig. 3.4(b) illustrates a significant decrease in swirl velocity magnitude for the same Re value. The Reynolds number, based on the average axial velocity, is a crucial parameter in understanding such flows. In this investigation, the axial flow of the fluid through the pipe is characterized by the Reynolds number. A higher Re implies a faster movement of the fluid through the pipe before the swirl decays.

Consequently, the magnitude of swirl velocity increases from Re = 10 to 100 with a decrease in the power-law index at $r_t = 0.7$ and an axial location z = 1, as depicted in Fig. 3.4(b). Notably, in dilatant fluids, the swirl velocity magnitude is lower than in pseudoplastic fluids, leading to quicker decay of swirl in the former. The interaction between swirl advective effects and viscous effects keeps the highest swirl magnitude close to its radial location. As a result, the influences of the pipe wall on viscosity cause the swirl velocity to closely follow the pipe axis.

As discussed earlier, it becomes evident that fluids characterized by higher *n* values (as depicted in Fig. 3.4) require more time for viscous forces to hinder the swirl velocity. The decrease in peak swirl velocity is more pronounced for fluids with higher *n* values, attributed to the heightened viscous effect resulting from a larger effective viscosity, as illustrated in Fig. 3.4(a).

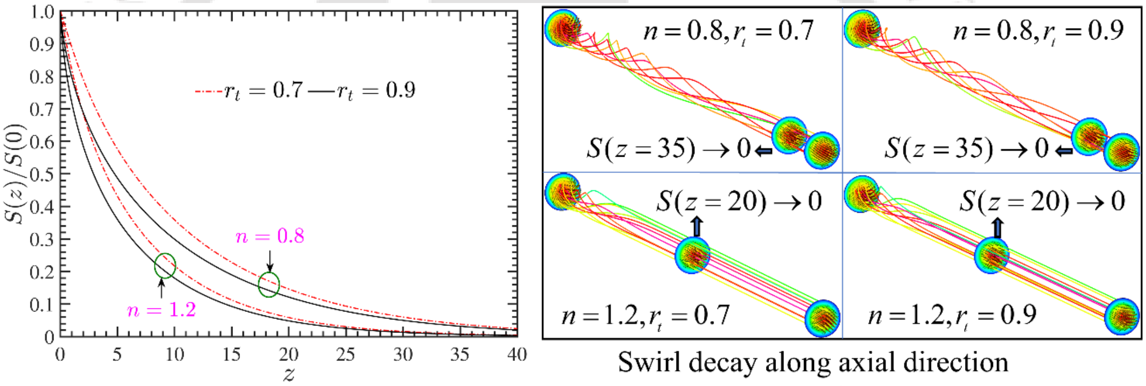

Swirl decay along axial direction

(a) (b)

Figure 3.5: (a) Plots depicting the axial variation of swirl intensity for *n* = 0.8 and 1.2, considering other parameters as $r_t = 0.7$, 0.9 and Re = 100. (b) Qualitative prediction of swirl velocity decay, as shown by the path lines obtained from numerical (ANSYS Fluent) solutions at axial planes (z = 20 and 35) for *n* = 0.8 and 1.2, while the other parameters considered are Re = 100, $r_t = 0.7$ and 0.9.

Figure 3.5 shows the variation of the swirl decay profile with a change in the power-law index (*n*) and transition radius (r_t) along the flow direction. Figure 3.5(a) demonstrates the intensity of swirl decay along the axial direction for both the shear-thinning (*n* = 0.8) and shear thickening, (*n* = 1.2) fluids. The plots are depicted for two different values of transition radii $r_t = 0.7$, 0.9 and obtained at Re = 100. It is apparent from the description made in the preceding section(s) that for a given value of Re, the magnitude of swirl becomes higher and at smaller transition radius. This finding is consistent with the observation we established in our earlier discussion pertaining to the relationship between swirl velocity and Reynolds number. This can be explained by the fact that as the transition radius increases, the swirl velocity gradient increases close to the channel wall. A larger velocity gradient near the channel wall tends to increase the shear stress therein and speed up the swirl velocity's decay. Furthermore, irrespective of the magnitude of Re, the increased viscous effect at higher transition radii tends to speed up the swirl decay for higher values of power-law index. As can be seen from Fig. 3.5(a), the effect of the transition radius is more prominent on the swirl momentum transport of shear-thinning fluids ($n < 1$) compared to shear-thickening fluids ($n > 1$). Also, Fig. 3.5(a) witnesses that the swirl velocity decay is somewhat higher for larger transition radii. We attribute this observation to the increased shear stress developed at higher transition radii owing to the larger velocity gradients. It can be inferred from the foregoing discussion as follows: fluids that thin out under shear would have enhanced transport capability at smaller transition radii than fluids that thicken under shear. Shear-thickening (Dilatant) fluids should not be used in applications that demand for an extended swirl effect since this special class of fluids promote swirl to decay more quickly than shear-thinning (pseudoplastic) fluids.

In Fig. 3.5(b), we show a qualitative description of swirl transport and its decay for different fluids to facilitate a better understanding of the results at hand. The other parameters considered for this plotting are Re = 100, $r_t = 0.7$ and 0.9. The Streamlines emerging from the channel entry are portrayed in Fig. 3.5(b) to provide greater insights into the swirl decay. Note that the plots depicted are obtained from simulations. Figure 3.5(b) witnesses that swirl decay occurs nearly at an axial location $z = 35$ and 20 for shear thinning fluids ($n = 0.8$) and shear thickening fluids ($n = 1.2$) respectively, from the inlet of the chosen fluidic configuration. We would like to discuss two important aspects as observed from Fig. 3.5(b). first, for the shear-thinning fluids ($n = 0.8$), the swirl momentum penetrates a more distance along the channel length for a given strength of inlet swirl, Re (=100) and transition radius, r_t. This observation on complying with our earlier explanation signifies the impact of rheology modulated fluid viscosity on the swirl transport. Second, inlet swirl induces azimuthal motion within the fluid layers, enhancing the contact area and chaotic interaction between the participating fluids. This enhancement in convective-based mixing is particularly significant irrespective of the fluid rheology, emphasizing the enduring impact of inlet swirl in promoting efficient mixing within the system. This qualitative representation of swirl transport in Fig. 3.5(b), derived from full-scale simulations, harmonizes closely with the quantitative analysis of swirl decay presented in Fig. 3.5(b). The coherence observed between our analytical solutions and full-scale simulated results once more underlines the credibility of the analytical technique proposed in this analysis.

3.3 Species Transport: Description of Concentration Field

Consistent with the assumptions considered in this analysis, except for the axisymmetric one (as the constituent two fluids occupy either half of the pipe inlet cross-section), the simplified species transport equation for zero radial flow velocity can be written in the form as given below.

$$u_\theta \frac{1}{r}\frac{\partial C^*}{\partial \theta} + u_z \frac{\partial C^*}{\partial z} = D_0 \left[\frac{1}{r}\frac{\partial}{\partial r}\left(r\frac{\partial C^*}{\partial r}\right) + \frac{1}{r^2}\frac{\partial^2 C^*}{\partial \theta^2} + \frac{\partial^2 C^*}{\partial z^2}\right] \tag{3.14}$$

Here, C^* is solute concentration and D_0 is the diffusion coefficient of non-Newtonian fluids. To distinguish the species concentration of constituent fluids/solutes in the flow domain, we assign $C^* = 1$ for stream A (red colour) and $C^* = 0$ for stream B (blue colour), as shown in Fig. 3.1.

To non-dimensionalize Eq. (3.14), we employ velocity and length scales that previously defined in Section 3.2.1. Simultaneously, we introduce the dimensionless concentration, denoted as $C = C^*/C_0$, where C_0 represents the initial concentration of stream A. It is noteworthy that, based on considerations commonly adopted in this field by researchers (Matsunaga and Nishino, 2014; Cortes-Quiroz et al., 2017; Majhi et al., 2023), we have chosen the specified initial species concentration of the candidate fluids. To provide a comprehensive overview of our ongoing discussion, we highlight a few of these factors, including maintaining the desired level of homogeneity or stratification in a laminar flow regime, controlling swirl intensity and direction for fluids with comparable effective viscosities, and ensuring a sufficiently reduced time for achieving the desired level of convective-based efficient mixing, as outlined by previous studies (Matsunaga and Nishino, 2014; Cortes-Quiroz et al., 2017; Majhi et al., 2023). The non-dimensionalized form of the species transport equation is expressed as follows:

$$\frac{W}{r}\frac{\partial C}{\partial \theta} + U\frac{\partial C}{\partial z} = \frac{1}{Pe}\left[\frac{1}{r}\frac{\partial}{\partial r}\left(r\frac{\partial C}{\partial r}\right) + \frac{1}{r^2}\frac{\partial^2 C}{\partial \theta^2} + \frac{\partial^2 C}{\partial z^2}\right] \tag{3.15}$$

In Eq. (3.15), the Peclet number Pe$(= u_{av}R/D_0)$ is defined as the ratio of convection strength to diffusion strength.

To obtain the mixing performance of the constituent fluids in the chosen fluidic device under the modulation of vortical flows, we solve Eq. (3.15) using our in-house developed finite volume-based code (Patankar, 1980) in parallel mode. For the simulations, we used workstation having the specifications as follows: 8 cores with 16 logical processor, ram 32 GB and base speed 3.41 GHz. The analytically derived flow velocity profiles (both tangential and axial velocities) are used to solve the species transport Eq. (3.15). The non-dimensional boundary conditions for the species transport Eq. (3.15) are outlined next in Eq. (3.16a-c).

Along the radial direction: $\left.\frac{\partial C}{\partial r}\right|_{r=0} = 0\ ;\ \left.\frac{\partial C}{\partial r}\right|_{r=1} = 0$ (3.16 a)

Along the azimuthal direction: $C_{(\theta=0)} = C_{(\theta=2\pi)}\ ;\left.\frac{\partial C}{\partial \theta}\right|_{\theta=0} = \left.\frac{\partial C}{\partial \theta}\right|_{\theta=2\pi}$ (3.16 b)

Along the axial direction: $C_{(z=0)} = \begin{cases} 1, 0 < \theta < \pi \\ 0, \pi < \theta < 2\pi \end{cases}\ ;\ \left.\frac{\partial C}{\partial z}\right|_{z=L} = 0$ (3.16 c)

We briefly discuss the numerical framework employed in this study for solving Eq. (3.15) using the aforementioned boundary conditions (3.16a-c) in the forthcoming section.

3.3.1 Numerical Analysis

As previously indicated, we numerically solve the species transport Eq. (3.15) using our in-house developed finite volume code. For the discretization of Eq. (3.15), we employ the power-law scheme (Patankar, 1980; Patankar, 1981), aiming to achieve converged solutions, particularly for elevated values of the Peclet number (Pe). The boundary conditions specified in (3.16a-c) are applied in the simulation process.

The mixing performance is typically assessed by analysing the variation of mixing efficiency with respect to the mixing methods (active or passive) and by varying the involved parameters such as Peclet number, characteristic length scale of the device etc., within their permissible range. In the present endeavour, to elucidate the mixing performance, we calculate mixing efficiency η_m by using the below given expression (Wang et al., 2015; Gaikwad et al., 2020; Shyam et al., 2021; Kaushik et al., 2022).

$$\eta_m(z) = \left[1 - \left(\int_A |C_i(r,\theta,z) - C_\infty|\, dr d\theta \Big/ \left(\int_A |C_0(r,\theta) - C_\infty| dr d\theta\right)\right)\right] \times 100\% \quad (3.17)$$

In Eq. (3.17), C_∞ represents the dimensionless concentration of species at a perfectly mixed state, which is usually taken as 0.5.

As evident from Eq. (3.17), η_m gives efficiency at each axial location of the channel. Therefore, we can estimate the mixing length from this expression, which in turn, will allow us to predict the required size of the proposed mixing assay. We mention here that at the channel inlet, C_0 = 1, 0 in the upper half and lower half parts respectively, as shown in Fig. 3.1. Note that $\eta_m \in (0,1)$ in (3.17) can take any values between zero and one. Important to mention here, zero value implies no mixing of the constituent components, while a value of unity indicates a completely mixed state of the participating components.

3.3.2 Grid performance analysis

Just to ascertain that the mixing efficiency, estimated numerically in the present analysis, do not have any grid resolution bias, we perform grid performance test for a set of other parameters as n = 0.8 at Pe = 2600, r_t = 0.9, and Re =100 as shown in Fig. 3.6. In doing so, we calculate the grid convergence index (GCI) as shown in Fig. 3.6(a).

To conduct this analysis, we considered grid number with a dummy variable Δ, proportional to the dimension of the chosen model, in three mutually perpendicular directions. Here, we vary Δ with spacing ratio of 1.2 in three mutually perpendicular directions having finer grid distributions for $\Delta = 1.2^1$ and $\Delta = 1.2^2$ cases than that of the case $\Delta = 1.2^0$. Note that a typical grid structure corresponding to $\Delta = 1.2^0$ pertaining to the chosen fluidic configuration with an axial distance of 120 times the pipe radius (L = 120R) is shown in Fig. 3.6(c). From the depicted results of grid convergence index (GCI) for two sets of grid refinements in Fig. 3.6(a), we find that $\mathrm{GCI}_{23}/1.2^p\,\mathrm{GCI}_{12} \approx 1$ with an order of convergence $p = 1.129$, where $\mathrm{GCI}_{12} = 4.98\%$ and $\mathrm{GCI}_{23} = 6.12\%$. This calculation of GCI suggests that the solutions indeed lie comfortably within the asymptotic range of convergence, affirming the reliability of the results of this endeavour.

Following this grid convergence index (GCI) plot, we show in Fig. 3.6(b) the axial variation of mixing efficiency for three distinct grid refinements in all directions as considered for GCI analysis. The parameters considered for this plot are n = 0.8, Pe = 2600, r_t = 0.9, and Re =100. Remarkably, with a change in grid refinements from 62.40×10^6 to 107.83×10^6 elements, we observe an insignificant variation in the mixing efficiency with a percentage change below 1% at a specific axial location, z =

100. Based on these observations from Figs. 3.6(a) - (b), we consider $\Delta = 1.2^1$, equivalently 100×260×2400 (= 62.4×10^6) grids for the subsequent analysis as discussed in the upcoming sections.

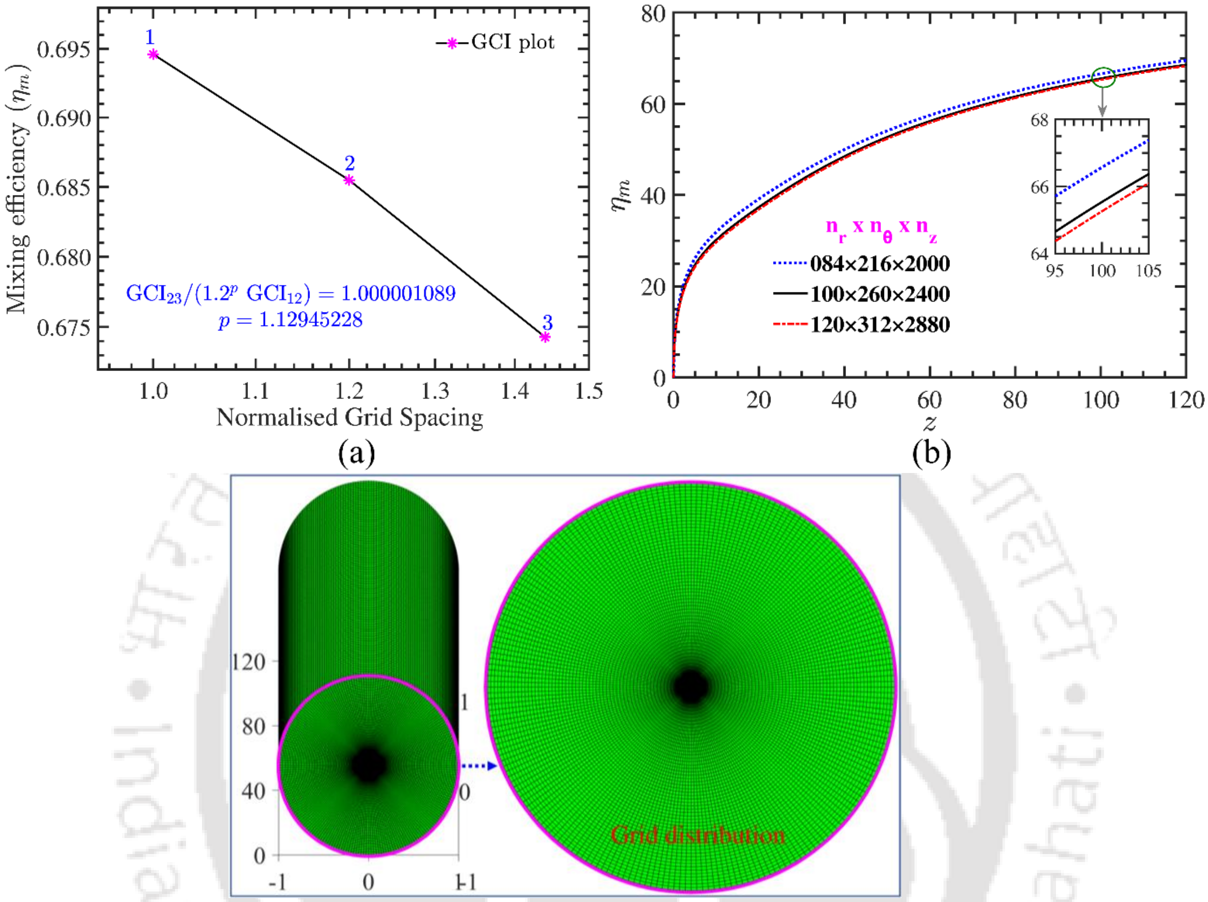

(a)

(b)

(c)

Figure 3.6: (a) Plot showing the grid convergence index (GCI) for three different grid refinements, defined with a dummy variable for $\Delta = 1.2^0, 1.2^1, 1.2^2$. (b) The mixing efficiency at the pipe outlet is plotted for three distinct grid refinements in all directions as considered for GCI analysis. The other parameters considered for these plots (a, b) are Reynolds number (Re = 100), transition radius (r_t = 0.9), Peclet number (Pe = 2600), and power-law index (n = 0.8). (c) Typical grid structure and distribution are shown for the fluidic configuration considered here with an axial distance of 120 times the radius (z = 120R).

3.3.3 Solute Mixing: Prediction, Transition and, Efficiency

From the discussion made above in sub-section 3.2.3, it is apparent that the shear-thinning fluids have a significant influence on the swirl velocity. Also, we understand from the foregoing discussion that for the shear-thinning fluids (n < 1), convection has a dominant influence over molecular diffusion on the underlying mixing for higher values of Re as discussed next.

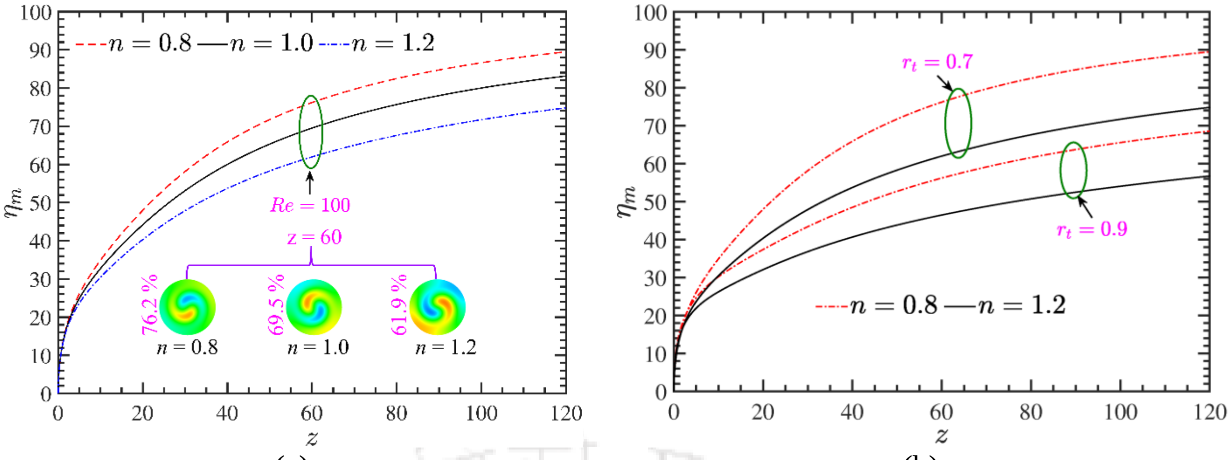

(a) (b)

Figure 3.7: The plot of mixing efficiency along the axial direction; (a) with change in value of power-law index, (*n* = 0.8, 1.0, 1.2). The other parameters considered for the plot are: Reynolds number, Re = 100, Peclet number, Pe = 2600, transition radius, r_t = 0.7; (b) at two different transition radii (r_t = 0.7, 0.9) for shear thinning (*n* = 0.8) and shear thickening fluid (*n* = 1.2). The other parameters considered for the plot are: Reynolds number, Re = 100, Peclet number, Pe = 2600.

The variation of mixing efficiency along the axial direction for different values of power-law index is depicted in Fig. 3.7. The other parameters considered for this plot are Pe = 2600, Re = 100 and $r_t = 0.7$. We can see from Fig. 3.7(a) that with decreasing the value of power-law index, the mixing efficiency increases along the axial direction. It may be mentioned here that for the shear-thinning fluids (*n* < 1), the effect of convection on underling mixing is better realised for a decreasing value of the transition radius and increasing magnitude of Re. The higher strength of rotational inertia for Re = 100 and more shear-thinning behaviour of the participating fluids for *n* = 0.8 leads to an increase of the tangential flow velocity at a given strength of inlet swirl. The higher tangential velocity is responsible for the augmented chaotic nature of the candidate fluids due to increase in the contact area between them, which in turn, promotes convective mixing along the axial direction. It is because of this reason the mixing efficiency of shear-thinning fluids becomes higher as witnessed in Fig. 3.7(a). We show, in Fig. 3.7(b), the influence of transition radii on the axial variation of mixing efficiency. The inference obtained from the depicted variation of swirl velocity profile versus transition radius (see Fig. 3.4(a)) suggests that swirl intensity is higher for smaller transition radius, i.e., r_t = 0.7. As can be seen from Fig. 3.7(b), for the smaller value of r_t, the mixing efficiency at the channel outlet becomes higher, attributed primarily to higher intensity of swirl. Notably, for a given r_t, the mixing efficiency at any axial location becomes higher for the shear-thinning fluids (*n* < 1) compared to the shear-thickening fluids (*n* > 1), as seen in Fig. 3.7(b). For a specified strength of inlet swirl, the rate of swirl decay is slower for shear-thinning fluids (see Fig. 3.5(a)), which in, renders better mixing efficiency for this class of fluids at any axial location.

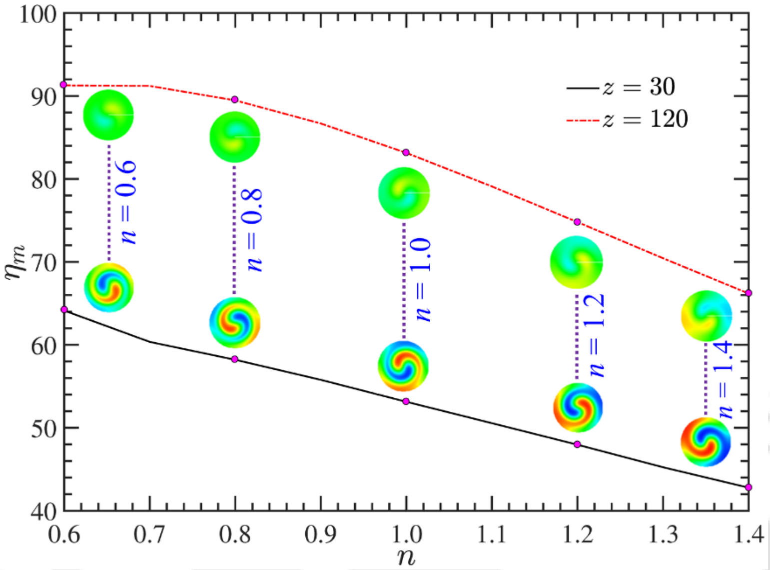

Figure 3.8: The plot shows qualitative aspect of mixing efficiency using concentration contour with change in power-law index (n = 0.6, 0.8, 1.0, 1.2, and 1.4) at two different axial location, z = 30 and 120. The inset concentration contours are used to show the qualitative aspect of advective mixing for shear thinning fluid at n = 0.6 compared to diffusive mixing for shear thickening fluid at n = 1.4. It is based on the complete rotation of fluid at n = 0.6 compared to n = 1.4. The other parameters considered for this analysis are: Reynolds number, Re = 100, Peclet number, Pe = 2600, and, transition radius, r_t = 0.7.

As the prime focus of this endeavour is to investigate the mixing performance of non-Newtonian fluids/solutes, we make an attempt in Fig. 3.8 to plot the variation of mixing efficiency (η_m) with flow behaviour index (n), characterizing the rheological behaviour of the inelastic non-Newtonian fluids considered in this analysis. We may mention here that the mixing transition is a consequence of the appearance and development of small-scale three-dimensional swirl structures in the flow field. The large excursions corresponding to large vortex structures, typically depends on Re, are responsible for convective based mixing in shorter length (Breidenthal, 1981). Precisely by depicting Fig. 3.8, we would like to demonstrate on how the transition in mixing occurs in a swirl-driven flow environment as modulated by the fluid rheology. The other parameters are Re = 100, Pe = 2600 and r_t = 0.7.

The higher internal convection of the constituent fluids, which follows a non-linear trend with increasing n, as demonstrated by the concentration contours in Fig. 3.8, leads to achieve better mixing in the swirl-driven flow environments. It may be mentioned here that the concentration contours give a good indication of the impact of swirl on vortex formation. At an axial location z = 30, the concentration contour for n = 0.6 (inset of Fig. 3.8) exhibits a complete bulk fluid rotation compared to the reference vortex formed for n = 1.4. This observation indicates that convection-based mixing dominates over molecular diffusion for n = 0.6. Depicted contours in Fig. 3.8 suggest that for more shear-thickening behaviour of the candidate fluids (n = 1.4), mixing based on molecular diffusion is clearly visible to the naked eye at an axial location z = 30 compared to z = 120. As can be verified from Fig. 3.8, with increasing the shear-thinning nature of constituent components, the underlying mixing is seen to become more pronounced regardless of the magnitude of Re, transition radius, and Pe. A lesser apparent viscosity of constituent fluids having more shear-thinning nature for a given deformation rate (here: strength of inlet swirl) inhibits faster attenuation of swirl for its given strength, which in turn, ensure better mixing performance at any axial location, as witnessed in Fig. 3.8.

It may be mentioned here that for a given strength of the inlet swirl, its transmission through the participating fluids largely relies on the momentum transport, which in turn, depends on the Reynolds number. Thus, in a swirl driven flow environment, underlying mixing of constituent fluids will be governed by both inevitable molecular diffusion and chaotic advection. Considering this aspect, we plot in Fig. 3.9(a) the variation of mixing efficiency with Re for three different values of n (= 0.8, 1.0, and 1.2). The following parameters are considered for this plot as: Pe = 2600, z = 100 and r_t = 0.7. We discuss two important observations as follows. First, the mixing efficiency is seen to be higher for shear-thinning fluids ($n < 1$) compared to shear-thickening fluids ($n > 1$). We attribute this observation to the lesser apparent viscosity of shear-thinning fluids, which prevents faster swirl decay. Second, higher inertial effect for higher Reynolds number accelerates the swirl motion to penetrate much deeper into the channel before attenuation. However, at lower Re, impeding viscous resistance leads to swirl decay over shorter distances from the inlet. This observation is justifiable qualitatively from the mixing concentration contours depicted in Fig. 3.9(b). It is because of the diminishing effect of inlet swirl at low Re, we observe a linear trend of mixing in regime-I of Fig. 3.9(a), attributed primarily to the diffusion-based mixing. The contours depicted in Fig. 3.9(b) suggest that for the smaller values of Re (= 1, 10), the effect of inlet swirl does not get translated into the downstream locations of the fluidic configuration. This observation is attributed to the weaker rotational fluid motion developed at the pipe inlet for smaller values of Re. It is because of this reason, we obtain diffusion-based mixing for smaller Re even at a further downstream location of the pipe as witnessed in Fig. 3.9. The role of convention-based mixing is shown in regime-II, which follows the non-linear trend. For Re greater than 10, bulk fluids rotate more than 90°. This flow structure helps to increase the contact surface area between the fluid layers and enhances convection-based mixing as supported by the contours shown in Fig. 3.9(b).

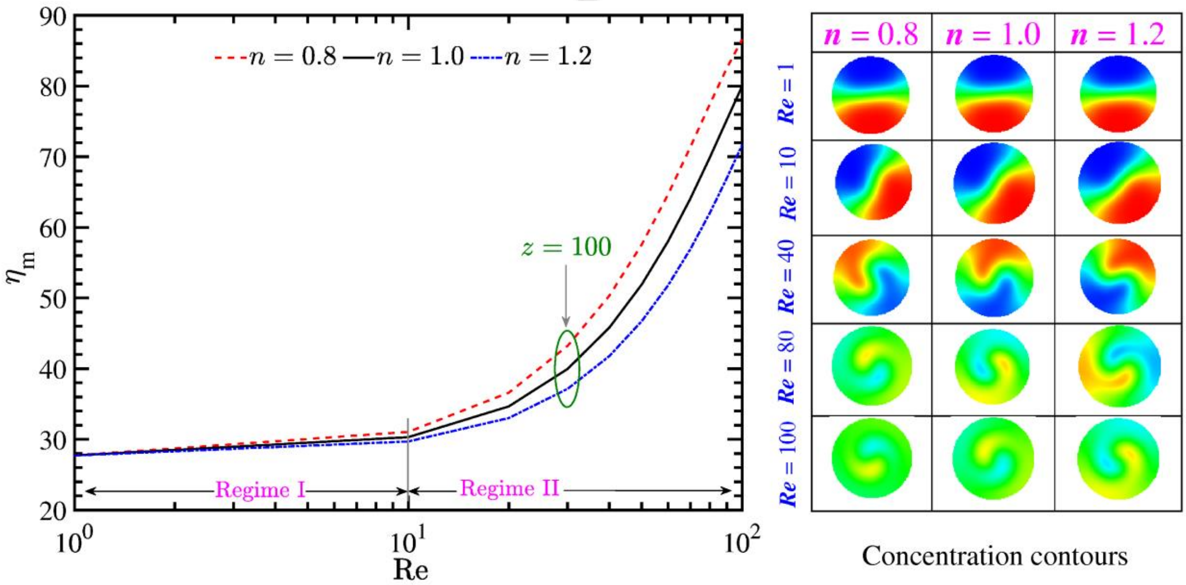

(a) (b)

Figure 3.9: (a) The plot shows mixing efficiency (left side) as a function of Reynolds number (1 to 100), as well as shear thinning and thickening (n = 0.8 and 1.2, respectively), in addition to Newtonian fluid (n = 1.0) at an axial location, z = 100. (b) The qualitative aspect of mixing efficiency (right side) using concentration contours with change in same n at Reynolds number, Re = 1, 10, 40, 80, and 100 is shown. Increasing the Reynolds number, advective mixing (Regime II) is obtained at Re = 100 compared to diffusive (Regime I) at Re = 1 and 10 based on complete rotation of fluid compared to only twist, respectively. The other parameters considered for this analysis are: Peclet number, Pe = 2600 and transition radius, r_t = 0.7.

The contours illustrating the mixing efficiency in Figs. 3.8 and 3.9 establishes the dependency of underlying mixing on the power-law index ($n \in 0.6 - 1.4$) and Reynolds number ($\mathrm{Re} \in 10^0 - 10^2$). The discussion made above in the context of Figs. 3.8 and 3.9 underscores that convection dominated mixing becomes prominent for shear-thinning fluids with higher Re. To substantiate this observation, we next take an effort to establish a correlation among the mixing efficiency (η_m), power-law index (n), and Reynolds number (Re). The developed correlation, represented by a second order polynomial, exhibits a high degree of fit with a coefficient of determination value of 0.9935. The developed explicit, quadratic form of η_m in terms of the independent variables, i.e., power-law index (n), and Reynolds number (Re) at the pipe outlet (z = 120) can be expressed as follows:

$$\eta_m = a_1 + a_2 n + a_3 \mathrm{Re} - a_4 n^2 - a_5 n \mathrm{Re} + a_6 \mathrm{Re}^2 \tag{3.18}$$

Here, the constants a_1, a_2, a_3, a_4, a_5 and a_6 are 23.31, 15.92, 0.8756, 10.9, 0.3503 and 0.0002416, respectively. Note that the proposed correlation in Eq. (3.18) corresponds to the date set obtained for transition radius $r_t = 0.7$ and Pe $= 2600$.

On using Eq. (3.18), we obtain the following insights as discussed next. The mixing efficiency at the channel outlet (z = 120) becomes higher with increasing the magnitude of Re and for an enhanced shear-thinning nature of the fluid. This inference effectively supports the findings depicted in Figs. 3.8 and 3.9. Hence, it becomes evident that convective-based mixing efficiency is significantly influenced by both the rheology of the constituent fluids and the flow Reynolds number.

3.4 Summary

In this analysis, we explore the impact of swirl flow, characterized by vorticial motion, on the mixing of non-Newtonian fluids within a narrow cylindrical channel under laminar flow conditions. The analytical derivation of the swirl velocity profile involves superimposing fully developed flow and applying the Rankine vortex condition at the channel inlet. Incorporating these analytically obtained flow velocities into the species transport equation allows us to model the concentration distribution of constituent fluids/solutes across the chosen fluidic configuration. Our investigation delves into the influence of inlet swirl by varying key parameters, including the flow behavior index (power-law index, n = 0.6-1.4), Reynolds number (Re = 10^0-10^2), and transition radius (r_t = 0.7-0.9). Results indicate that an increase in the power-law index, signifying a shift in the behaviour of the constituent fluids from shear-thinning to shear-thickening, leads to an apparent viscosity increase for a given inlet swirl. We observe that understanding the decay of swirl is closely tied to the power-law index, highlighting its critical role in this context. Both the power-law index and Reynolds number significantly impact the length of swirl decay. The heightened apparent viscosity of fluids with higher power-law index values results in reduced axial and tangential velocities. Subsequently, decreasing the transition radius and increasing the Reynolds number enhance swirl intensity, influenced by a higher radial pressure gradient and reduced wall shear stress. Our simulations reveal how swirl alters flow structure, inducing rotation and expanding the contact surface area of participating fluids. Importantly, chaotic convection driven by swirl plays a substantial role in boosting mixing efficiency, particularly at higher Reynolds numbers. The study explores the influence of Reynolds and power-law index (= 0.8, 1.0 ,1.2), demonstrating that at lower Reynolds numbers ($Re \leq 10$), molecular diffusion dominates mixing, while chaotic convection becomes significant at higher Reynolds numbers ($Re > 10$). Also, through our simulations, we reveal how swirl modifies the flow structure, inducing rotation and increasing the contact surface area of the participating fluids. Our study highlights the significant role of chaotic convection, driven by swirl, in enhancing mixing efficiency at higher Reynolds numbers with increase in the shear thinning nature of fluid Insights gained may benefit researchers aiming to enhance convective mixing using swirl flow, especially by altering rheological properties of base fluids. We believe that the insights garnered from this study contribute to the foundational understanding of vortex-assisted mixing for non-Newtonian fluids within a narrow fluidic confinement.

Chapter 4

Effective solute mixing of non-Newtonian fluid through the modulation of electroosmotic vortices using a soft polyelectrolyte layer

We investigate the flow of non-Newtonian Carreau fluids through a small conduit with patterned PEL-PL (Ployelectrolyte layer-Polymeric layer) patch on the inner walls. The fluid movement is induced by both an applied pressure gradient and an electric field, leading to vortex formation at the PEL-fluid interface. Our study reveals that the rheological properties of the involved components significantly impact the recirculation velocity (vortex strength), influencing mixing efficiency. Additionally, we analyze the characteristic time of aggregation kinetics in the binary system, illustrating how it is influenced by rheological and PEL geometrical parameters. This has significant implications, especially in the context of non-Newtonian biofluids containing biomolecules such as DNAs, proteins, and blood plasma.

4.1 Mathematical Formulation

The physical domain of the micromixer, as schematically depicted in Fig. 4.1, is having built-in patterned polyelectrolyte layer (PEL) and polymeric layer (PL) soft patched at the inner wall surfaces. The considered length and height of the micromixer are L and $2H$, length, while the length and width of the PEL patch are L_P^* and d_p^*, respectively. It is also noted that the space between two consecutive PEL is filled with uncharged PL of thickness d_p^*. Also, as can be seen from Fig. 4.1, the PL is grafted in both upstream and downstream portions of the top and bottom channel walls. Moreover, the arrangement of patterned PEL-PL patch grafted on the top and bottom walls is considered to be symmetric. We have imposed the external electric potential difference, ΔV at the micromixer ends to generate the electroosmotic vortices, while an applied pressure gradient drives the bulk flow. The tractor species (specifically dye), which would mix with pure non-Newtonian liquid (Liquid-1), is referred to as liquid-2 having diluted concentration (c_0^*). Liquid-2 is introduced at the lower-half of the inlet in order to quantify the mixing quality. Therefore, the normalised dilute tracer species concentration (C = c^*/c_0^*) should be 1 at the bottom-half of the inlet (in liquid-2) and zero (= 0) at the top-half of the inlet (in liquid-1) (Azimi et al., 2017; Banerjee et al., 2019).

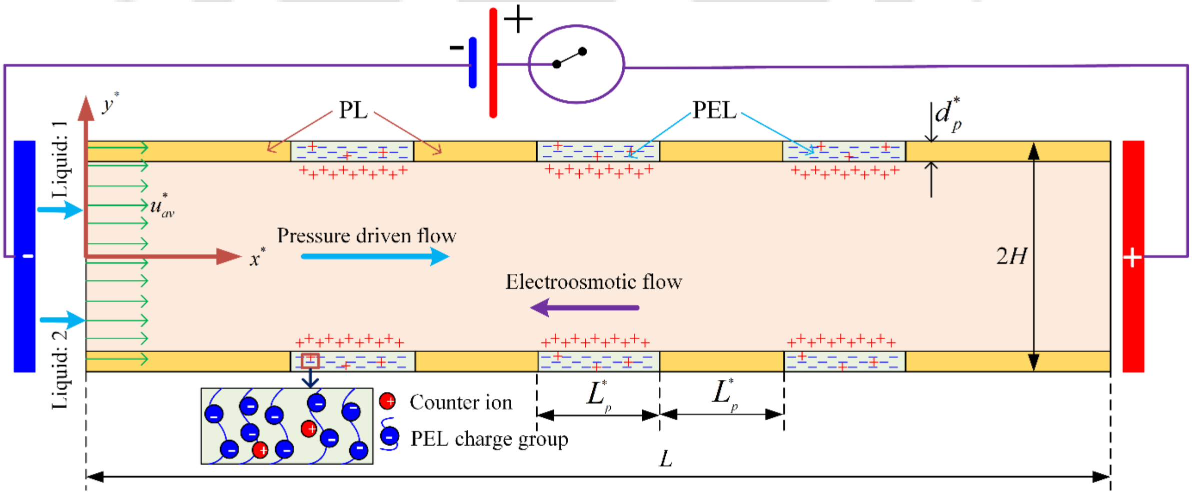

Figure 4.1: Schematic diagram of physical domain depicting polyelectrolyte layer (PEL), polymeric layer (PL), and dimensions of the micromixer. Here, liquid 1 is pure, and liquid 2 is a mixture of the same base fluid and electrically neutral tracer particles.

For the modeling framework developed here, we have taken the following assumptions as follows: the flow of non-Newtonian fluid is assumed to be steady, two-dimensional, and incompressible; the effect of finite-ionic size is neglected due to smaller bulk ionic concentration (Nayak et al., 2020); the Joule heating effect is neglected as the order of external electric field is taken as 10^4 V/m (Shit et al., 2016). We have also ignored the viscous heating effect. Further, the order of induced electric field in EDL $\left(\psi_{ref}/\lambda_D\right)$ is much higher than the order of external applied electric field. Therefore, we neglected the influence of external electric field on ionic distribution inside the EDL. Now, considering these physically justified assumptions, the corresponding transport equation in their dimensionless form can be written as (Gaikwad et al., 2020; Mehta and Mondal, 2023):

$$\nabla^2\Psi = \kappa^2 \sinh(\Psi) - \Omega\kappa_p^2 \tag{4.1}$$

$$\nabla^2\Phi = 0 \tag{4.2}$$

$$\nabla\cdot\mathbf{u} = 0 \tag{4.3}$$

$$\mathrm{Re}\left(\mathbf{u}\cdot\nabla\right)\mathbf{u} = -\nabla p + \nabla\cdot\boldsymbol{\tau} + \kappa^2\sinh\left(\Psi\right)\nabla\Phi - \Lambda F_d^2\mathbf{u} \tag{4.4}$$

$$\mathrm{Pe}\left(\mathbf{u}\cdot\nabla C\right) = \nabla^2 C \tag{4.5}$$

Here, Eqs. (4.1) to (4.5) represent the Poisson–Boltzmann (PB) equation for EDL potential field $\left(\Psi\right)$, Laplace equation for the external potential field $\left(\Phi\right)$, continuity and momentum equation for fluid flow, and convection-diffusion equation for species concentration field (C) all are in dimensionless form. Dimensionless parameters for the present study are defined as: $\nabla \equiv \left(\partial/\partial x, \partial/\partial y\right)$; $x = x^*/H$, $y = y^*/H$; $\Psi = \Psi^*/\Psi^*_{ref}$, $\Psi^*_{ref} = K_b T/ze$; $\Phi = \Phi^*/\Phi^*_{ref}$, $\Phi^*_{ref} = (\Delta V)H/L$; dimensionless velocity vector, $\mathbf{u} = \mathbf{u}^*/u^*_{HS}$, Helmholtz-Smoluchowski velocity, $u^*_{HS} = \varepsilon_0\varepsilon_r E\Psi^*_{ref}/\mu^*_0$, $E = \Delta V/L$; $p = p^* H/\mu^*_0 u^*_{HS}$; $C = c^*/c^*_0$, here c^*_0 is inlet tracer particle concentration in base liquid; dimensionless Debye-Hückel (DH) parameter of electrolyte, $\kappa = H/\lambda_D$, $\lambda_D = \sqrt{\varepsilon_0\varepsilon_r K_b T/z^2 e^2 n_0}$, here $\varepsilon_0, \varepsilon_r, z, e, n_0, K_b,$ and T represents free space permittivity, electrolyte relative permittivity, valance of mobile ion, the charge of an electron, bulk ionic concentration, Boltzmann constant and absolute temperature, respectively. The DH parameter of the PEL, $\kappa_p^{*2} = zZe^2 N/\varepsilon_0\varepsilon_r K_b T$; dimensionless DH parameter of the PEL $\kappa_p = \kappa_p^*(H)$, here Z and N are the total valences of polyelectrolyte functional group and electrolyte, and total number density of polyelectrolyte ions, respectively. $\Omega = 0$ and 1 for PEL-free region and PEL region, respectively; $\Lambda = 0$ and 1 for PEL/PL-free region and PEL/PL region, respectively. Here, Re and Pe are the Reynolds number and Peclet number which are expressed as; $\rho u_{HS}^* H/\mu_0^*$ and $u_{HS}^* H/D$, respectively, where D is the diffusion coefficient of ionic species. Moreover, F_d is the flow resistance provided by the PEL and PL porous structures, called Darcy's frictional drag.(Gaikwad, Kumar and Mondal, 2020) Further, the dimensionless deviatoric stress tensor (Nayak et al., 2020; Mehta et al., 2021), $\boldsymbol{\tau}$ is written as $\boldsymbol{\tau} = \bar{\eta}(\dot{\boldsymbol{\gamma}})\left(\nabla\mathbf{u} + (\nabla\mathbf{u})^T\right)$, which is non-dimensionlised with the scale $\mu_0^* u_{HS}^*/H$; the dimensionless apparent viscosity according to Carreau model is given as $\bar{\eta}(\dot{\boldsymbol{\gamma}}) = \bar{\mu}_\infty + (1-\bar{\mu}_\infty)\left(1+Cu^2\dot{\boldsymbol{\gamma}}^2\right)^{n-1/2}$; and the dimensionless second invariant of rate of deformation tensor, $\dot{\boldsymbol{\gamma}} = \sqrt{0.5(\mathbf{S}:\mathbf{S})}$, $\mathbf{S}$ is the dimensionless strain rate tensor and expressed as $\left(\nabla\mathbf{u} + (\nabla\mathbf{u})^T\right)$. Further, $\bar{\mu}_\infty$ is the dimensionless infinity shear rate viscosity normalized with the scale zero shear rate viscosity, μ_0^*; Cu is the Carreau number and expressed as $\lambda u_{HS}^*/H$; n is flow-behavior index and λ is the time parameter for Carreau model.

4.1.1 Boundary conditions

We have employed the following physically justified boundary to solve the Eqs. (4.1) to (4.5) numerically: At the inlet: $\mathbf{n}\cdot\nabla\Psi = 0,\ \Phi = 10,\ u_{av} = 0.3,\ C = 0$ for $0 \le y \le 1$ and $C = 1$ for $-1 \le y \le 0$; at the wall: $\mathbf{n}\cdot\nabla\Psi = 0,\ \mathbf{n}\cdot\nabla\Phi = 0,\ \mathbf{u} = 0,\ \mathbf{n}\cdot\nabla C = 0$; at the outlet: $\mathbf{n}\cdot\nabla\Psi = 0,\ \Phi = 0,\ p_g = 0,\ \mathbf{n}\cdot\nabla C = 0$; at the interface of PEL and void region; $\Psi_{PEL} = \Psi_{void}$, $\nabla\Psi_{PEL} = \nabla\Psi_{void}$, $\Phi_{PEL} = \Phi_{void}$, $\nabla\Phi_{PEL} = \nabla\Phi_{void}$, $\mathbf{u}_{PEL} = \mathbf{u}_{void}$, $\boldsymbol{\tau}_{PEL} = \boldsymbol{\tau}_{void}$, $C_{PEL} = C_{void}$. Moreover, the continuity of transport variables, as well as its fluxes, is considered at the interface of PL and void region.

Further, to quantify micromixing, the mixing efficiency is defined and the same at the mixer outlet is calculated as (Gaikwad et al., 2020; Mehta et al., 2021):

$$\eta = 100 \times \left(1 - \left(\int_{y=-1}^{y=1} \left(\left| C - C_{\infty} \right| \right) \Big/ \int_{y=-1}^{y=1} \left(\left| C_0 - C_{\infty} \right| \right) \right) \right) \tag{4.6}$$

Here, C_0 (= 0 or 1) and C_{∞} (= 0.5) represent the initial concentration of fluid at unmixed and mixed states, respectively.

In the present case, we have considered applied pressure gradient to bring the candidate fluids in motion through the mixer, while the applied electric field helps in generating vortices in regions at the grafted PEL and clear fluid interface by virtue of the electroosmotic effect. It may be mentioned here that generated vortices promotes mixing as aptly discussed in the later section of this article. Albeit the generated vortices seem to have favorable impact on the underlying mixing of the candidate fluids, these structures have an adverse impact on the net throughput as well. Therefore, to maintain the constant net throughput, the required pumping power needs to be higher as compared to the case wherein no vortices are formed. In this regard, we have proposed a parameter called 'mixing performance' and defined as the ratio of mixing efficiency to pressure-drop across the micromixer. This term is mathematically represented as:

$$\text{Mixing Performance (MP)} = \eta / \Delta p_{drop} \tag{4.7}$$

Here, Δp_{drop} is the dimensionless pressure-drop between inlet and outlet of the micromixer. It may be added here that a relatively higher value of this parameter will signify the better performance of the proposed mixer.

4.2 Numerical methodology and model benchmarking

The transport equations governing the mixing dynamics [Eqs. (4.1) to (4.5)] are solved using the finite element-based numerical solver COMSOL® Multiphysics, (2015) in serial mode. For the simulations, we used workstation having the specifications as follows: 8 cores with 16 logical processor, ram 32 GB and base speed 3.41 GHz. The computational domain of the micromixer is divided into subdomains using non-uniform triangular mesh elements. The mesh is considered denser at the inlet near to fluid interface section, walls, and near the PEL patch for the accurate prediction of all transport variables. The Galerkin weighting method is used to convert the governing differential equations into integral equations, which are then solved iteratively to reach the specified relative residual value of 10^{-6} for all the transport variables.

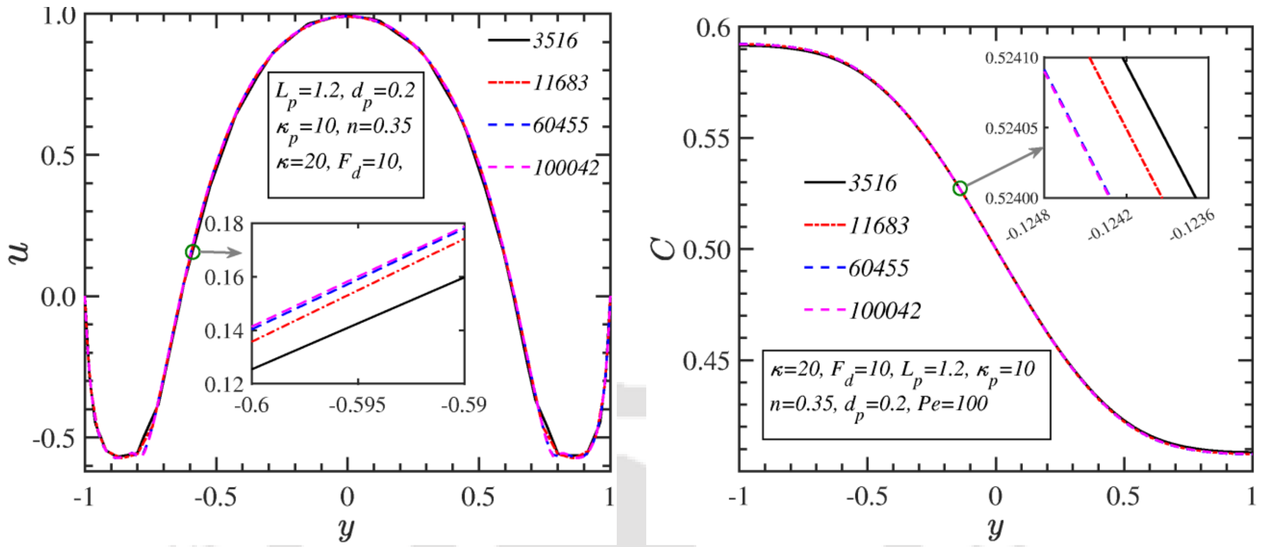

(a) (b)

Figure 4.2: Comparison of (a) dimensionless flow velocity profile at section, x = 5.5, and (b) dimensionless species concentration at the outlet of micromixer by varying the number of elements of mesh when $L_p = 1.2$, $d_p = 0.2$, $u_{av} = 0.3$, $\kappa_p = 10$, $\kappa = 20$, $n = 0.35$, $F_d = 10$, Pe = 100.

Also, to check the accuracy of the present work, we performed the grid independence test in Figs. 4.2(a) and (b) for axial velocity field at section $x = 5.5$ and dimensionless species concentration at the outlet of micromixer, respectively. The parameters considered for the grid independence test are: $L_p = 1.2$, $d_p = 0.2$, $u_{av} = 0.3$, $\kappa_p = 10$, $\kappa = 20$, $n = 0.35$, $F_d = 10$, and Pe = 100. As can be seen from Fig. 4.2, for the increase in mesh elements beyond 60455, profiles are closely overlapping with the case with number of elements 100042, and percentage error is obtained less than 0.3 %. Hence, to save the computational cost, a total number of elements 60455 are considered for simulating all the cases as considered and demonstrated in this analysis.

To check the accurateness of the modeling framework developed in this work, we compare in Fig. 4.3 the results obtained from the present numerical model with the existing numerical and experimental results works. First, we compare the dimensionless species concentration field at the section, x = 5 of the electroosmotic micromixers, obtained from the present model with the numerical results of Gaikwad et al., (2020) as shown in Fig 4.3(a), for the limiting case of n = 1. The other parameters considered for this validation are $u_{av} = 0.1$, $d_p = 0.1$, $\kappa_p = 10$, $\kappa = 15$, $F_d = 10$, and $\mathrm{Pe} = 500$. Also, in

Fig. 4.3(b), the dimensionless species concentration profile of the present study is validated with the experimental results of Biddiss et al., (2004), considering two electric field strengths, 280 V/cm and 70 V/cm for the limiting case of $n = 1$. The other parameters considered for this comparison are as follows: solution molarity = 25 mM, $\bar{\mu}_{\infty} = 0$, $\mu_o^* =$ 0.001 Pa-s, $\rho = 1000$ kgm^{-3}, $D = 4.37 \times 10^{-10}$ m^{2}s^{-1}. Note that for this particular validation, we considered the value of zeta potential in such a way that corresponds to electroosmotic mobility $= -5.9 \times 10^{-8}$ m^2/(V-s).

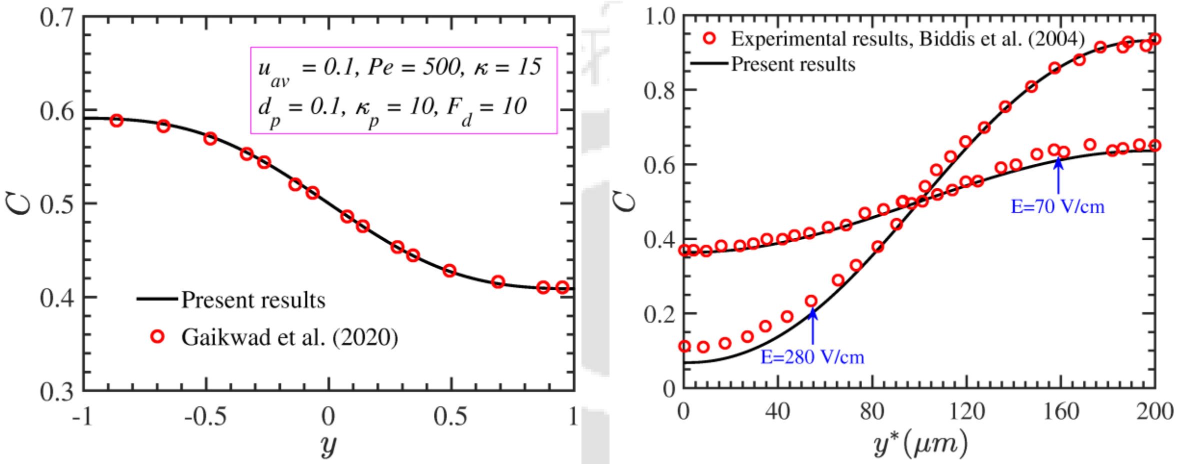

(a) (b)

Figure 4.3: (a) Comparison of dimensionless species concentration at the section $x = 5$ in the electroosmotic micromixer having PEL layer with the numerical work of Gaikwad, et al., (2020) for the limiting case when $n = 1$, $u_{av} = 0.1$, $d_p = 0.1$, $\kappa_p = 10$, $\kappa = 15$, $F_d = 10$ and Pe $= 500$. (b) Comparison of dimensionless species concentration at the outlet of the electroosmotic micromixer with the experimental result of Biddiss et al., (2004) for the limiting case when $n =$ 1, $E = 280$ V m^{-1} and 70 V m^{-1}, $\bar{\mu}_{\infty} = 0$, $\mu_o^* = 0.001$ Pa-s, $\rho = 1000$ kg/m^3, $D =$ 4.37×10^{-10} m^2 s^{-1}.

4.3 Range of present model parameters

In the present study, we have considered micromixer height $(2H)$, while values of the other parameters considered are as follows: external electric field (E) and reference EDL potential (Ψ_{ref}^*) as 10 μm, 10000 V m^{-1}, and 25 mV, respectively (Haque et al., 2021; Mehta et al., 2022). The range of dimensionless PEL patch thickness $(d_p = d_p^*/H)$ and length $(L_p = L_p^*/H)$ is taken as: $0.02 \le d_p \le 0.2$ and $0.8 \le L_p \le 1.6$, respectively (Gaikwad et al., 2020; Mehta and Mondal, 2023). It is worth mentioning here that, as evident from experimental studies, the thickness of PEL varies from 100 nm to 1000 nm (Biesalski and Rühe, 1999; Biesalski and Rühe, 2000). Therefore, the aforementioned range of d_p (dimensionless thickness), as considered for the present investigation, is physically justifiable from the perspective of fabrication of micromixer. The dimensionless value of DH parameter (κ) is taken as 20 and this value corresponds to electrolyte ionic concentration typically considered in real applications. Moreover, conforming to the physically permissible range of fixed charge in PEL, the range of DH parameter for PEL patch (κ_p) is taken as $5 \le \kappa_p \le 20$ (Li et al., 2017; Patel et al., 2020; Sadeghi et al., 2020). It may be added here that the Carreau model time parameter (λ), for the range hematocrit levels of 5 to 15%, is almost constant for the separated plasma (i.e., 95% water) and RBC mixture of blood, as well as for the pure blood sample with a hematocrit level of 45%. Considering this aspect, the value λ for the present analysis is taken as 3.313 s (Mehri et al., 2018). To mimic the shear-thinning nature of the fluid, the range of the flow-behavior index (n) considered here is 0.35 to 0.75 (Cho and Kensey, 1991; Zhao and Yang, 2011; Mehri et al., 2018). A fixed value of $\mu_\infty^* / \mu_0^* = 0.0616$ is considered for the present study (Johnston et al., 2004; Mehri et al., 2018). Further, the typical range of μ_0^* varies from 23.33 to 139.3 mPa-s for hematocrit levels of 5 to 15% of blood. Hence, the order of Helmholtz– Smoluchowski velocity (u_{HS}^*) is obtained as $10^{-6} \sim 10^{-5}$ m-s^{-1} for $\varepsilon_r = 80$ and aforementioned values of H, Ψ_{ref}^* and E. Based on the obtained range of u_{HS}^* and aforementioned value of λ, the range of Carreau number is obtained as $0 \le Cu \le 5$ (Shahsavari and McKinley, 2015; Mehta and Mondal, 2023). The range of diffusion coefficient considered for the present analysis is $10^{-11} \sim 10^{-12}$ m^{2}s^{-1} and this chosen range is typical to solutes/species used for biomedical applications (Mehta et al., 2021; Mehta and Mondal, 2023). The range of diffusive Peclet number based on the aforementioned values of u_{HS}^* and H is taken as $1 \le \mathrm{Pe} \le 100$ (Gaikwad et al., 2020; Haque et al., 2021; Mehta et al., 2021; Vasista et al., 2022; Mehta and Mondal, 2023).

4.4 Results and discussion

In this work, we primarily focus on the mixing of the constituent components and for this part, we look into the flow field and flow structure developed in the chosen fluidic system. To this end, we take an effort to describe the variation of dimensionless recirculation velocity (u_r), dimensionless species concentration (C), mixing efficiency (η), mixing performance $(\eta/\Delta p_{drop})$, and characteristic time for shear-induced binary aggregation kinetics (t_c) by varying the flow-behavior index (n), Carreau number (Cu), diffusive Peclet number (Pe) dimensionless PEL thickness (d_p), dimensionless patch length (L_p), drag coefficients (F_d), and the PEL Debye-Hückel parameter (κ_p) in the aforementioned physically justified ranges.

4.4.1 Description of flow field

For the problem considered in this analysis, the species transport is dominated by the convection as diffusive Peclet number is greater than unity. Pertaining to the convection-dominated species transport phenomenon, vortex formation is important fluidic functionality essentially to obtain an effective solute mixing (Mehta et al., 2021; Mehta and Mondal, 2023). It is intuitive to expect that the fluid rheology would modulate the size and strength of vortex which in turn, will control the mixing efficiency. This aspect has triggered us to take an effort to delve deep into the underlying physics behind the charged PEL-induced vortex generation phenomenon under the influence of fluid rheology. In doing so, we first look at the description of the flow field as discussed next. The contours of dimensionless flow velocity and streamlines (left side) and dimensionless stream function (right side) are depicted in Fig. 4.4 by varying the Carreau number $(Cu = 0.1,\ 1,\ 5)$. It is observed from Fig. 4.4 that the vortex is formed near the PEL patch due to the interaction of pressure-drive flow (forwards flow), which occurs

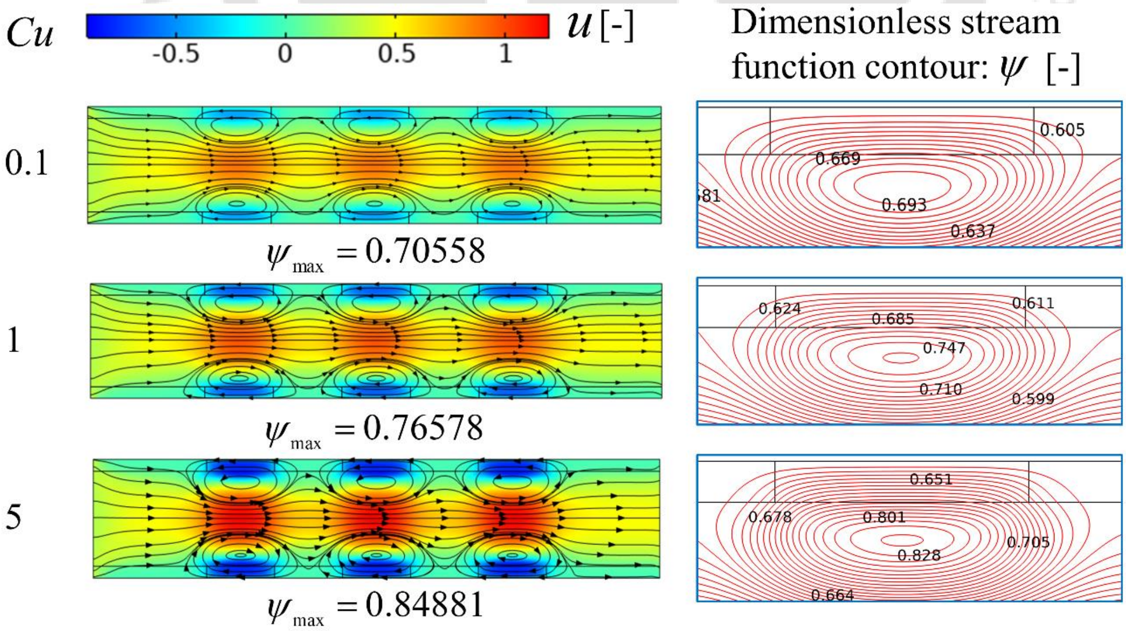

Figure 4.4: Contours of streamlines, dimensionless flow velocity (left side), and stream function (right side) at different Cu (= 0.1, 1, 5). The other parameters are: $L_p = 1.2$, $u_{av} = 0.3$, $d_p = 0.2$, $\kappa_p = 10$, $\kappa = 20$, $n = 0.35$, $F_d = 10$.

- from left to right, and electroosmotic flow (EOF) induced therein from right to left (reverse flow). The EOF actuation from right to left is attributed to the interaction of negatively charged polymeric groups inside the PEL and externally applied electric field acting on the system from right to left. Hence, the positively charged contour-ions near the PEL experience electrostatic body force from right to left, and accordingly EOF commences in the same direction. The underlying interactions lead to the formation of vortices at the PEL junction as witnessed in Fig. 4.4. It is seen from the contours placed in the left panel of Fig. 4.4 that the magnitude of revered EOF velocity as well as the maximum vortex strength $\left(\psi_{\max}\right)$ enhances with increase in Cu. It is because of the decrease in apparent viscosity of the candidate fluids with increasing Cu (see the expression of $\bar{\eta}\left(\dot{\gamma}\right)$ in terms of Cu in Section 4.1; with increasing value of Cu, the shear-thinning nature of the fluid becomes higher), the resistance offered to both forward and reverse flow decreases. We see that the symmetric arrangement of the grafted PEL patches about the channel center line allows the formation of symmetric vortices in the pathway. Formation of these vortices increases the intensity of primary flow velocity at the middle by satisfying the mass conservation constraint. Interestingly, the intensity of primary flow velocity also enhances with increase in Cu, attributed primarily to the higher shear-thinning effect on the underlying dynamics.

Next, we have taken an effort in Fig. 4.5 to demonstrate the effect of geometrical parameters of PEL, frictional drag parameters, and rheological parameters on vortex strength. It is noted that vortex strength is represented here in terms of the maxima magnitude of reverse flow velocity $\left(u_r\right)$ (Mehta et al., 2021; Mehta and Mondal, 2023). The variation of u_r with Cu at different d_p is depicted in Fig. 4.5(a). It is observed that u_r is insensitive to Cu at its smaller value up to the critical value Cu $\left(Cu_{c,u_r}\right)$, while Cu_{c,u_r} decreases with increase in d_p. Also, u_r increases with Cu beyond this critical value. Moreover, u_r increases with increase in d_p for the considered range of Cu as witnessed in Fig. 4.5(a). The physical explanation of these observations is as follows. The insensitiveness nature of u_r with Cu at its smaller value is because of the mild change in apparent viscosity with change in smaller Cu (see the expression of $\bar{\eta}\left(\dot{\gamma}\right)$ in terms of Cu in Section 4.1). While the significant decrease in apparent viscosity with increase in higher value of *Cu* increases the strength of EO flow actuation. Therefore, u_r increases with *Cu* at its higher value beyond $Cu > Cu_{c,u_r}$. The extent of the region where electrostatic body force is acting on the fluid mass increases with d_p. Therefore, the higher strength of EOF that occurs in the opposite of the main flow will be provided by PEL at higher d_p. Accordingly, we get increasing strength of u_r with d_p as can be verified from Fig. 4.5(a). Also, the higher values of shear rate near the interface of primary and secondary flow, as realized for increasing the value of d_p results in smaller apparent viscosity. This interfacial shear rate increases with d_p due to the increase in strength of reverse flow, attributed primarily to augmentation in electroosmotic body force. Therefore, this effect results in a significant decrease in apparent viscosity with *Cu* from its smaller values when d_p is higher. Hence, we get smaller Cu_{c,u_r} for larger d_p.

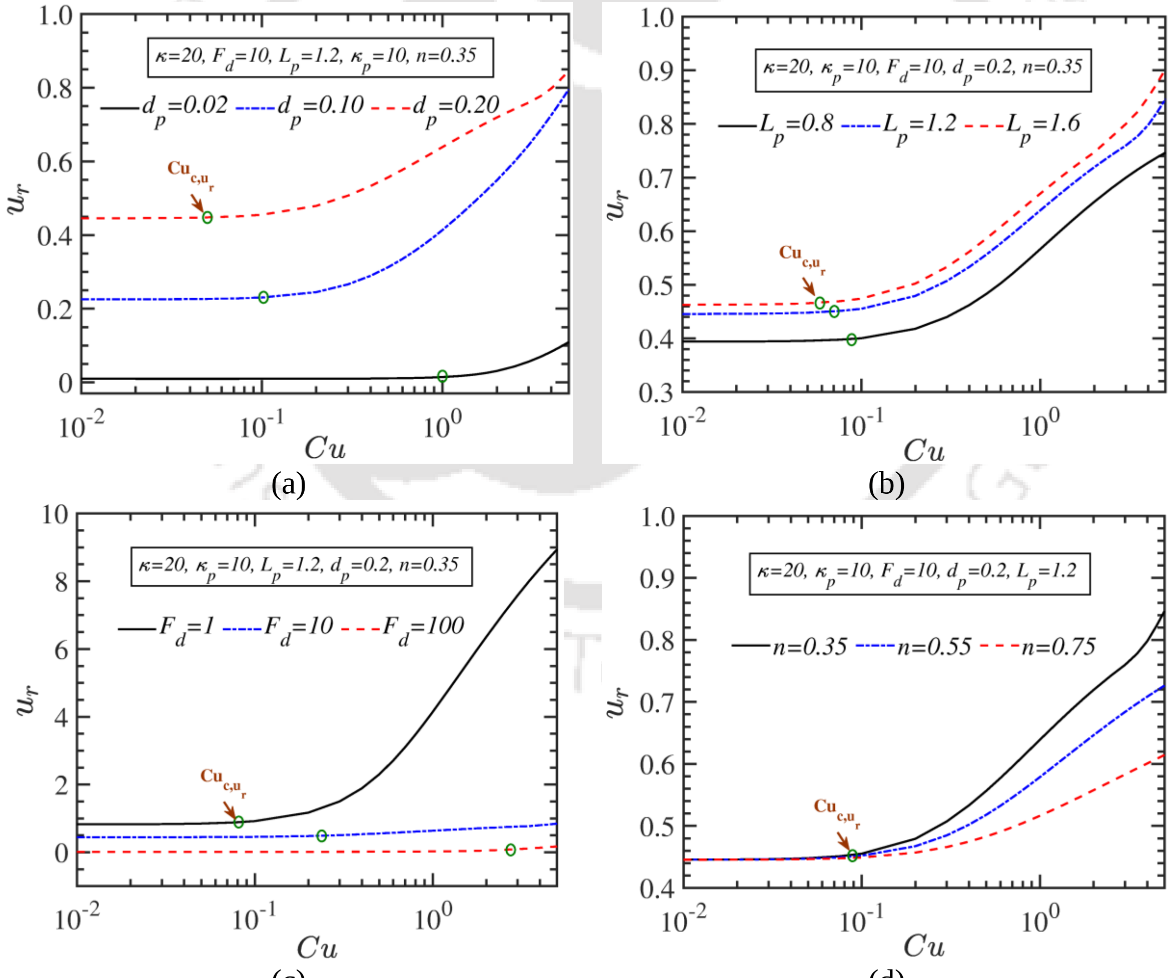

(a) (b)

(c) (d)

Figure 4.5: Variation of recirculation velocity (u_r) with Carreau numbers (Cu) when $\kappa_p = 10$ and $u_{av} = 0.3$ by varying (a) PEL patch thickness when $L_p = 1.2$, $\kappa = 20$, $n = 0.35$, $F_d = 10$; (b) PEL patch length when $d_p = 0.2$, $\kappa = 20$, $n = 0.35$, $F_d = 10$; (c) frictional drag when $d_p =$

0.2, $\kappa = 20$, $n = 0.35$, $L_p = 1.2$;.(d) flow-behavior index when $d_p = 0.2$, $\kappa = 20$, $L_p = 1.2$, $F_d = 10$.

The effect of dimensionless PEL patch length (L_p) on u_r is shown in Fig. 4.5(b). The depicted variations in Fig. 4.5(b) are obtained for different values of Cu. The variation of u_r with Cu is similar to the variation as discussed in the aforementioned paragraph. One can find from Fig. 4.5(b) that u_r increases with increase in L_p. With increasing the value of L_p, the effective area of the PEL patch increases, which in turn, allows larger electrostatic body force alongside a simultaneous increase of the reverse EO actuation. Hence, we get an increase in u_r with L_p. Interestingly, as seen in Fig. 4.5(b), the value of Cu_{c,u_r} increases with increase in L_p as well. It is the increase in L_p that increases the shear rate at the interface of primary and secondary flows owing to the simultaneous increase in acting area of electroosmotic body force and core primary flow intensity. Hence, a higher interfacial shear rate leads to significantly smaller apparent viscosity at a relatively smaller critical Cu number for larger L_p. A substantial weaker flow resistance at smaller Cu for higher L_p results in smaller values of Cu_{c,u_r}, as witnessed in Fig. 4.5(b).

In Fig. 4.5(c), we show the effect of drag coefficient (F_d) on vortex strength with change in Cu. It is found that the rate of increment in u_r with Cu is higher for smaller F_d. Also, Cu_{c,u_r} increases with F_d. The higher rate of increase in u_r with Cu is attributed to a lesser flow resistance offered by the patterned PEL and PL patch arrangements as considered here. A reduction in flow resistance with Cu leads to a sharp enhancement of the reverse flow velocity as well as u_r beyond Cu_{c,u_r}. We found that with the increase in F_d the value of u_r decreases, and this observation is attributed to the increase in flow resistance as F_d rises. Interestingly, the value Cu_{c,u_r} increases with increase in F_d. The additional flow resistance provided by higher drag coefficient allows higher values of Cu_{c,u_r} beyond which a decrease in viscosity with Cu becomes significant on the strength of reversed flow velocity.

We next demonstrate in Fig. 4.5(d) the effect of rheological parameter, i.e., flow-behavior index (n) on u_r with change in Cu is shown in Fig. 4.5(d). We observe that the Cu_{c,u_r} is insensitive to the change in n. We attribute this observation to the significant decrement in apparent viscosity number for all n in the regime of smaller critical Cu.

4.4.2 Species concentration field

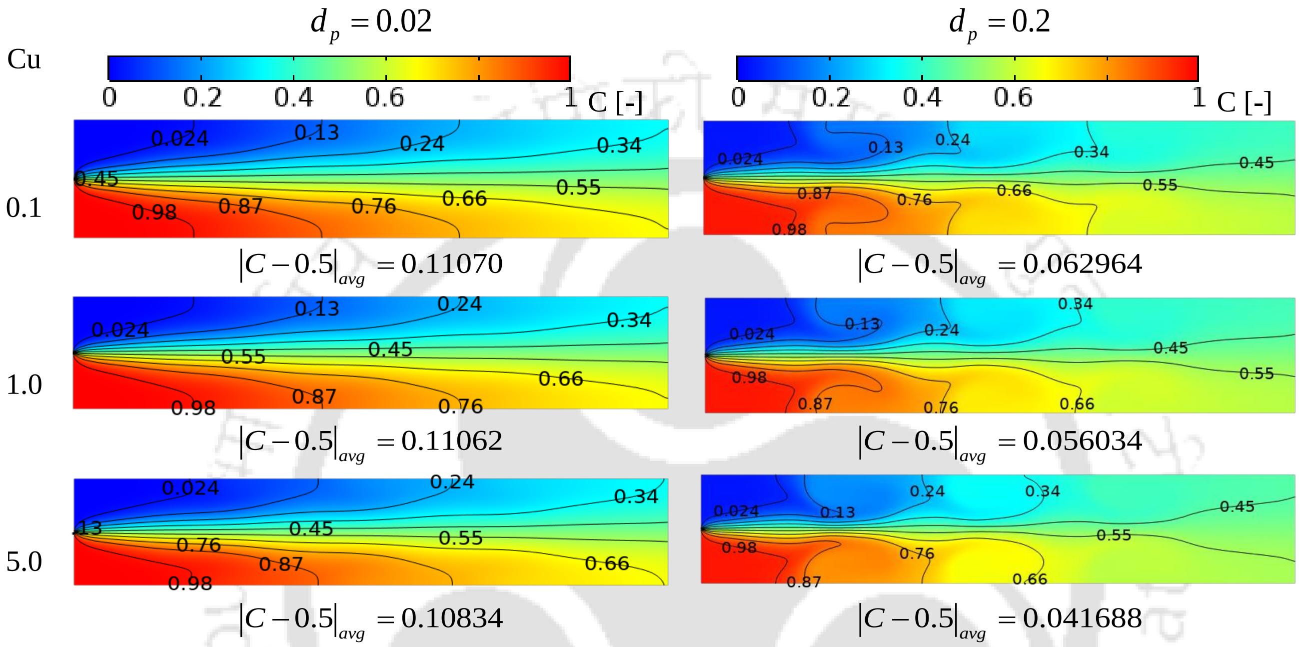

Figure 4.6: Contours of dimensionless species concentration with patch thickness, $d_p = 0.02$ (left side) and $d_p = 0.2$ (right side) at different Cu (=0.1, 1, 5) when $L_p = 1.2$, $u_{av} = 0.3$, $\kappa_p = 10$, $\kappa = 20$, $n = 0.35$, $F_d = 10$, $\mathrm{Pe} = 80$.

To see the effect of fluid rheology on mixing strength of non-Newtonian solutes inside the proposed EO micromixer, the dimensionless species concentration contour for different Cu and d_p is depicted in Fig. 4.6. We observe that an increase in Cu increases the uniformity of dimensionless species concentration as the magnitude of average deviation of concentration $|C-0.5|_{avg}$ at the outlet, as compared to fully mixed state (C = 0.5), decreases with Cu. The decrease in $|C-0.5|_{avg}$ with Cu from 0.1 to 5 is attributed to the augmentation in convective mixing strength with increase in Cu as u_r increases with Cu (see Fig. 4.5). Moreover, the species concentration uniformity is higher when the thickness of the patch is larger as $|C-0.5|_{avg}$ decreases with increase in d_p from 0.02 to 0.2 for a given Cu. This is because of the increase in the strength of the recirculation zone with d_p (see Fig. 4.5(a)) allows greater convective mixing strength at higher patch thickness. Therefore, we get higher species concentration uniformity at the outlet for larger d_p.

4.4.3 Mixing efficiency

Now, an effort has been taken to describe the mixing phenomenon both qualitatively as well as quantitatively, as represented by the variation of mixing efficiency (η) obtained under the modulation of the geometrical, rheological, and electroosmotic parameters. The variation of η with *Cu* at different d_p is depicted in Fig. 4.7(a). We observe from Fig. 4.7(a) that an increase in d_p increases in species concentration uniformity at the outlet (see Fig. 4.6), which in turn, increases the mixing efficiency. The insensitiveness of mixing efficiency with change in smaller *Cu* is attributed to the insensitiveness of vortex strength with change in *Cu* (see Fig. 4.5(a)). Moreover, the increase in vortex strength at higher *Cu* increases the species concentration uniformity (see Fig. 4.6), which in essence increases the mixing efficiency beyond $Cu \geq Cu_{c,\eta}$. The $Cu_{c,\eta}$ follows the same trend as obtained for Cu_{c,u_r} with change in d_p as shown in Fig. 4.5(a), attributed to the convection dominated species transport. Furthermore, the increase in species concentration uniformity at the outlet with d_p (see Fig. 4.6) increases the value of η. Interestingly, for d_p = 0.2, the value of η is $\geq 90\%$ at higher value of *Cu*. Note that in the purview of solute mixing at small scale, $\eta \geq 90\%$ is considered as the fully mixed state. Therefore, we can say that the current micromixer is able to give fully mixed state for higher patch thickness with larger *Cu* number.

The effect of L_p on η, obtained for different values of *Cu*, is depicted in Fig. 4.7(b). We observe that an increase in L_p enhances the value of η. Note that the recirculation strength increases with L_p (see Fig. 4.5(b)), and this in turn, increase the mixing efficiency following the enhancement in convective mixing strength. For this case also, $Cu_{c,\eta}$ follows the same trend as obtained for Cu_{c,u_r} with change in L_p as shown in Fig. 4.5(b). The value of η increases with *Cu* for $Cu \geq Cu_{c,\eta}$ attributed to an increase in convective mixing strength with an increase in u_r (see Fig. 4.5(b)). Notably, the value of η is $>90\%$ for larger L_p $(=1.2,\ 1.6)$ because of higher vortex strength for larger patch lengths.

In Fig. 4.7(c), we show the effect of drag coefficient (F_d) on η with change in Cu. We observe that the increase in F_d decreases the value of η. This is due to increase in reduction in the vortex strength of vortex (see Fig. 4.5(c)) with F_d, which in turn, decreases the strength of convective mixing and hence the mixing efficiency drops. Also, the trend of $Cu_{c,\eta}$ is similar to the Cu_{c,u_r} with change in F_d (see Fig. 4.5(c)). The value of η becomes greater than 90% for lower value of F_d $(=1,\ 10)$. It is because of the higher vortex strength at smaller F_d which provides greater convective mixing strength as well as better mixing quality.

The effect of DH parameter of the PEL (κ_p) on the variation of η, obtained for different values of Cu is depicted in Fig. 4.7(d). It is seen that increasing the value of κ_p increases the value of η. This observation can be explained as follows. The increase in κ_p reduces the thickness of EDL due to the strong attractive force between counter-ions and polyelectrolyte ions at the PEL-bulk electrolyte solution interface. This phenomenon, in turn reduces the corresponding flow resistance to the reverse electroosmotic flow with increase in κ_p. Therefore, the higher electroosmotic flow reversal at higher κ_p allows greater strength of vortex being formed at the PEL interface. Therefore, augmented convective mixing strength with increase in κ_p eventually results in an enhancement of η. Moreover, the value $Cu_{c,\eta}$ decreases with an increase in κ_p. The higher shear rate between the primary and secondary flows develops at higher κ_p allows a significant decrement in the apparent viscosity with Cu from its smaller value and causes substantial augmentation in recirculation velocity as well. Hence, we found, smaller $Cu_{c,\eta}$ for higher κ_p due to the rise in mixing efficiency with Cu from its smaller because of augmented convective mixing strength. Interestingly, the value of η is greater than 95% for higher $\kappa_p(=20)$ in the considered range of Cu. While the value of η is greater than 90% for $\kappa_p=10$ only at a higher value of Cu.

The surface plot of η in the plane of diffusive Peclet number (Pe) and Carreau number (Cu) is displayed in Fig. 4.8(a). We observe that η decreases with increase in

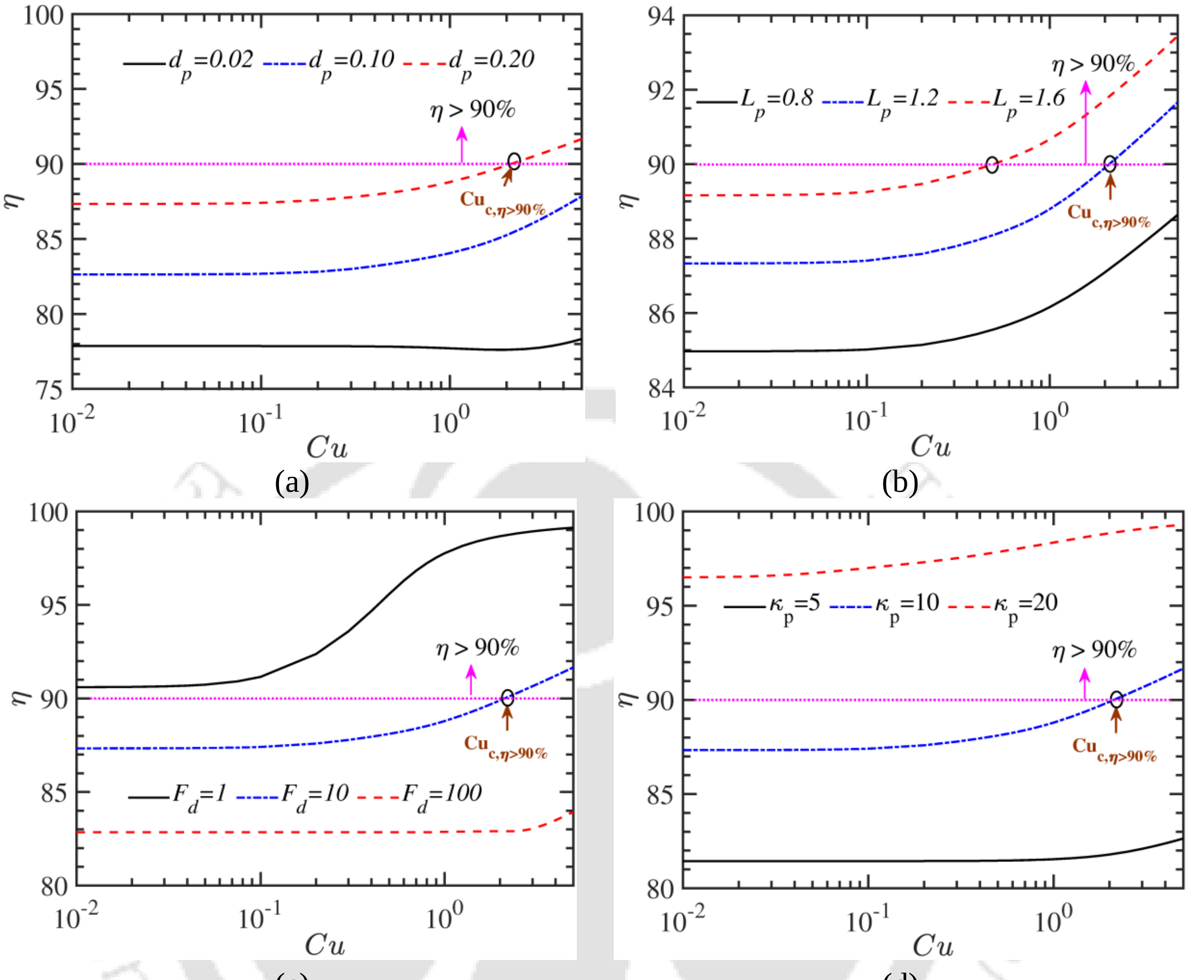

(a) (b)

(c) (d)

Figure 4.7: The variation of mixing efficiency (η) with Carreau numbers (Cu) when $n = 0.35$ and Pe $= 80$ by varying (a) PEL patch thickness when $L_p = 1.2$, $\kappa = 20$, $F_d = 10$ and $\kappa_p = 10$; (b) PEL patch length when $d_p = 0.2$, $\kappa = 20$, $\kappa_p = 10$ and $F_d = 10$; (c) frictional drag when, $d_p = 0.2$, $\kappa = 20$, $\kappa_p = 10$ and $L_p = 1.2$;.(d) PEL DH patch parameters when $L_p = 1.2$, $\kappa = 20$, $L_p = 1.2$ and $F_d = 10$.

- Pe. An increase in Pe decreases the average retention time of species in the domain, and hence the mass diffusion between the solutes decreases. Therefore, species molecules will get very less time to properly mixed and we obtained lesser uniform species concentration at the outlet at higher Pe. Hence, we obtain smaller η at higher Pe. Interestingly, the sharp rate of increment of η with increase in higher Cu is predicted at larger Pe, while the same is weaker at smaller Pe as shown in Fig. 4.8(a). This is attributed to the fact of the augmentation in convective mixing strength at larger Pe. as discussed next. In the regime of higher Pe, the rate of increment in mixing efficiency increases with Cu at its larger value, attributed primarily to the enhancement of recirculation strength enhances (cf. Fig. 4.5). Also, we have shown the surface plot of η in the plane of *Cu* and the flow-behavior index (n) in Fig 4.8 (b). We observe that the value of η is insensitive to *n* at smaller *Cu* because of the insignificant change in flow field by a trivial alteration in apparent viscosity with *n* (see the expression of $\bar{\eta}(\dot{\gamma})$ in terms of *Cu* and n in Section 4.1).

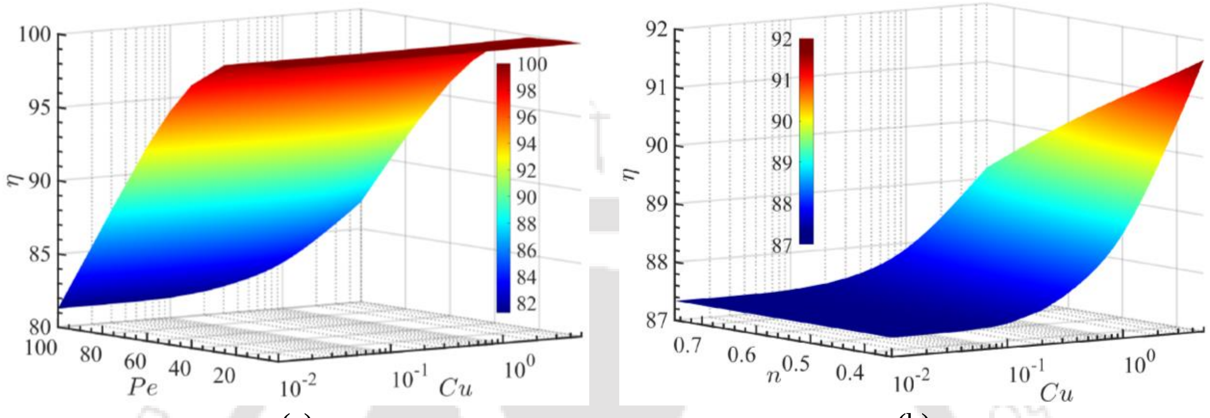

(a) (b)

Figure 4.8: Surface plots showing the three-dimensional variation of mixing efficiency (η): (a) in the plane of diffusive Peclet number and Carreau number when $n=0.35$; and (b) in the plane of flow-behavior index and Carreau number when $\mathrm{Pe}=80$. The other parameters considered for this analysis are: $\kappa=20, F_d = 10$, $d_p = 0.2$, $L_p = 1.2$, $\kappa_p = 10$.

On the other hand, the value of η decreases with increase in *n* at the higher values of *Cu*. This is due to the significant decrease in recirculation velocity with *n* because of the augmented apparent viscosity decreases the convective mixing strength. Notably, the sharp rate of increment in η with higher *Cu* is predicted for smaller *n*. It is due to the sharp augmentation in recirculation velocity with increase in higher *Cu* at smaller *n*, which is attributed to the higher shear-thinning nature of fluid.

4.4.4 Mixing performance

As mentioned before, we consider in this endeavor an applied pressure gradient to drive the bulk solute through the fluidic confinement considered in this analysis, while grafted PEL modulated electrical double layer effect interacted with the applied electrical field leads to the generation of vortices at the PEL interface. Thus, pertaining to this flow configuration, the required pumping power (power needed to drive the constituent solutes through the channel) will be higher when vortex is formed in the pathway in comparison to the no vortex case. Hence, we introduced a parameter called mixing performance $(=\eta/\Delta p_{drop})$, which is defined as the ratio of underlying mixing efficiency to the power required to drive the bulk flow. Certainly, the quantity $\eta/\Delta p_{drop}$ should be maximized for the chosen set up towards justifying the better performance of the proposed configuration. Hence, we have taken an effort to see the effect of geometrical, frictional drag, and rheological parameters on the variation of $\eta/\Delta p_{drop}$, and the corresponding variations are presented in Fig. 4.9. The effect of d_p on $\eta/\Delta p_{drop}$ in the considered range of *Cu* is shown in Fig. 4.9(a). With increasing the magnitude of d_p the resistance being offered to the flow increases, which in turn, pressure-drop. This increase in pressure drop becomes higher as compared to increase in mixing efficiency with d_p (see Fig. 4.7(a)), and eventual consequence is the reduction in $\eta/\Delta p_{drop}$ as witnessed in Fig. 4.9(a). Moreover as seen in Fig. 4.9(a), the mixing performance parameter $\eta/\Delta p_{drop}$ does not change up to critical *Cu* $(Cu_{c,MP})$ and for $Cu > Cu_{c,MP}$, $\eta/\Delta p_{drop}$ sharply increases with *Cu*. The reason behind the insensitive nature of $\eta/\Delta p_{drop}$ with *Cu* up to $Cu_{c,MP}$ is attributed to the mild change in apparent viscosity with change in smaller *Cu*. This mild change in apparent viscosity of the constituent solutes allows a mild change of both η (see Fig. 4.7(a)) as well as Δp_{drop} [due to the insensitive change in u_r with *Cu* (see Fig. 4.5(a))]. While the sharp rise in $\eta/\Delta p_{drop}$ with increase in higher *Cu* is due to the enhancement in η with higher *Cu* (see Fig. 4.7) as well as decrease in Δp_{drop} with *Cu*. It is noted that $Cu_{c,MP}$ increases with increase in d_p. This is because of the higher flow resistance offered by a larger PEL thickness allows huge Δp_{drop}. Hence, the rise in $\eta/\Delta p_{drop}$ with *Cu* is suppressed up to higher *Cu* when d_p is larger.

The effect of L_p on $\eta/\Delta p_{drop}$ with change in *Cu* is shown in Fig. 4.9(b). With increasing the value of L_p, the pressure drops and flow resistance both rise due to an increase in recirculation velocity (see Fig. 4.5(b)). This rise in pressure drop decrease $\eta/\Delta p_{drop}$ as witnessed in Fig. 4.9(b). Moreover, $Cu_{c,MP}$ follows the same trend with increase in L_p as obtained for d_p in Fig. 4.9(a).

In Fig. 4.9(c), we show the variation of $\eta/\Delta p_{drop}$ at different F_d with change in Cu. Interestingly, the non-monotonic effect of F_d on $\eta/\Delta p_{drop}$ is predicted. The increase in value of F_d from 1 to 10, increases $\eta/\Delta p_{drop}$, while increase in the same from 10 to - 100 decreases the value of $\eta/\Delta p_{drop}$. This observation can be attributed to the decrease in Δp_{drop} with change in F_d from 1 to 10 which in turn increases $\eta/\Delta p_{drop}$. The rise in Δp_{drop} with change in F_d from 1 to 10 is attributed to reduction in flow resistance offered by vortices as u_r decreases with F_d (see Fig. 4.5(c)). For the higher values of F_d (=10 to 100), the excessive flow resistance offered by the drag force in PEL and PL amplified

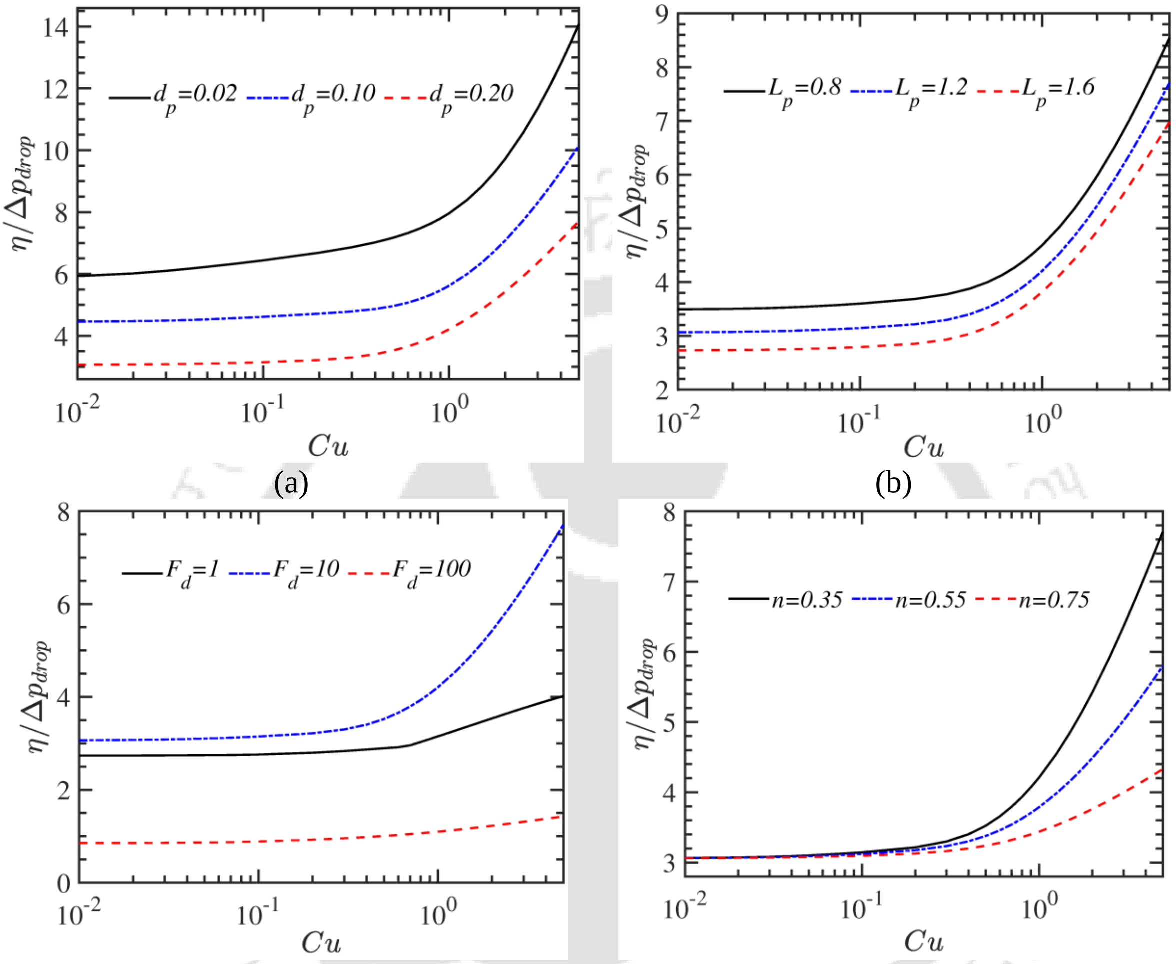

(a) (b)

(c) (d)

Figure 4.9: Variation of mixing performance $(\eta/\Delta p)$ with Carreau numbers (Cu) when $\kappa_p = 10$ by varying (a) PEL patch thickness when $L_p = 1.2$, $\kappa = 20$, $n = 0.35$ and $F_d = 10$; (b) PEL patch length when $d_p = 0.2$, $\kappa = 20$, $n = 0.35$ and $F_d = 10$; (c) frictional drag when $d_p = 0.2$, $\kappa = 20$, $n = 0.35$ and $L_p = 1.2$;.(d) flow-behavior index when $d_p = 0.2$, $\kappa = 20$, $L_p = 1.2$ and $F_d = 10$.

the value of Δp_{drop}. Hence, the sharp increase in Δp_{drop} at higher values of F_d (=10 to 100) reduces the value of $\eta/\Delta p_{drop}$. The higher vortex strength for smaller F_d (=1) as seen from Fig. 4.5(c), which allows substantially larger flow resistance that causes pressure drop reduction (since apparent viscosity deceases with *Cu*) from higher *Cu* value. On the other hand, with a higher value of F_d (=100), the stagnant flow within the PL and PEL is caused by the immense drag resistance, which permits a negligible strength of recirculation velocity (see Fig. 4.5(c)). Therefore, the flow resistance is substantially lower due to the weaker vortex strength, which decreases the pressure drop with *Cu* relatively at its smaller values.

Also, the effect of flow-behavior index (n) on $\eta/\Delta p_{drop}$ with change in *Cu* is shown in Fig. 4.9(d). It is noted that $\eta/\Delta p_{drop}$ decreases with increase in *n* at the higher values of *Cu*. This is due to the decrease in shear-thinning behavior with increase in *n* enhances the value of apparent viscosity (see the expression of apparent viscosity, $\bar{\eta}(\dot{\gamma})$ in Section 4.1) and enhance the value of Δp_{drop}. Additionally, the value of $\eta/\Delta p_{drop}$ with *n* is insensitive up to $Cu_{c,MP}$ due to the insensitive nature of η and Δp_{drop} with *Cu* as witnessed in Fig. 4.9(d). Interestingly, $Cu_{c,MP}$ is insensitive with change in *n*. This is because of *Cu* is present at the base of expression of $\bar{\eta}(\dot{\gamma})$ while *n* is present at the index. Hence, the significant decrement in apparent viscosity is observable beyond the critical *Cu* for all *n*.

4.5 Shear-modulated binary aggregation kinetic

Pertaining to the mixing of non-Newtonian solutes containing biomolecules such as DNA, blood plasma, and protein molecules, the estimation of aggregation kinetics seems to be important for the probable prediction of the inherent properties of the biomolecules (Zaccone et al., 2009). It should be noted that as a result of aggregation, which depends on both the diffusion and the advection fields, the number density of the particles varies locally. Additionally, an adverse shearing intensity becomes vulnerable for the biomolecules as it may deteriorate their inherent biological characteristics. Therefore, in LOC applications involving biological fluids, the quantitative estimation of a parameter related to the shear-rate-dependent aggregation kinetics of biomolecules is of utmost significance. With this as motivation, the characteristic time of the binary aggregation, which is inversely proportional to the reaction rate of binary aggregation kinetics, is determined by assuming two-body aggregation of particles that is affected by shear rate (Zaccone et al., 2009; Gaikwad et al., 2020):

$$t_c \sim \frac{\exp\left(-6\pi\alpha_s\mu_0^*\dot{\gamma}_m^* a^3 / K_b T\right)}{\sqrt{3\pi\alpha_s\mu_0^*\dot{\gamma}_m^* a^3 / K_b T}} \tag{4.8}$$

Where numerical coefficient, $\alpha_s = 1/3\pi$; the colloidal radius of the particle, $a = 100$ nm; $\mu_0^* = 0.056$ Pa-s; T = 300 K and $\dot{\gamma}_m^*$ is the maximum shear rate. Noted that the normalized number concertation of particles (C_N) at any instant of time, t can be correlated to t_c as $C_N = \left(1/\left(1+\left(t/t_c\right)\right)\right)$ (Zaccone et al., 2009). Further, the order of particle aggregation Peclet number $(Pe_c = (u_{HS}^*)a/D_p)$ is obtained as 8.063 for $u_{HS}^* = 3.161\times10^{-6}$ m-s^{-1} and particle diffusion coefficient, $D_p = K_b T/6\pi\mu_0^* a$ (= 3.92×10^{-14} m^{2}s^{-1}).

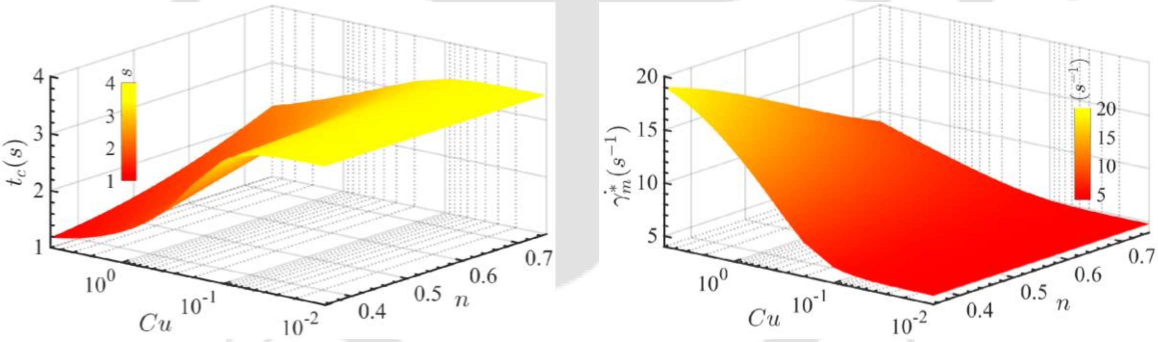

(a) (b)

Figure 4.10: Three-dimensional variation at section x = 2.6 of (a) characteristics time of the binary aggregation kinetics (t_c) and (b) maximum shear rate ($\dot{\gamma}_m^*$) in the plane of the flow-behavior index (n) and Carreau numbers (Cu) when $\kappa = 20$, $F_d = 10$, $d_p = 0.2$, $L_p = 1.2$, $\kappa_p = 10$, and $u_{av} = 0.3$.

Hence, $Pe_c > 1$ signifies that the particle aggregation kinetics must be dependent on the convection field. Motivated by this fact, we have investigated the shear-induced binary aggregation kinetics for the mixing of biofluids. In this part, the three-dimensional variation of t_c in the plane of Cu and n is depicted in Fig. 4.10(a), and the corresponding maximum shear rate ($\dot{\gamma}_m^*$) is depicted in Fig. 4.10(b) in the same plane. We observe that t_c is insensitive to an increase in smaller Cu, while a sharp decrement of the same is predicted with an increase in higher values of Cu. This rate of decrement in t_c with higher

Cu is sharper when the shear-thinning nature of fluid is higher (i.e., smaller *n*). These observations can be explained by the variation of $\dot{\gamma}_m^*$ in the same plane (*n* and *Cu*) as depicted in Fig. 4.10 (b). By observing Eq. (4.8), it is found that t_c ultimately follows an inverse relationship with $\dot{\gamma}_m^*$. Additionally, it is observed that the maximum shear rate exists near the interface of the PEL-solute (electrolyte layer). As a result, $\dot{\gamma}_m^*$ becomes higher for the higher values of *Cu* because of the increase in-reversed EO flow velocity with *Cu* (see Fig. 4.5). The higher EO velocity results in an augmented shear rate at that interface. Hence, in the regime higher values of *Cu*, t_c decreases with an increasing magnitude of *Cu*. The sharp increment in reversed EO flow velocity with *Cu* at smaller *n* (see Fig. 4.5(d)) allows a sharp increase in the shear rate at the PEL-solute interface with *Cu*. Therefore, the sharp decrement in t_c with an increase in higher *Cu* is predicted when *n* is smaller. The increase in *n* enhances the values of t_c for the higher values of *Cu*. We attribute this observation to the decrease in $\dot{\gamma}_m^*$ with *n* at the higher values of *Cu* as the reversed electroosmotic flow velocity decreases with *n* (see Fig. 4.5(d)).

4.6 Summary

In this investigation, we explored the impact of the co-dependent interplay between polyelectrolyte layer (PEL)-modulated interfacial electrostatics and pressure-driven bulk flow on the flow field and mixing characteristics of non-Newtonian solutes within a micromixer. The rheology of the non-Newtonian solutes was represented using the Carreau fluid model. We examined the flow dynamics and mixing characteristics of shear-thinning non-Newtonian solutes by varying parameters such as the geometrical features of the grafted PEL, electrokinetic properties of the PEL, rheological attributes of the solutes, and the diffusive Peclet number. The presence of a fixed charge in the grafted PEL, influenced by an external electric field, induced the formation of an electric double layer at the PEL electrolyte interface. This, in turn, facilitated the generation of vortices with varying scales through momentum exchange with the bulk flow. Our findings revealed that an increase in the Carreau number, indicating the degree of shear-thinning behavior of solutes, led to enhanced strength and size of vortices (recirculation velocity) at the PEL electrolyte interface. We identified a critical Carreau number associated with a change in recirculation velocity strength, and this critical value varied with parameters such as drag coefficient, PEL patch thickness, and length. The recirculation velocity was found to be insensitive to the flow-behavior index up to the critical Carreau number, after which it decreased with higher values of this parameter. Additionally, an augmentation in convective mixing strength, linked to the shear-thinning nature of components, improved species concentration uniformity at the micromixer outlet with higher Carreau numbers. Notably, our analysis demonstrated that mixing efficiency surpassed 90% for larger values of normalized PEL patch thickness and length at higher Carreau numbers. We reported that mixing efficiency exceeded 90% within the considered Carreau number range for smaller drag coefficients (= 1) and higher normalized PEL Debye-Hückel parameter (= 20). Furthermore, we calculated the characteristic time of shear-induced binary aggregation kinetics for non-Newtonian biofluids consisting of biomolecules. The analysis showed a sharp decrement in the characteristic time of binary aggregation kinetics for higher Carreau numbers, primarily attributed to the higher shear-thinning nature of the fluid. Moreover, an increase in the flow-behavior index was found to enhance the characteristic time of binary aggregation kinetics for higher Carreau numbers.

Chapter 5

Effective solute mixing of non-Newtonian fluid through the modulation of electroosmotic vortices using a pH-dependent soft polyelectrolyte layer

According to a comprehensive review of the literature, the vortex production mechanism is of paramount importance when dealing with the mixing phenomenon in microfluidic systems. Besides, the liquids employed in the mixing phenomenon often exhibit non-Newtonian behavior. Furthermore, the electroosmotic vortex can be manipulated by grafting polyelectrolyte layers into microfluidic devices under an external electric field. Interestingly, due to spontaneous protonic exchange in the presence of aqueous solution, these polyelectrolyte acidic and basic groups are often extremely sensitive to solution pH (Pandey et al., 2022; Chen and Hsu, 2022; Mehta et al., 2023). As a result, this protonic exchange can impact the ionic field, reshaping the electrical forcing strength and flow pattern. Despite this, the electroosmotic vortex generation and mixing characteristics of non-Newtonian liquids have not been investigated in terms of protonic exchange between the polyelectrolyte group and mobile electrolytic species. To address this research gap, the current numerical investigation employed a microchannel with a pH-sensitive polyelectrolyte layer along with a pH-sensitive zeta potential to explore the underlying physics of vortex production and mixing phenomena.

5.1 Mathematical Formulation

The fluidic configuration depicted in Fig. 5.1 illustrates a plane micromixer with the following dimensions: height = $2H$ and length L is $10H$. In the central region of the top wall of this micromixer, there is a polyelectrolyte layer (PEL) patch grafted axially. This patch is characterized by its length $L_P^* = H$ and width, $t_p^* = 0.2H$. Notably, the PEL is filled with a semi-permeable polyelectrolyte material, and its space charge density considered to be pH-sensitive.

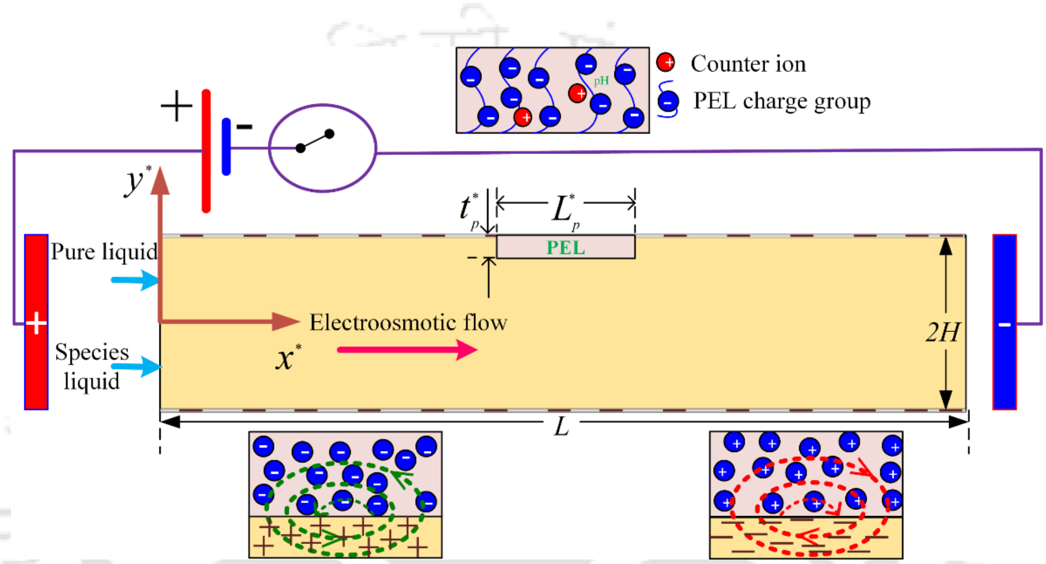

Figure 5.1: Sketch of schematic diagram of vortex induced electroosmotic mixing depicting a pH sensitive PEL patch arrangement, and dimensions of the micromixer. Here, inlet upper part of the domain is pure liquid, and bottom part domain is species liquid which is mixture of the same base fluid and electrically neutral tracer particles.

The surface (zeta) potential of microchannel wall is considered to be pH and ionic concentration sensitive. The micromixer ends have been subjected to an external electric potential difference, ΔV to produce electroosmotic vortices essentially towards achieving better convective mixing strength. The PEL contains acidic (–COOH) and basic (–NH$_2$) functional groups are associated with equilibrium constants K_A and K_B, respectively. The pH-tunable PEL space charge density $\left(\sigma_{PEL}\left(\mathrm{C/m^3}\right)\right)$ is expressed as (Mehta et al., 2023):

$$\sigma_{PEL}\left(\mathrm{C/m^3}\right)=\frac{F\times 10^{18}}{t_p^*\times N_A}\left[\frac{\Gamma_B}{\left(K_B/[H]^+\right)+1}-\frac{\Gamma_A}{1+\left([H]^+/K_A\right)}\right] \tag{5.1}$$

Where, F = Faraday constant; N_A = Avogadro's constant; $\Gamma_A = \Gamma_B = 0.5$ number of polyelectrolyte group per nm^2; $[\mathrm{H}]^+ = 10^{-\mathrm{pH_b}}$ M, which is the molar concentration of H^+ ions; $K_A = 10^{-pK_A}$ with $pK_A = 2.2$ and $K_B = 10^{-pK_B}$ with $pK_B = 9$ (Pandey et al., 2022). Also, in Fig. 5.1, the tractor species introduced as a mixing agent, which is intended to blend with a pure non-Newtonian liquid (referred to as pure liquid), is denoted as species liquid with a diluted concentration (C_0^*). Species liquid is introduced at the lower half of the inlet, whereas pure non-Newtonian liquid is introduced at the upper half of inlet to assess the underlying mixing strength of this endeavour.

Certain physically justifiable assumptions have been employed in this analysis so as to model the underlying phenomena mathematically in the chosen fluidic configuration. It is assumed that both the fluids, i.e., pure and tracer fluids, are incompressible and we consider 2D analysis in this study. We ignore the effect of finite ionic size in the underlying analysis, attributed primarily to the lower value of bulk ionic concentration (Nayak et al., 2020). The order of external electric field considered in this analysis is 10^4 V/m, and the chosen field strength allows us to ignore the Joule heating effect (Mehta et al., 2021; Mehta and Mondal, 2023). Additionally, the order of induced electric field, Ψ_{ref}^* / λ_D, where Ψ_{ref}^* and λ_D are the reference electrical-double layer (EDL) potential and characteristic EDL thickness respectively, order within the EDL is significantly higher than that of the externally applied electric field (Gaikwad et al., 2020; Kumar et al., 2023). Consequently, the influence of the external electric field on the ionic distribution within the EDL is neglected. Also, the generation of difference in Born energy owing to the difference in permittivity of PEL and electrolyte is ignored because of the consideration of the monovalent ionic species (K^+ and Cl^-) (Pandey et al., 2022; Chen and Hsu, 2022; Mehta et al., 2023). It may be mentioned here that for the monovalent ionic species, the magnitude of Born energy is trivial as compared to the energy associated with the induced EDL field induced by the charged surface.

To describe the ionic concentration field, we employ the Nernst-Planck equation. Below we write the steady-state non-dimensional form of the Nernst-Planck equation (Gaikwad et al., 2020):

$$\mathrm{Pe_I}\left[\frac{\partial \bar{n}_i}{\partial \bar{t}} + \nabla \cdot \left(\bar{n}_i \mathbf{u}\right)\right] = \nabla^2 \bar{n}_i + \nabla \cdot \left(\bar{n}_i \nabla \Psi\right) \qquad (5.2)$$

In Eq. (5.2), $\mathrm{Pe_I}(=u_{HS}^{*}H/D_i)$ is the ionic Peclet number; $\bar{n}_{i\pm}=n_{i0}\exp(\mp ez_i\Psi^{*}/k_bT)$ represents the i^{th} type (i = 1, 2 , 3, and 4 for $\mathrm{K^+}$, $\mathrm{Cl^-}$, $\mathrm{H^+}$ and $\mathrm{OH^-}$, respectively) of ionic species where n_{i0} represents the bulk ionic concentration of corresponding ionic species in mM (= mol/m^3); D_i is the ionic diffusion coefficient; **u** is the dimensionless velocity field; Ψ is the dimensionless induced electrostatic potential. Based on the physically justified assumptions as considered in this study and discussed before, the order of magnitudes of $\mathrm{Pe_I}$ is calculated to be in the range of 10^{-2} to 10^{-4} for microscale transport (Gaikwad et al., 2020). Accordingly, using the proper boundary conditions to maintain electroneutrality in the solution, the concentrations of the four ionic species ($\mathrm{K^+}$, $\mathrm{Cl^-}$, $\mathrm{H^+}$ and $\mathrm{OH^-}$) are adjusted based on the bulk solution pH (pH$_\mathrm{b}$) using KOH and HCl (Pandey et al., 2022). Also, for pH$_\mathrm{b}$ ≤ 7; $n_{10}=n_0$, $n_{20}=n_0+10^{-\mathrm{pH_b}+3}-10^{-(14-\mathrm{pH_b})+3}$, $n_{30}=10^{-\mathrm{pH_b}+3}$, $n_{40}=10^{-(14-\mathrm{pH_b})+3}$ and for pH$_\mathrm{b}$ > 7; $n_{10}=n_0-10^{-\mathrm{pH_b}+3}+10^{-(14-\mathrm{pH_b})+3}$, $n_{20}=n_0$, $n_{30}=10^{-\mathrm{pH_b}+3}$, $n_{40}=10^{-(14-\mathrm{pH_b})+3}$. These expressions account for different conditions based on whether pH$_\mathrm{b}$ is less than or equal to 7 or greater than 7 (Chen and Hsu, 2022).

The transport equations in their non-dimensional forms are written in Eqs. (5.3) to (5.7) (Gaikwad et al., 2020; Pandey et al., 2022). The modified non-dimensional form of Poisson–Boltzmann equation describing dimensionless EDL potential field (Ψ) can be represented by Eq. (5.3) as:

$$\Theta_\varepsilon\left(\nabla^2\Psi\right)=\kappa^2\sinh\left(\Psi\right)-\Omega\kappa_p\left(\frac{\Gamma_B/\Gamma_A}{1+K_B/[\mathrm{H}]^+}-\frac{1}{1+[\mathrm{H}]^+/K_A}\right) \tag{5.3}$$

Here, Θ_ε is taken as 1 for free electrolytic region and $\Theta_\varepsilon=\varepsilon_{r,p}/\varepsilon_r=0.25$ (Pandey et al., 2022; Chen and Hsu, 2022; Mehta et al., 2023); where ε_r and $\varepsilon_{r,p}$ represent electrolyte relative permittivity and polyelectrolyte relative permittivity, respectively.

Also, the non-dimensional form of the Laplace equation describing dimensionless external potential field (Φ) is represented by Eq. (5.4) as:

$$\nabla^2\Phi=0 \tag{5.4}$$

The modified non-dimensional form of the continuity and momentum transport equations for fluid flow, used to describe dimensionless flow velocity ($\mathbf{u} = u_x i + u_y j$), is represented by Eqs. (5.5) and (5.6), respectively read as:

$$\nabla \cdot \mathbf{u} = 0 \tag{5.5}$$

$$\mathrm{Re}\left(\mathbf{u} \cdot \nabla\right)\mathbf{u} = -\nabla p + \nabla \cdot \boldsymbol{\tau} + \kappa^2 \sinh\left(\Psi\right)\nabla(\Psi/\varpi + \Phi) - \Lambda F_d^2 \mathbf{u} \tag{5.6}$$

In Eq. (5.6), ϖ denotes the ratio of reference external potential to the reference EDL potential, i.e., $\varpi = \Phi_{ref}^* / \Psi_{ref}^*$.

Finally, for the species transport, the modified non-dimensional form of the convection-diffusion equation with dimensionless species concentration field (C) is given by Eq. (5.7) as:

$$\mathrm{Pe}\left(\mathbf{u} \cdot \nabla C\right) = \nabla^2 C \tag{5.7}$$

The non-dimensional parameters considered for the present analysis [Eqs. 5.3, 5.4, 5.5, 5.6, and 5.7] are defined as (Gaikwad et al., 2020): $x = x^*/H$, $y = y^*/H$, $L_p = L_p^*/H$ $t_p = t_p^*/H$; $\Psi = \Psi^*/\Psi_{ref}^*$, $\Psi_{ref}^* = k_b T/ze$; $\Phi = \Phi^*/\Phi_{ref}^*$, $\Phi_{ref}^* = (\Delta V)H/L$; $\mathbf{u} = \mathbf{u}^*/u_{HS}^*$. Note that reference quantities are as follows: the Helmholtz–Smoluchowski reference velocity is $u_{HS}^* = \varepsilon_0 \varepsilon_r E_{ref}^* \Psi_{ref}^* / \mu_0^*$, $E_{ref}^* = \Delta V/L$; $p = p^* H / \mu_0^* u_{HS}^*$; Re = $\rho u_{HS}^* H / \mu_0^*$; Pe = $u_{HS}^* H / D$, where D is the diffusion coefficient of the tracer species; $C = C^*/C_0^*$, here C_0^* is inlet tracer species concentration at the bottom side inlet. The dimensionless Debye–Hückel (DH) parameter of electrolyte layer (κ) and poly electrolyte layer (κ_p) are defined based on Eq. (5.3) are given as $\kappa = \sqrt{2Fn_0 H^2 / \varepsilon_0 \varepsilon_r \Psi_{ref}^* \left\{1 + 10^{-\mathrm{pH_b}+3}/n_0\right\}}$ for $\mathrm{pH} \le 7$, $\kappa = \sqrt{2Fn_0 H^2 / \varepsilon_0 \varepsilon_r \Psi_{ref}^* \left\{1 + 10^{-(14\text{-}\mathrm{pH_b})+3}/n_0\right\}}$ for $\mathrm{pH} > 7$ and $\kappa_p = 10^{18} \times eH^2 \Gamma_A / (t_p \varepsilon_0 \varepsilon_{r,p} \Psi_{ref}^*)$, respectively. Here $\varepsilon_0, \varepsilon_r, \varepsilon_{r,p}, e$ and n_0 are used to denote free space permittivity, electrolyte relative permittivity, polyelectrolyte relative permittivity, the charge of an electron and bulk ionic concentration (10^{-6} to 10^{-4} M) (Pandey et al., 2022), respectively. Also, $\Omega = 0$ and 1 in Eq. (5.3); $\Lambda = 0$ and 1 in Eq. (5.6), represent PEL-free region and PEL region, respectively. Moreover, F_d in Eq. (5.6) is the flow resistance provided by the PEL porous structures, called Darcy's frictional drag (Gaikwad et al., 2020). The dimensionless deviatoric stress tensor in Eq. (5.6) is written as $\boldsymbol{\tau} = \bar{\eta}(\dot{\boldsymbol{\gamma}})\left(\nabla\mathbf{u} + (\nabla\mathbf{u})^T\right)$ (Kumar et al., 2023), which is made non-dimensionless using the scale $\mu_0^* u_{HS}^* / H$. The dimensionless apparent viscosity according to Carreau model is given as $\bar{\eta}(\dot{\boldsymbol{\gamma}}) = \mu_\infty^* + (1-\mu_\infty^*)\left(1 + Cu^2\dot{\boldsymbol{\gamma}}^2\right)^{n-1/2}$, where $\dot{\boldsymbol{\gamma}}$ is the dimensionless second invariant of rate of deformation tensor and given as, $\dot{\boldsymbol{\gamma}} = \sqrt{0.5(\mathbf{S}:\mathbf{S})}$. Here, $\mathbf{S}$ represents the dimensionless strain rate tensor and expressed as $\left(\nabla\mathbf{u} + (\nabla\mathbf{u})^T\right)$; Further, $\bar{\mu}_\infty$ represent the dimensionless infinity shear rate viscosity normalized with the zero shear rate viscosity, μ_0^*; Cu is the Carreau number and expressed as $\lambda u_{HS}^* / H$; n represents the flow behavior index and λ is the time parameter for Carreau model. Furthermore, the non-dimensional solution pH (here: bulk value pH$_b$) dependent zeta potential (ζ, here ζ = ζ^* / Ψ_{ref}^* and Ψ_{ref}^* is taken as 25 mV) is taken based on the experimental data, and expressed as $\zeta(\mathrm{pH_b}, n_0)$ = $((-\log 10(n_0)) \times (0.4836 \times \mathrm{pH_b}^2 - 10.93 \times \mathrm{pH_b} + 24.44)/25)$ (Tandon et al., 2008).

The following boundary conditions are imposed to solve the Eqs. (5.3) to (5.7) numerically (Kumar et al., 2023); At inlet: $\mathbf{n}\cdot\nabla\Psi = 0,\ \Phi = 10$, $p_g = 0$, $C = 0$ for $0 \le y \le 1$ and $C = 1$ for $-1 \le y \le 0$; at the wall: $\Psi = \zeta(\mathrm{pH_b}, n_0),\ \mathbf{n}\cdot\nabla\Phi = 0,\ \mathbf{u} = 0$, $\mathbf{n}\cdot\nabla C = 0$; at outlet: $\mathbf{n}\cdot\nabla\Psi = 0,\ \Phi = 0,\ p_g = 0$, $\mathbf{n}\cdot\nabla C = 0$; at the interface of PEL and void region; $\Psi_{PEL} = \Psi_{void}$, $\Theta(\nabla\Psi_{PEL}) = \nabla\Psi_{void}$, $\Phi_{PEL} = \Phi_{void}$, $\Theta(\nabla\Phi_{PEL}) = \nabla\Phi_{void}$, $\mathbf{u}_{PEL} = \mathbf{u}_{void}$, $\boldsymbol{\tau}_{PEL} = \boldsymbol{\tau}_{void}$, $C_{PEL} = C_{void}$.

To quantify the mixing quality in the chosen microfluidic configuration, the mixing efficiency at outlet is calculated as (Gaikwad et al., 2020):

$$\eta_m = 100\left(1 - \left(\int_{y=-1}^{y=1} \left(\left|C - C_\infty\right|\right) \Big/ \int_{y=-1}^{y=1} \left(\left|C_0 - C_\infty\right|\right)\right)\right) \tag{5.8}$$

Here, C_0 (= 0 or 1) and C_∞ (= 0.5) in Eq. (5.8) represent the dimensionless concentration of species at unmixed and mixed states, respectively.

5.2 Numerical methodology and model benchmarking

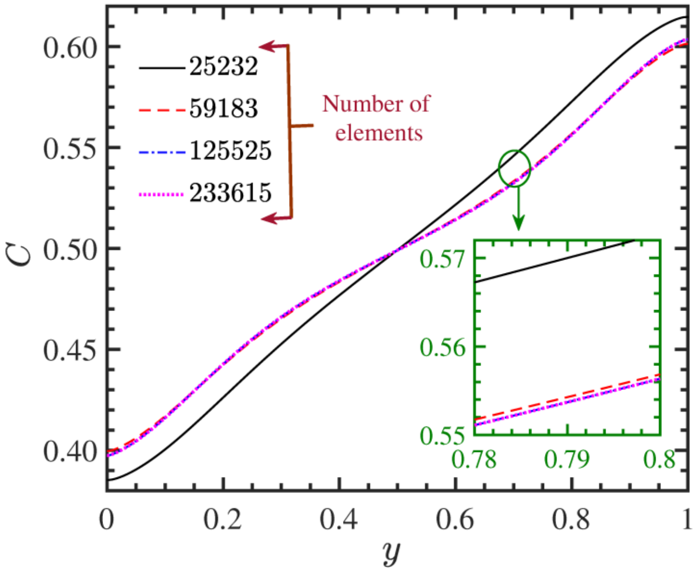

Figure 5.2: The non-dimensional species concentration comparison at the outlet of micromixer by changing the number of mesh elements from 25,232 to 2,33,615. The other parameters considered for the comparison are: $L_p = 1.0$, $t_p = 0.2$, $n_0 = 10^{-5}\,\mathrm{M}$, n = 0.5, $F_d = 10$, pH$_b$ = 4.2, Cu = 0.2, and Pe = 100.

In this study, we solve the transport Eqs. (5.3) to (5.7) numerically in the framework of COMSOL® Multiphysics, (2015) in serial mode. For the simulations, we used workstation having the specifications as follows: 8 cores with 16 logical processor, ram 32 GB and base speed 3.41 GHz. The computational domain of the micromixer shown in Fig. 5.1 is discretized into subdomains using non-uniform triangular mesh elements. The mesh is specifically refined in areas proximal to the inlet, fluid interface section, walls, and the PEL patch to ensure a higher density. This strategic mesh refinement is implemented to enhance the accuracy of predicting all relevant transport variables pertinent to this analysis. The Galerkin weighting method is applied to transform the governing differential equations into integral equations. Subsequently, an iterative solution approach is employed to achieve a relative residual value of 10^{-6} for all the transport variables. To ascertain the accuracy of model developed here, we conducted a grid independence test, illustrated in Fig. 5.2, focusing on the dimensionless species concentration at the outlet of the micromixer. The parameters considered to perform the grid independence test are: $L_p = 1.0$, $t_p = 0.2$, $n_0 = 10^{-5}\,\mathrm{M}$, n = 0.5, $p_g = 0$, $F_d = 10$, pH = 4.2, Cu = 0.2, and Pe = 100. We observe from Fig. 5.2 that as the number of mesh elements increased beyond 125525, the profiles are closely aligned, and the percentage error is found to be less than 0.1%. Therefore, to optimize computational efficiency, we chose a mesh configuration with 125525 elements for all the simulations performed in this endeavour.

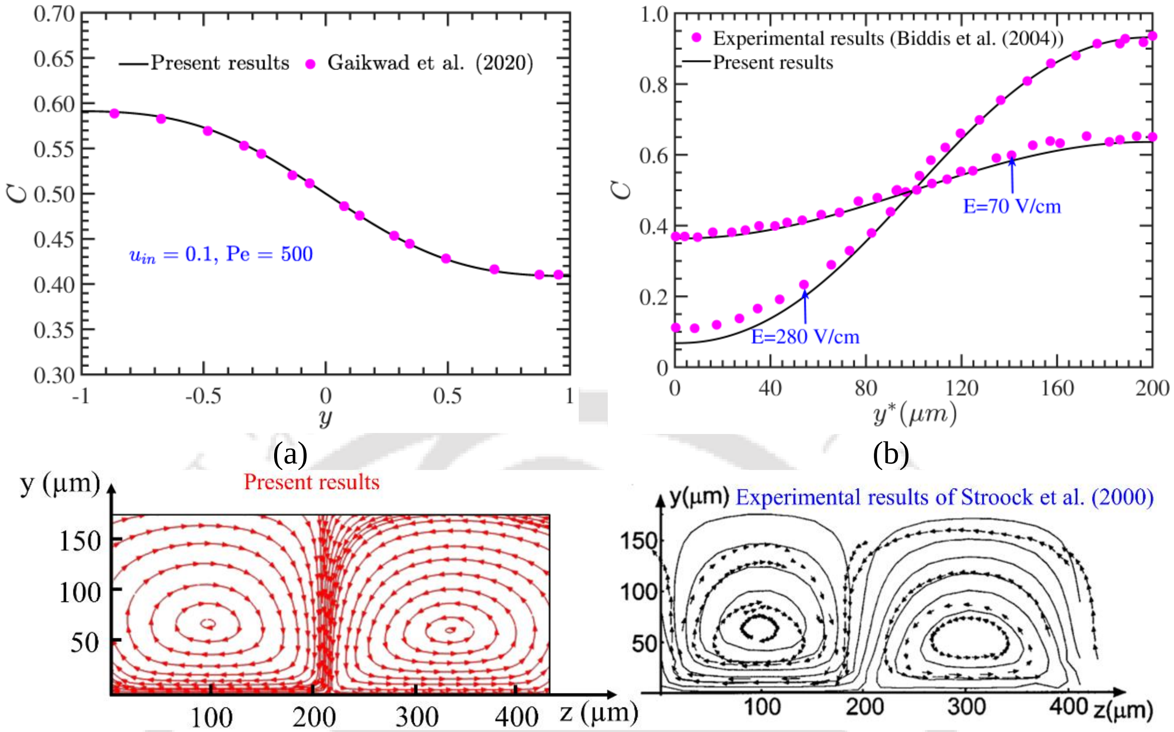

(a) (b)

(c)

Figure 5.3: (a) Represents the validation of dimensionless species concentration at the section x = 5 with limiting Newtonian fluid (n = 1) case in the electroosmotic micromixer having PEL layer with the numerical work by Gaikwad et al., (2020). The other parameters considered for this numerical validation are: dimensionless inlet velocity, $u_{in} = 0.1$, $t_p = 0.1$, $\kappa_p = 10$, $\kappa = 15$, $\mathrm{Pe} = 500$ and $F_d = 10$. (b) Represents the validation of dimensionless species concentration with limiting Newtonian fluid (n = 1) case at the outlet of the electroosmotic micromixer with the experimental result by Biddiss et al., (2004). The other parameters considered for this experimental validation are: $\mu_\infty^* = 0$, $\mu_0^* = 0.001$ Pa-s, $\rho = 1000\ \mathrm{kg/m^3}$, $D = 4.37\times10^{-10}\ \mathrm{m^2 s^{-1}}$, $E = 280\ \mathrm{V/cm}$ and $70\ \mathrm{V/cm}$. (c) Represents the experimental results by Stroock et al., (2000) (right side) validated with present work (left side) of electroosmotic vortices limiting to Newtonian fluid (n = 1). The other parameters considered for this experimental validation (limiting case) are: $u_{in} = 0.025$, $\kappa = 250$, electroosmotic mobility, $\mu_{eo} = \varepsilon_r \varepsilon_0 \Psi_{ref}^* / \mu_0^*$ = 1.9 $(\mu\mathrm{m/s})/(\mathrm{V/cm})$ and $E^* = 95\ \mathrm{V/cm}$.

Further, to establish the credibility of present modelling framework, we conducted a comparative analysis of our results with the existing numerical data and experimental observations, as depicted in Fig. 5.3(a) and (b) respectively. Specifically, we compared the dimensionless species concentration field obtained at the section (x = 5) of the chosen micromixer with the numerical results (Gaikwad et al., 2020) for limiting case (n = 1), as illustrated in Fig. 5.3(a). The other parameters considered for this validation are: $u_{in} = 0.1$, $d_p = 0.1$, $\kappa_p = 10$, $\kappa = 15$, $F_d = 10$, and $\mathrm{Pe} = 500$. Additionally, the same dimensionless species concentration profile is compared with the experimental findings of Biddiss et al., (2004) as depicted in Fig. 5.3(b). This comparison is shown for two distinct electric field strengths, namely 280 V/cm and 70 V/cm, for the limiting to Newtonian fluid case (n = 1). The specific parameters considered for this experimental validation include a solution molarity of 25 mM, $\mu_\infty^* = 0$, $\mu_o^* = 0.001$ Pa-s, $\rho = 1000\ \mathrm{kg/m^3}$, $D = 4.37\times10^{-10}\ \mathrm{m^2 s^{-1}}$ and the zeta potential is set to yield an electroosmotic mobility $= -5.9\times10^{-8}\ \mathrm{m^2/(V\text{-}s)}$. It may be mentioned here that electroosmotic vortex/vortices formed pertaining to the present flow configuration is the instrumental to yield augmented solute mixing. Considering the crucial role of electroosmotic vortex/vortices in the underlying mixing strength, we undertook an attempt in Fig. 5.3(c) to compare the constitutive structure of electroosmotic vortex/vortices based on current results (left side) with the experimental data (right side) of Stroock et al., (2000) for a Newtonian fluid (n = 1). The validation is carried out in the y-z plane at x ~ 0 μm, with a focus on underlying transportation primarily due to electroosmotic effect. We consider non-uniform surface charge by patterning the bottom all with negative and positive zeta potentials at the first and second halves along the axial length. The purpose of this arrangement is to produce electroosmotic vortices under the application of a uniform axial electric field (E^*). For this comparison, we consider the magnitude of applied electric field strength E^* = 95 V/cm and magnitude of electroosmotic mobility of the charged surface 1.9 $(\mu\mathrm{m/s})/(\mathrm{V/cm})$ in the limit of thin double layer. The measured value of the vortex strength based on the experimental data (1.805×10^{-4} m/s) approximately aligns with the result obtained from the present study (1.737×10^{-4} m/s) for the limiting case of Newtonian fluid (n = 1). It is worth mentioning here that for this endeavour, we considered necessary assumptions in formulating the mathematical model to mimic the experimental phenomenon.

5.3 Range of model parameters

In the present study, we have considered micromixer height, $2H$ = 20 μm; reference external electric field, E_{ref}^* = 10^4 V/m and reference EDL potential, Ψ_{ref}^* = 25 mV when T = 298 K (Gaikwad et al., 2020; Mehta and Mondal, 2023). The value of

$\varpi\left(=\Phi^*_{ref}/\Psi^*_{ref}\right)$ for the chosen value of Ψ^*_{ref} and E^*_{ref} is calculated as 4. The dimensionless patch thickness ($t_p = t^*_p/H$) and length ($L_p = L^*_p/H$) are considered as 0.2 and 1.0, respectively, which is equivalent to t^*_p = 2 μm and L^*_p = 10 μm (Biesalski and Rühe, 1999; Dubas and Schlenoff, 2001). Note that the chosen dimensions of the proposed fluidic configuration/micromixer are in compliance with the experimental setup. It is important to mention here that the time parameter of the Carreau model (λ) remains nearly constant across a range of hematocrit levels, specifically within the range of 5 to 15% for the separated plasma (95% water) and red blood cell (RBC) mixture, as well as for the pure blood sample with a hematocrit level of 45%. Consequently, for the present analysis, the value of λ is set at 3.313 s. To capture the shear-thinning characteristics of the fluid, the flow-behavior index (n) is varied within the range of 0.35 to 0.75 (Mehri et al., 2018; Mehta et al., 2021). The ratio of infinite to zero shear rate viscosity, μ^*_∞/μ^*_0 is held constant throughout the present study and considered as $\mu^*_\infty/\mu^*_0 = 0.0616$. Furthermore, generally, the range of zero shear rate viscosity (μ^*_0) varies from 23.33 to 139.3 mPa-s when hematocrit levels range from 5 to 15% of blood (Mehri et al., 2018; Mehta et al., 2021). Consequently, the order of the Helmholtz–Smoluchowski velocity (u^*_{HS}) become $10^{-6} \sim 10^{-5}$ m/s for $\varepsilon_r = 80$ and the specified values of H, Ψ^*_{ref}, and E^*_{ref} mentioned before. For the calculated range of u^*_{HS} and the value of λ mentioned before, the Carreau number (Cu) can be obtained be in the range of 10^{-3} to 10^{-1}, and the same range has been considered in the present analysis (Mehta and Mondal, 2023). Considering the range of species diffusion coefficient range as 10^{-11} to 10^{-12} m^2s^{-1} typical to samples used in biomedical applications, the diffusive Peclet number range, based on the mentioned value of H and range of u^*_{HS}, range from 10^0 to 10^3 (Gaikwad et al., 2020; Mehta et al., 2022; Mehta and Pati, 2022; Mehta and Mondal, 2023).

5.4 Results and discussion

In this endeavor, we take an effort to investigate the following: the modulation in space charge density of the polyelectrolyte layer (PEL), net electrical body force, streamlines, flow pattern regimes, mixing efficiency, and flow rates for a change in pH of the bulk solution (pH_b) from acidic to basic range; diffusive Peclet number (Pe) of species; Carreau number (*Cu*) and flow behavior index (*n*).

5.4.1 PEL space charge density and body force

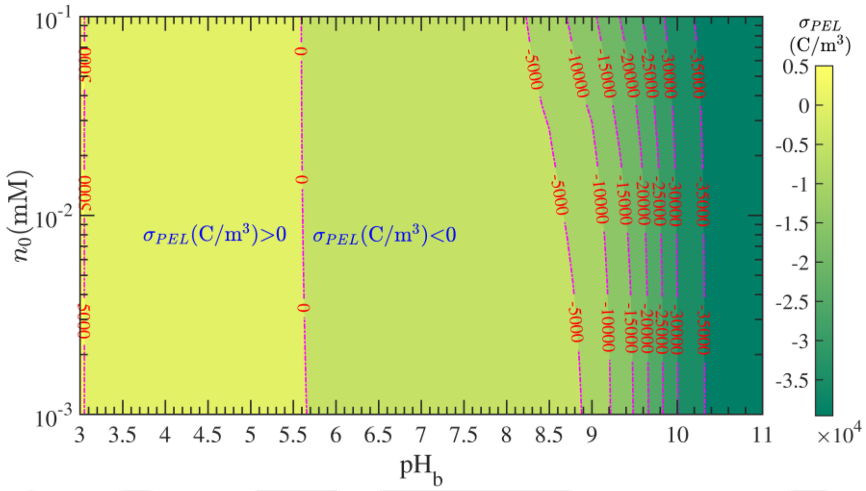

Figure 5.4: Contour of the space charge density in the plane of pH_b and n_0 when patch thickness, $t_p^* = 0.2H$ and patch length, $L_p^* = H$.

We have mentioned before that the PEL charge group is extremely sensitive to protonic exchange. Therefore, as can be seen from Eq. (5.1), the space charge density of PEL (σ_{PEL}) is greatly impacted by the solution bulk pH (pH_b) or the local concentration of H^+ ions. In light of this, Fig. 5.4 shows the contour of space charge density in the plane of pH_b and bulk ionic concentration (n_0). It is observed that, in highly acidic solutions (pH_b ~ 3), the space charge density is positive. This finding can be explained by the first positive term in Eq. (5.1), which is having a greater dominance than the second negative term for the highly acidic solution. Consideration of reaction constants as $K_A = 10^{-2.2}$ M and $K_B = 10^{-9}$ M, for PEL acidic and basic functional group protonic exchange respectively, permits a higher magnitude of H^+/K_A as compared to K_B/H^+ . On the contrary, we obtain a negative space charge density at higher values of pH_b for the set of K_A and K_B considered, attributed to dominating effect of second negative term over the first positive term in Eq. (5.1) for a basic solution. Accordingly, the order of K_B/H^+ (~10^2) is found to be extremely high as compared to the order of H^+/K_A (~10^{-9}) in Eq. (5.1) for very high solution bulk pH (pH_b ~ 11). Consequently, for the higher pH_b values, the second term of Eq. (5.1) will dominate.

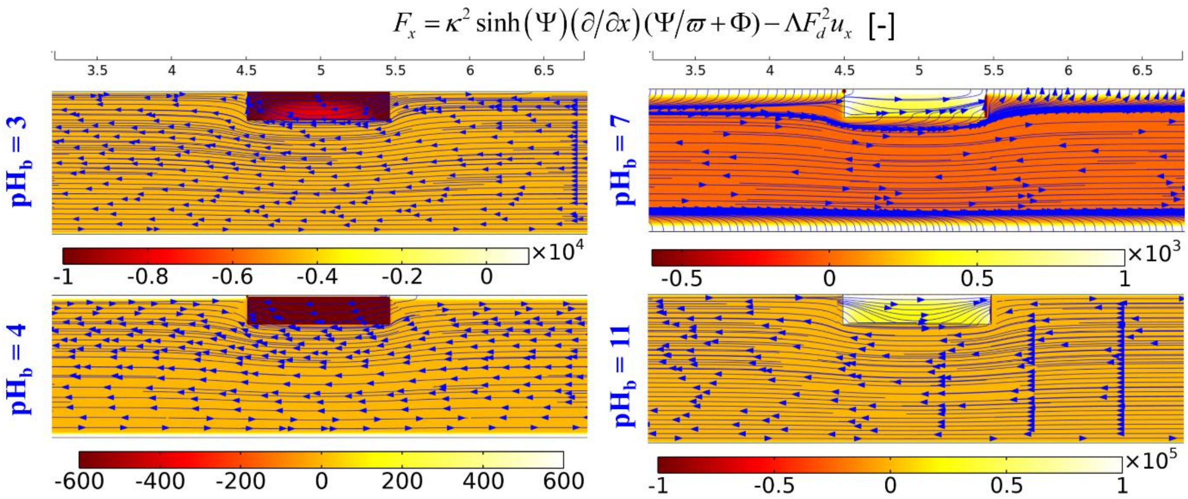

Figure 5.5: Contours of dimensionless electrical body force lines and its axial component ($F_x = \kappa^2 \sinh(\Psi)(\partial/\partial x)(\Psi/\varpi + \Phi) - \Lambda F_d^2 u_x$) intensity by varying the solution bulk pH (pH$_b$) when $Cu = 0.02$, $n = 0.55$, $n_0 = 10^{-5}\,\mathrm{M}$.

We next delve into the magnitude of net body force acting on the fluid mass for different solution bulk pH (pH$_b$). This endeavour will help to physically explain the related flow field, as demonstrated graphically in Fig. 5.5, that is generated by electroosmotic actuation. Figure 5.5 plots the contour of axial component of body force ($F_x = \kappa^2 \sinh(\Psi)(\partial/\partial x)(\Psi/\varpi + \Phi) - \Lambda F_d^2 u_x$) and lines of the net body force (see right side of Eq. 5.6) for different values of pH$_b$. The body force lines are mostly oriented from right to left for the lower pH$_b$ values (= 3 and 4). It is explained by the existence of applied potential field's negative gradient, i.e., negative magnitude of $\partial\Phi/\partial x$, when higher potential is applied to the left-side of the microchannel. Remarkably, within the PEL, the axial body force component has a larger negative magnitude. This observation is attributed to decreased electrical permittivity of PEL. The decreased electrical permittivity of PEL allows the electric field lines within it to pass through less electrically resistive medium. Because of this, the larger negative magnitude of applied electric field strength is predicted inside the PEL. Therefore, at lower pH$_b$, the higher negative axial electric field component is predicted inside the PEL due to the underlying phenomenon mentioned above. Furthermore, the body force lines inside the PEL are directed from left to right side for the higher values of pH$_b$ (= 7 and 11). This observation can be explained by the protonic exchange at higher pH$_b$. Note that the protonic exchange at higher pH$_b$ results in a stronger negative intensity of space charge density inside the PEL, as illustrated in Fig. 5.4. It is because of the reason more mobile cations are drawn into the highly negatively charged PEL group inside the PEL. Consequently, those inducted cations are electrically pushed towards the right side inside the PEL and away from the left positive electrode.

5.4.2 Effect of pH$_b$ on the flow field and associated regime

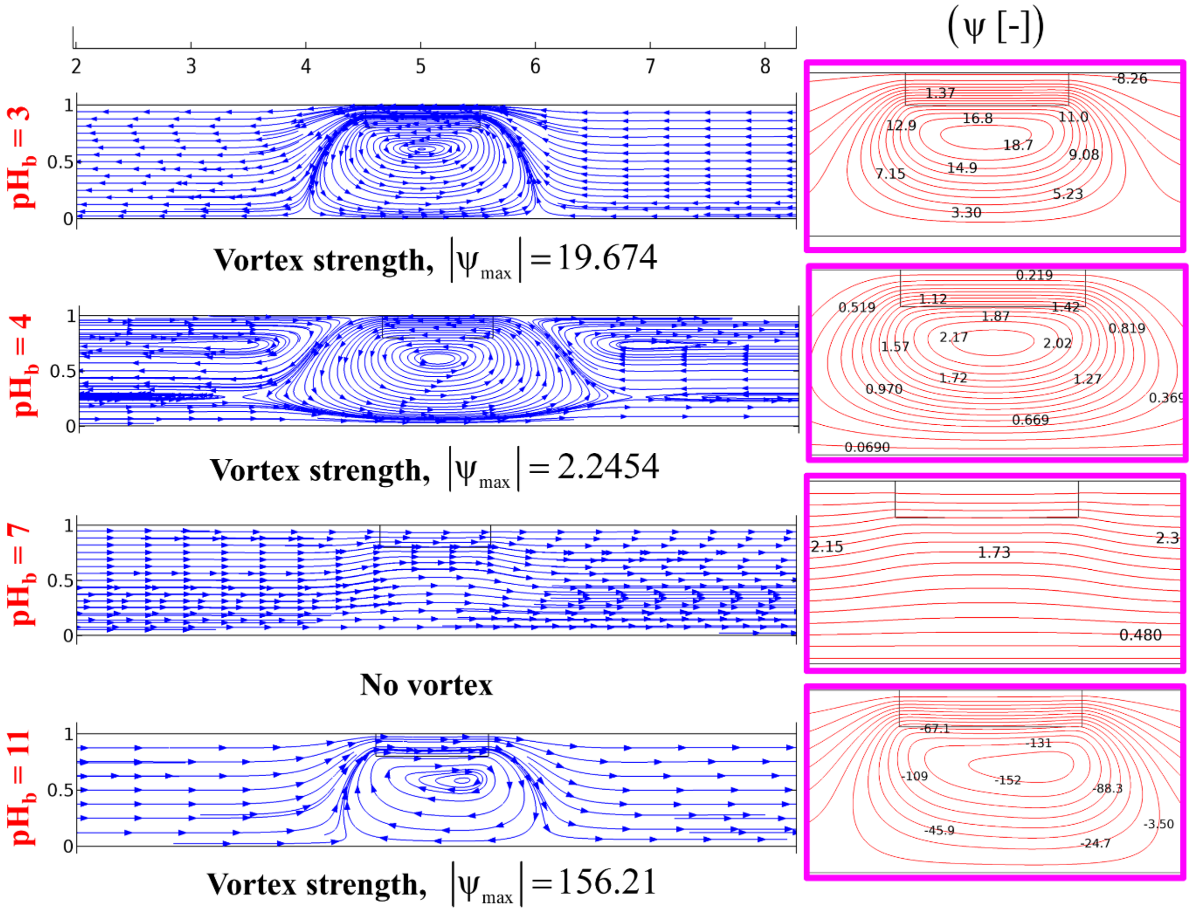

Figure 5.6: Contours of dimensionless flow velocity with streamlines and vortex strength along the flow direction by varying the solution bulk pH (pH$_b$) when $Cu = 0.02$, $n = 0.55$ and $n_0 = 10^{-5}$ M
.

We undertake an effort, in Fig. 5.6, to illustrate the electroosmotic flow field developed in the fluidic channel by varying the bulk solution pH (pH$_b$). In addition, by solving Poisson's equation for the stream function, which is given as $\nabla^2\psi = \left(\partial u_x/\partial y - \partial u_y/\partial x\right)$, the dimensionless magnitude of vortex strength $\left(|\psi_{\max}|\right)$ is also demonstrated in Fig. 5.6. Here, ψ stands for the dimensionless stream function normalised by the scale $u_{HS}^{*}H$. The solution of this equation is involved with the following conditions: setting $\psi = 0$ at the wall, and no-slip condition, which ensures zero flow rate per unit width close to the wall. For pH$_b$ = 3, we observe onset of bulk flow from right to left, leading to formation of a counterclockwise vortex adjacent to PEL (see

Fig. 5.5). This phenomenon can be explained by the following physical justifications. The direction of net body force acting on the fluid mass is from right to left for $pH_b = 3$, as illustrated in Fig. 5, triggering the underlying flow to take place in that direction. Notably, intensity of negative body force is higher inside the PEL for $pH_b = 3$, developing a stronger electrical forcing from right to left within the fluid mass inside the PEL. This amplified negative flow velocity inside the PEL, coupled with a relatively lower magnitude of electrical forcing in the clear region below the PEL, results in a substantial momentum difference between the prevailing flow in PEL and that in the clear region (below PEL). Consequently, this interplay of forces leads to the formation of counterclockwise vortex observed beneath the PEL during bulk fluid flow from the channel's right to left. Due to a substantial momentum loss of the underlying flow below the PEL region, the flow gets reversed to maintain mass continuity. Specifically, at $pH_b = 4$, a notable reduction in the magnitude of net body force within the clear region, compared to the PEL region (see Fig. 5.5), facilitates generation of intensified momentum differences over a larger region. Consequently, the vortex size at the PEL becomes significant at $pH_b = 4$, impeding the primary flow on both sides of it and leads to the formation of additional recirculation zones. For $pH_b = 7$, the flow is directed from left to right owing to the dominance of net body force in the same direction as illustrated in Fig. 5.5. For extremely high solution bulk pH ($pH_b = 11$), a clockwise vortex is formed below the PEL. This is attributed to a higher positive net body force within the PEL, developing a substantial momentum difference between the PEL and clear regions. Subsequently, the flow reverses in the opposite direction, resulting in a clockwise vortex generation. Notably, the vortex strength is positive for $pH_b = 3$ and 4, indicating counterclockwise vortex formation, and negative for $pH_b = 11$, indicative of clockwise vortex formation. It is crucial to highlight that the magnitude of vortex strength is notably higher at $pH_b = 11$, owing to a higher net body force within the PEL, as depicted in Fig. 5.5.

In the previous discussion, we explored how local modulation of electrical body force leads to diverse flow field topologies with a change in pH_b. Consequently, the anticipated flow patterns are influenced by the variations in pH_b and rheological parameters, namely *Cu* and *n*, as illustrated in Figs. 5.7(a) and 5.7(b) respectively. The distinct flow pattern regimes can be classified as follows: bottom recirculation (Type I),

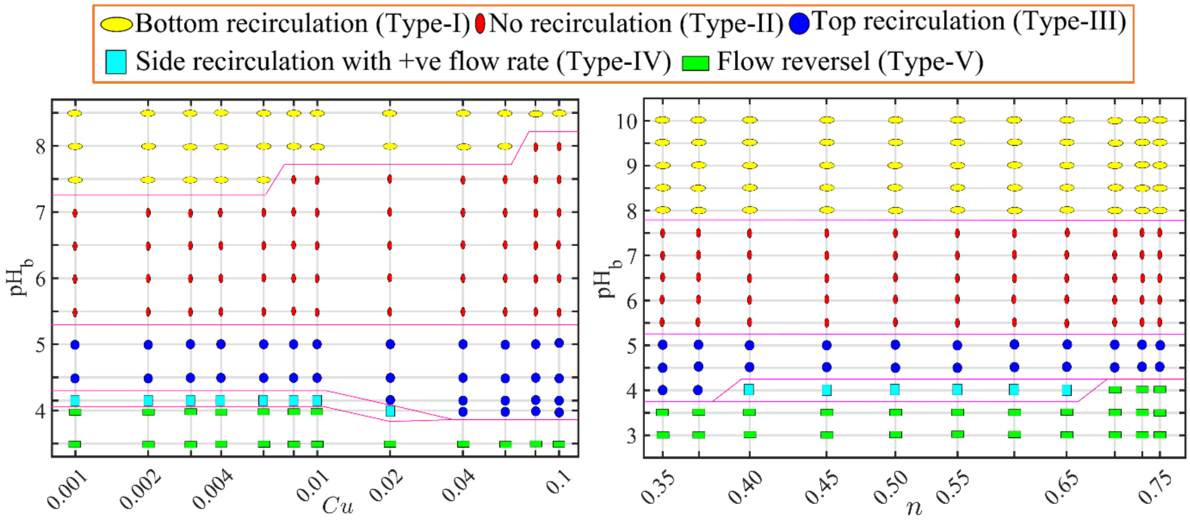

(a) (b)

Figure 5.7: Phase diagram of flow structure regimes (a) in the plane of Carreau number (*Cu*) and solution bulk pH (pH$_b$) when n = 0.55 and (b) in the plane of flow-behaviour index (n) and solution bulk pH (pH$_b$) when $Cu = 0.02$ The other values of parameters considered for this analysis are: patch thickness $t_p^* = 0.2H^*$, patch length $L_p^* = H^*$ and bulk concentration, $n_0 = 10^{-5}\,\mathrm{M}$
.

- no-recirculation (Type II), top recirculation (Type III), side recirculation with positive flow rate (Type IV), and flow reversal (Type V). Nota that type I regime, indicating bottom recirculation, is prominent at higher pH$_b$ values. Additionally, the thickness of this region on pH$_b$ axis shrinkages with increasing the value of *Cu*. This observation is attributed to a reduction in flow resistance because of the enhanced shear-thinning behaviour of the fluid with increased *Cu*. This reduction in flow resistance with higher *Cu* allows for an increase in primary flow strength, leading to a lesser momentum loss and preventing vortex formation at the bottom wall over some larger pH$_b$ range. Similarly, the increased primary flow strength for higher *Cu* results in narrower flow regimes, referred to as type V regime. It is because of this reason; we do not find type IV flow regime for higher values of *Cu* as witnessed in Fig. 5.7(a). This implies that reversal of net flow rate occurs quickly at higher *Cu* values, particularly with a decrease in pH$_b$ range between type III and type V regimes. Furthermore, the impact of the flow behavior index (n) on these flow pattern regimes is shown in Fig. 5.7(b). It is seen from Fig. 5.7(b) that the value of n has minuscule effect on the flow regime except for smaller pH$_b$ values. It is evident that a narrower region of the type V regime is observed for lower n values at smaller pH$_b$. This observation is once again attributed to the reduced flow resistance owing to a lesser apparent viscosity of the fluid for smaller n values. Consequently, the combination of stronger primary flow velocity and weaker momentum loss enables the generation of a narrower pH_b range for type V flow regime at smaller *n*. Notably, occurrence of type IV flow regime (side recirculation with positive flow rate) is anticipated when both primary and secondary flows demonstrate almost a comparable strength. In instances of smaller values of *n*, the primary flow tends to be stronger due to the lower apparent viscosity. Conversely, at higher *n* values, the increased apparent viscosity leads to more substantial momentum loss and simultaneously results in an intensified reverse flow. Subsequently, type IV flow pattern is not predicted for either higher or lower values of *n*, as illustrated in Fig. 5.7(b).

5.4.3 Mixing efficiency and flow rate

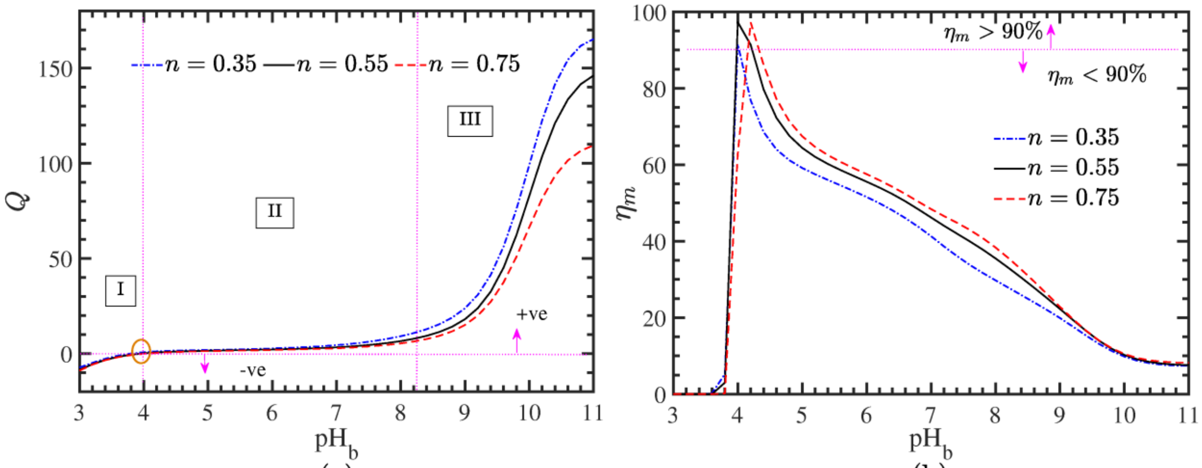

(a)
(b)

Figure 5.8: Plot of (a) dimensionless flow rate with three regime and (b) mixing efficiency by varying the solution bulk pH (pH_b) at Peclet number, Pe = 100 when *Cu* = 0.02, $n_0 = 10^{-5}\,\text{M}$, and flow-behaviour index, *n* = 0.35, 0.55, 0.75.

The net mass flow rate generated by electroosmotic flow can be expressed in terms of the dimensionless flow rate, *Q*. The variation of the *Q* with pH_b is illustrated in Fig. 5.8(a), obtained considering different flow behaviour indices (*n*). Notably, the dimensionless flow rate exhibits a negative value for very low pH_b values in regime I. This negative flow rate is attributed to the primary flow direction from right to left of the channel in highly acidic solutions, as depicted in Fig. 5.6. In regime II, the dimensionless flow rate is observed to be very small. This phenomenon is attributed to a weak strength of the electrical body force in regime II, as evidenced in Fig. 5.5, stemming from the weaker magnitude of the PEL space charge density (as illustrated in Fig. 5.4). Consequently, this weak body force leads to a very low flow rate and, correspondingly, a diminutive dimensionless flow rate in regime II is witnessed. Moreover, the higher values of $\mathrm{pH_b}$ in regime III leads to a substantial increase in the dimensionless flow rate. The prominent augmentation in electrical body force at higher $\mathrm{pH_b}$, as depicted in Fig. 5.5, significantly amplifies the flow strength. This enhancement plays a pivotal role in triggering the dimensionless flow velocity, especially with an increase in $\mathrm{pH_b}$ value in its higher range considered in this endeavour. Note that an increase in the value of n contributes to a reduction in the dimensionless flow velocity, particularly for higher $\mathrm{pH_b}$ values. The increase in apparent viscosity associated with higher values of n introduces a higher flow resistance. Subsequently, the enhanced flow resistance at higher n values predicts a lower dimensionless flow velocity.

Now, referring to Fig. 5.1, where the upper part of the inlet represents injection of pure liquid and the bottom part involves liquid with species, grafted PEL modulated electroosmotic flow initiates mixing of species within the system. Hence, the variation of mixing efficiency (η_m) versus $\mathrm{pH_b}$ is illustrated in Fig. 5.8(b), considering changes in the flow behaviour index (n). It is observed that η_m is close to zero for highly acidic solutions ($\mathrm{pH_b} \sim 3$). This is attributed to the negative flow rate, as can be seen in Fig. 5.8(a), which inhibits the species transport into the domain for mixing with the pure liquid. Interestingly, a sharp increase in η_m is predicted at around $\mathrm{pH_b} \sim 4$, reaching a value exceeding 90%. This observation is attributed to the generation of multiple recirculation zones in the chosen fluidic pathway at that $\mathrm{pH_b}$ value, corresponding to regime IV (side recirculation with positive flow rate). Consequently, these multiple recirculation zones contribute to a stronger convective mixing strength, as supported by η_m exceeding 90%. Furthermore, an increase in flow rate with higher $\mathrm{pH_b}$ (as shown in Fig. 5.8(a)) leads to a reduction in the mixing efficiency η_m. The augmented flow rate at higher $\mathrm{pH_b}$ substantially decreases average residual time of the species. Therefore, a less uniform ($C \sim 0.5$) concentration field at the outlet is predicted for larger $\mathrm{pH_b}$ values, which in turn, results in a reduction of η_m. On the other hand, the reduction in flow rate with increasing n (as depicted in Fig. 5.8a) extends the residual time of the species. Notably, a more uniform concentration field ($C \sim 0.5$) at the outlet for higher n values offers higher mixing efficiency, as illustrated in Fig. 5.8(b).

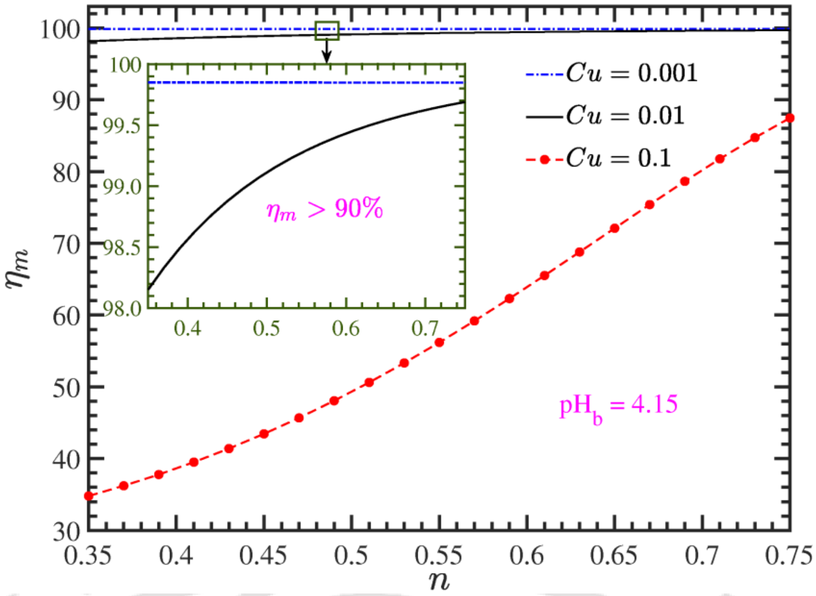

Figure 5.9: Plot of mixing efficiency by varying the flow-behaviour index (*n*) at different Carreau number, *Cu* (= 0.001, 0.01, 0.1) at bulk solution pH, $\mathrm{pH_b} = 4.15$, bulk concentration, $n_0 = 10^{-5}\,\mathrm{M}$ and Peclet number, Pe = 100.

As discussed before, the maximum efficiency is observed when the solution bulk pH ($\mathrm{pH_b}$) is approximately close to 4. To explore more into this aspect, we have depicted in Fig. 5.9 the variation of mixing efficiency (η_m) with the flow behavior index (*n*) for different Carreau numbers (*Cu*), specifically when $\mathrm{pH_b}$ is close to 4 ($\mathrm{pH_b} = 4.15$). In this analysis, it is evident that the value of η_m becomes greater than 90% and approaches 100% (see the inset of Fig. 5.9) for smaller values of the Carreau number (*Cu* = 0.001 and 0.01) for all values of *n* considered. This observation suggests that fluids with both lower and higher values of *n* consistently predict very high η_m for *Cu* in the range of 0.001 to 0.01, while keeping the velocity scale constant for a given potential difference and $\mathrm{pH_b}$ close to 4. Moreover, an increase in the value of *n* for higher values of *Cu* results in an enhancement of η_m. This can be attributed to the reduction in primary flow velocity, allowing for a more uniform species concentration field (*C* ~ 0.5) at the outlet for higher *n* value due to the increase in average residual time. However, it is noted that η_m is less than 90% when *Cu* is set to 0.1. This observation is attributed to the reduced residual time because of stronger primary velocity attained for *Cu* = 0.1.

The species diffusion coefficient plays a crucial role in determining the mixing characteristics of a given species. In Fig. 5.10, the contour of η_m is presented on the Pe - $\mathrm{pH_b}$ plane, showcasing the variation in the species diffusion coefficient by changing a diffusive Peclet number in the range of 10^0 to 10^3. The depicted trend reveals that a decrease in the species diffusion coefficient, (equivalently increase in Peclet number), leads to a consistent decrease in η_m for all pH$_b$ values. This behaviour is attributed to the reduction in the diffusion coefficient, which in turn, curtails the residual time of the species in the pathway. Consequently, this reduction promotes uniformity in species concentration (C ~ 0.5) at the outlet. Notably, we have identified a distinct locus on the Pe - pH$_b$ plane where η_m exceeds 90%, depicted by the projected arrow lines in Fig. 5.10. Furthermore, it is observed that pertaining to a highly acidic solution, η_m approaches 90% even at higher Peclet numbers. This phenomenon is explained by the presence of multiple recirculation zones developed in the fluidic pathway, facilitating a stronger species mixing as witnessed by a higher η_m in Fig. 5.10. In summary, it can be inferred that acidic solutions exhibit a higher potential to attain higher η_m, particularly at higher diffusive Peclet numbers where convective mixing indeed poses a challenge.

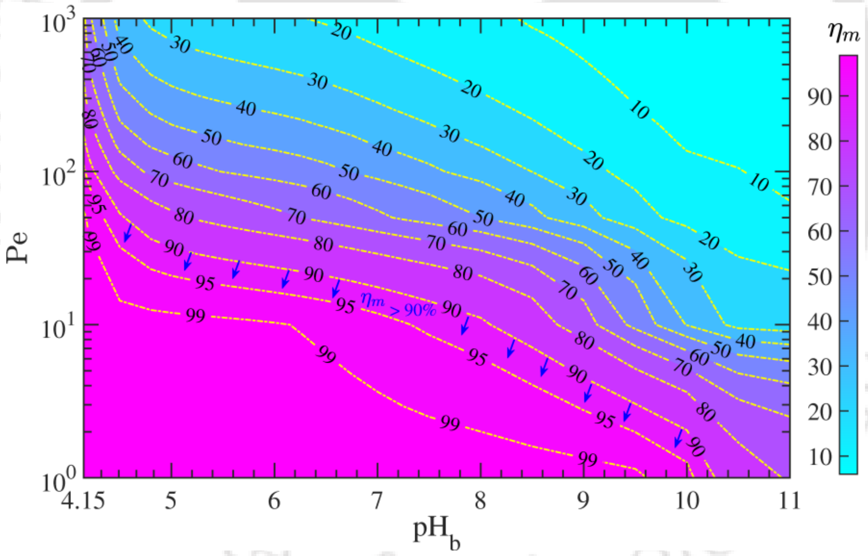

Figure 5.10: Surface plot of mixing efficiency in the plane of Peclet number and bulk solution pH (pH$_b$). The other values of parameters considered for this analysis are: Cu = 0.02, n = 0.55, $n_0 = 10^{-5}\,\mathrm{M}$.

5.5 Summary

In this study, we delve into the characteristics of electroosmotic flow and species mixing in soft microchannels with polyelectrolyte grafts, focusing on non-Newtonian fluids. The interplay among charged surfaces, polyelectrolyte groups, and mobile electrolytes results in the formation of an electrical double layer (EDL) at the interface with the electrolytic liquid. The study considers the influence of protonic exchange with polyelectrolyte groups, along with the pH and ionic concentration-dependent zeta potential. A mathematical framework, employing a finite element method, is developed to estimate the external potential field, EDL potential field, flow field, and species concentration. Validation of the numerical model is carried out using existing experimental data, benchmarking the estimated species concentration field under electroosmotic actuation and vortex formation in the presence of non-uniform surface charge. The investigation explores variations in the space charge density of the polyelectrolyte layer (PEL), net electrical body force, mixing efficiency, and flow rates by altering the bulk solution pH (pH_b) across acidic to basic ranges. Additionally, the study analyzes the impact of diffusive Peclet number, Carreau number, and flow behavior index. The research reveals that protonic exchange between basic and acidic polyelectrolyte groups is significantly influenced by the bulk pH of the solution, leading to changes in the pH-sensitive PEL space charge density. This, in turn, affects the net electrical body force in the PEL, influencing both direction and magnitude, ultimately resulting in distinct flow patterns based on the solution's bulk pH. Five distinct flow patterns are identified, ranging from bottom recirculation to flow reversal, with a strong correlation to the Carreau number. Notably, the study demonstrates that optimal mixing efficiency and positive flow rates are achievable when the bulk pH of the solution is around 4, particularly at lower Carreau numbers. In conclusion, this research yields valuable insights for the design of microfluidic devices intended for mixing and transporting liquids with specific pH_b values and non-Newtonian behavior.

Chapter 6

Epilogue

In this dissertation, we have conducted a comprehensive exploration of selected challenges aimed at achieving effective and efficient mixing in narrow fluidic channels. Our approach encompasses both passive and active methods, specifically investigating the influence of swirl flow and electroosmotic flow. Chapters 2-5 have delved into the mathematical modelling, solution procedures, and results of each problem in detail. As a culmination of our research, this final chapter serves as an epilogue, summarizing our findings and drawing inferences from the various analyses conducted throughout the dissertation.

This dissertation delves into the microfluidic applications concerning biofluid transport and mixing within narrow fluidic assays. It concentrates on two distinct approaches: passive mixing, considering the influence of inlet swirl on both Newtonian and non-Newtonian fluid flow, and active mixing, which incorporates a grafted soft polyelectrolyte layer (PEL) and pH-dependent polyelectrolyte layer. The pH-dependent PEL is characterized by a space charge density influenced by the non-trivial electroosmotic effect and the solution bulk pH (pH_b). These considerations could bring about a paradigm shift in the design aspects of micro/nanofluidic systems. Notably, a persistent challenge faced by researchers is achieving efficient mixing in a microchannel within a limited space, necessitating the incorporation of secondary flows to enhance advection strength over molecular diffusion. These identified gaps and challenges serve as compelling justifications for further exploration in this specific research domain. The dissertation is structured around four distinct problems, each accompanied by mathematical modelling, solution procedures, and results, providing insights into the intricacies of these microfluidic phenomena.

- *Effective solute mixing of a Newtonian fluid within a cylindrical narrow fluidic channel, specifically in the presence of an inlet swirl.*
- *Effective solute mixing of a non-Newtonian fluid within a cylindrical narrow fluidic channel, specifically in the presence of an inlet swirl.*

- *Effective solute mixing of non-Newtonian fluid through the modulation of electroosmotic vortices using a soft polyelectrolyte layer*.
- *Effective solute mixing of non-Newtonian fluid through the modulation of electroosmotic vortices using a pH-dependent soft polyelectrolyte layer*.

A brief summary of our findings and the inferences obtained from these analyses are presented as follows.

In **Chapter 2**, we have described a novel method for efficient vortex-induced mixing in a narrow cylindrical fluidic channel, emphasizing the impact of inlet swirl on convection under laminar flow conditions. Analytical derivation of the swirl velocity profile reveals its role in rotating the fluid tangentially, promoting vortex formation for enhanced mixing. The study explores the influence of Reynolds and Peclet numbers, demonstrating that at lower Reynolds numbers ($Re \leq 10$), molecular diffusion dominates mixing, while chaotic convection becomes significant at higher Reynolds numbers ($Re > 10$). Also, we demonstrate that for $Re \geq 25$, the role of molecular diffusion becomes insignificant on the mixing because of the lesser residence time of the constituent fluids. Increased Reynolds numbers amplify swirl magnitude, reducing the role of molecular diffusion. The addition of swirl velocity proves effective in achieving efficient mixing even after complete swirl decay, significantly reducing the required length of the fluidic configuration. Overall, the insights gained contribute to understanding vortex-assisted mixing in microfluidic systems.

In **Chapter 3**, we extend the first investigation by extending it to encompass non-Newtonian fluids. Here, we propose a novel method to achieve efficient vortex-induced mixing of non-Newtonian fluids within a confined narrow cylindrical channel. The emphasis is on understanding the impact of inlet swirl flow on convection under laminar flow conditions. By incorporating analytically derived swirl and axial velocities into the species transport equation, we determine the concentration distribution of the constituent fluids/solutes across the chosen fluidic configuration. Results show that an increased power-law index leads to higher apparent viscosity, affecting swirl decay length and reducing axial and tangential velocities. It is demonstrated that decreasing the value of transition radius and increasing the magnitude of Reynolds number leads to an enhancement of swirl intensity to act over a greater extent of the flow configuration, attributed primarily to the combined effects of higher value of radial pressure gradient and reduced wall shear stress. The study explores the influence of Reynolds and power-law index (= 0.8, 1.0 ,1.2), demonstrating that at lower Reynolds numbers ($Re \leq 10$), molecular diffusion dominates mixing, while chaotic convection becomes significant at higher Reynolds numbers ($Re > 10$). Also, through our simulations, we reveal how swirl modifies the flow structure, inducing rotation and increasing the contact surface area of the participating fluids. Our study highlights the significant role of chaotic convection, driven by swirl, in enhancing mixing efficiency at higher Reynolds numbers with increase in the shear thinning nature of fluid Insights gained may benefit researchers aiming to enhance convective mixing using swirl flow, especially by altering rheological properties of base fluids.

In **Chapter 4**, we introduce an innovative approach to achieve efficient mixing within a narrow fluidic channel with patterned-soft layers on the walls, leading to the formation of electroosmotic vortices. The focus of the study was to investigate the combined impact of modulated interfacial electrostatics facilitated by polyelectrolyte layers (PEL) and pressure-driven bulk flow, with the Carreau model employed to characterize the non-Newtonian rheological properties of the solute in a micromixer. The results revealed the generation of vortices at the interface of PEL electrolyte, influenced by the interplay between the inherent fixed charge in the grafted PEL and the external electric field. As the Carreau number increased, indicating shear-thinning behavior, both the strength and size of the vortices (recirculation velocity) at the PEL electrolyte interface are amplified. The analysis emphasized that higher degrees of shear-thinning enhanced convective mixing strength, leading to improved uniformity of species concentration at the micromixer outlet for higher Carreau numbers. The research demonstrated that within the specified Carreau number range, mixing efficiency exceeded 90%, attributed to a decrease in the drag coefficient, a higher normalized PEL Debye-Hückel parameter, along with larger values for normalized PEL patch thickness and length. Additionally, we computed the characteristic time of aggregation kinetics for two-body aggregation under shear rate, a crucial parameter in understanding the impact of induced shear, inherently connected to the underlying mixing, on soft biofluids comprising biomolecules. A notable decrease in the characteristic time of binary aggregation kinetics is anticipated for higher Carreau numbers, primarily attributed to the heightened shear-thinning nature of the fluid. Moreover, an increase in the flow-behavior index prolongs the characteristic time of binary aggregation kinetics for higher Carreau number values.

In **Chapter 5**, we extend the third investigation by introducing a pH-dependent soft PEL structure within the narrow fluidic channel while maintaining the effects of fluid rheology. In this study, we present a novel approach to comprehensively investigate electroosmotic flow and species mixing in soft microchannels grafted with polyelectrolytes, focusing on non-Newtonian fluids. The interplay among the charged surface, polyelectrolyte groups, and mobile electrolyte leads to the creation of electroosmotic vortices and the formation of an electrical double layer (EDL) in contact with the electrolytic liquid. The research delves into the influence of various factors, such as bulk solution pH (pH_b), diffusive Peclet number, Carreau number, and flow behavior index, on the modulation of space charge density in the polyelectrolyte layer (PEL), net electrical body force, mixing efficiency, and flow rates. Notably, the study reveals that changes in pH_b from acidic to basic significantly impact the protonic exchange between acidic and basic polyelectrolyte groups, affecting the pH-sensitive PEL space charge density and, consequently, the net electrical body force in the PEL. The direction and magnitude of the net electrical force are found to be influenced by the bulk pH of the solution, resulting in distinct flow patterns. The study categorizes five distinct flow patterns based on pH_b, ranging from bottom recirculation to flow reversal, and highlights the strong influence of the Carreau number on these patterns. Furthermore, it demonstrates that optimal mixing efficiency, characterized by robust vortices and side recirculation, is possible when the bulk solution pH is approximately 4. This is especially evident in the lower Carreau number range, coupled with positive flow rates.

The analyses presented in this dissertation underscore the transformative potential of both inlet swirl and the polyelectrolyte layer in reshaping contemporary Lab-on-a-Chip (LOC) or micro Total Analysis Systems (μTAS) platforms. Singularly, these factors have the capacity to steer these platforms towards achieving more effective and promising outcomes. The applications discussed herein also pave the way for the development of an entirely new device, with potential utility in in-vitro disease detection. The significance of inlet swirl is particularly valuable for researchers aiming to enhance transport capabilities and convective mixing, especially when manipulating the rheological properties of base fluids, such as water through polymer dilution, to modify their rheological behavior. It is anticipated that the insights gained from these studies will contribute to the enhancement of functionalities, particularly in biological, clinical, and pathological devices, as well as artificial implants. However, for the augmentation of these devices' functionalities through the incorporation of soft polyelectrolyte layers and viscoelastic properties in varying solution pH conditions, the conducted analyses will necessitate the consideration of additional aspects outlined as follows.

Scope of future work**:** In reviewing the various analyses conducted in this thesis, it becomes evident that the objectives outlined for each problem can be expanded through the incorporation of several non-trivial approaches that have not yet been explored. These approaches encompass the utilization of end-charged polyelectrolyte brushes and the consideration of pH-dependent charge density. Specifically, the implementation involves the mixing of fluid components, composed of non-Newtonian fluid, within the context of thermosmotic effects under patch arrangements of polyelectrolyte layers (PEL) to induce a vortex under electroosmotic flow. In consequence, it is also possible to investigate the attainment of vortex-induced mixing by applying an AC electric field that is non-uniformly charged and has a larger zeta potential. Additionally, the investigation may involve pH-dependent PEL and surface charge density in relation to the electroosmotic flow of viscoelastic fluids within a wavy micromixer. Building upon the findings in Chapter 4 and 5, where the influence of a soft polyelectrolyte layer on non-Newtonian mixing dynamics through narrow-fluidic channels was examined, attention can now be turned to considering convective inertia's role in flow dynamics. At sufficiently high Reynolds numbers, the conventional double vortex configuration or dumbbell-shaped vortices may bifurcate into a non-trivial four vortex configuration, potentially impacting mixing performance significantly.

Moreover, exploring vortex-assisted mixing is viable when dealing with the mixing of ferrofluid droplets in a microfluidic channel under the influence of both magnetic and electric fields. This multifaceted approach not only extends the scope of the thesis objectives but also opens avenues for investigating fundamental and intriguing aspects of the underlying mixing phenomena.

REFERENCES

Aboelkassem, Y. (2023) Computational and theoretical model of electro-osmotic flow pumping in a microchannel with squeezing walls. *Physics of Fluids*, 35(5).

Abramowitz, M. and Stengun, I.A. (1968) *Handbook of mathematical functions with formulas, graphs, and mathematical tables*. US Government printing office.

Alekseenko, S.V., Kuibin, P.A., Okulov, V.L. and Shtork, S.I. (1999) Helical vortices in swirl flow. *Journal of Fluid Mechanics*, 382, pp. 195–243.

Alipanah, M., Hatami, M. and Ramiar, A. (2021) Thermal and rheological investigation of non-Newtonian fluids in an induced-charge electroosmotic micromixer. *European Journal of Mechanics - B/Fluids*, 88, pp. 178–190.

Alleborn, N., Nandakumar, K., Raszillier, H. and Durst, F. (1997) Further contributions on the two-dimensional flow in a sudden expansion. *Journal of Fluid Mechanics*, 330, pp. 169–188.

Andrews, L.C. and Phillips, R.L. (2003) *Mathematical techniques for engineers and scientists*. Spie Press.

Ansari, M.A., Kim, K.Y., Anwar, K. and Kim, S.M. (2012) Vortex micro T-mixer with non-aligned inputs. *Chemical Engineering Journal*, 181–182, pp. 846–850.

Ansari, M.A., Kim, K.Y. and Kim, S.M. (2018) Numerical and Experimental Study on Mixing Performances of Simple and Vortex Micro T-Mixers. *Micromachines*, 9(5), p. 204.

Arfken, G.B. and Weber, H.J. (1999) *Mathematical methods for physicists*. American Association of Physics Teachers.

Atencia, J. and Beebe, D.J. (2005) Controlled microfluidic interfaces. *Nature*, 437(7059), pp. 648–655.

Ayinde, T.F. (2010) A generalized relationship for swirl decay in laminar pipe flow. *Sadhana*, 35(2), pp. 129–137.

Azimi, S., Nazari, M. and Daghighi, Y. (2017) Developing a fast and tunable micro-mixer using induced vortices around a conductive flexible link. *Physics of Fluids*, 29(3).

Balasubramaniam, L., Arayanarakool, R., Marshall, S.D., Li, B., Lee, P.S. and Chen, P.C. (2017) Impact of cross-sectional geometry on mixing performance of spiral microfluidic channels characterized by swirling strength of Dean-vortices. *Journal of Micromechanics and Microengineering*, 27(9).

Bali, T. (1998) Modelling of heat transfer and fluid flow for decaying swirl flow in a circular pipe. *International Communications in Heat and Mass Transfer*, 25(3), pp. 349–358.

Banerjee, A., Nayak, A.K., Haque, A. and Weigand, B. (2018) Induced mixing electrokinetics in a charged corrugated nano-channel: towards a controlled ionic transport. *Microfluidics and Nanofluidics*, 22(10), pp. 1–21.

Banerjee, A. and Nayak, A.K. (2019) Influence of varying zeta potential on non-Newtonian flow mixing in a wavy patterned microchannel. *Journal of Non-Newtonian Fluid Mechanics*, 269(April), pp. 17–27.

Banerjee, A., Nayak, A.K. and Weigand, B. (2019) Enhanced mixing and flow reversal in a modulated microchannel. *International Journal of Mechanical Sciences*, 155, pp. 430–439.

Basati, Y., Mohammadipour, O.R. and Niazmand, H. (2019) Numerical investigation and simultaneous optimization of geometry and zeta-potential in electroosmotic mixing flows. *International Journal of Heat and Mass Transfer*, 133, pp. 786–799.

Beebe, D.J., Mensing, G.A. and Walker, G.M. (2002) Physics and Applications of Microfluidics in Biology. *Annual Review of Biomedical Engineering*, 4(1), pp. 261–286.

Biddiss, E., Erickson, D. and Li, D. (2004) Heterogeneous Surface Charge Enhanced Micromixing for Electrokinetic Flows. *Analytical Chemistry*, 76(11), pp. 3208–3213.

Biesalski, M. and Ruhe, J. (1999) Preparation and Characterization of a Polyelectrolyte Monolayer Covalently Attached to a Planar Solid Surface. *Macromolecules*, 32(7), pp. 2309–2316.

Biesalski, M. and Rühe, J. (2000) Swelling of a Polyelectrolyte Brush in Humid Air.

Bird, R.B., Stewart, W.E. and Lightfoot, E.N., (2006) *Transport phenomena*.

Bothe, D., Stemich, C. and Warnecke, H.J. (2006) Fluid mixing in a T-shaped micro-mixer. *Chemical Engineering Science*, 61(9), pp. 2950–2958.

Breidenthal, R. (1981) Structure in turbulent mixing layers and wakes using a chemical reaction. *Journal of Fluid Mechanics*, 109, pp. 1–24.

Brilliantov, N.V., Budkov, Y.A. and Seidel, C. (2016) Generation of mechanical force by grafted polyelectrolytes in an electric field: application to polyelectrolyte-based nano-devices. *Philosophical Transactions of the Royal Society A: Mathematical, Physical and Engineering Sciences*, 374(2080), p. 20160143.

Burns, M.A., Johnson, B.N., Brahmasandra, S.N., Handique, K., Webster, J.R., Krishnan, M., Sammarco, T.S., Man, P.M., Jones, D., Heldsinger, D. and Mastrangelo, C.H. (1998) An Integrated Nanoliter DNA Analysis Device. *Science*, 282(5388), pp. 484–487.

Chang, C.-C. and Yang, R.-J. (2008) Chaotic mixing in a microchannel utilizing periodically switching electro-osmotic recirculating rolls. *Physical Review E*, 77(5), p. 056311.

Chang, H.-C. and Yeo, L. (2010) Electrokinetically driven microfluidics and nanofluidics. *Cambridge university press*.

Chan, S.T., Ault, J.T., Haward, S.J., Meiburg, E. and Shen, A.Q. (2019) Coupling of vortex breakdown and stability in a swirling flow. *Physical Review Fluids*, 4(8), p. 84701.

Chen, Y. and Hsu, J. (2022) Space charge modulation and ion current rectification of a cylindrical nanopore functionalized with polyelectrolyte brushes subject to an applied pH-gradient. *Journal of Colloid and Interface Science*, 605, pp. 571–581.

Chew, Y.T., Xia, H.M. and Shu, C. (2007) Fluid Micromixing Technology and Its Applications for Biological and Chemical Processes. In: *Springer, Berlin, Heidelberg*. pp. 16–20.

Chou, H.P., Spence, C., Scherer, A. and Quake, S. (1999) A microfabricated device for sizing and sorting DNA molecules. *Proceedings of the National Academy of Sciences*, 96(1), pp. 11–13.

Cho, Y.I. and Kensey, K.R. (1991) Effects of the non-Newtonian viscosity of blood on flows in a diseased arterial vessel. Part 1: Steady flows. *Biorheology*, 28(3–4), pp. 241–262.

Cortes-Quiroz, C.A., Azarbadegan, A. and Zangeneh, M. (2010). Characterization and Optimization of a Three-Dimensional T-Type Micromixer for Convective Mixing Enhancement with Reduced Pressure Loss. In *International Conference on Nanochannels, Microchannels, and Minichannels*, 54501, pp. 1357-1364.

Cortes-Quiroz, C.A., Azarbadegan, A. and Zangeneh, M. (2017) Effect of channel aspect ratio of 3-D T-mixer on flow patterns and convective mixing for a wide range of Reynolds number. *Sensors and Actuators, B: Chemical*, 239, pp. 1153–1176.

Cortes-Quiroz, C.A., Azarbadegan, A. and Zangeneh, M. et al. (2014) Evaluation of flow characteristics that give higher mixing performance in the 3-D T-mixer versus the typical T-mixer. *Sensors and Actuators, B: Chemical*, 202, pp. 1209–1219.

Cosentino, A., Madadi, H., Vergara, P., Vecchione, R., Causa, F. and Netti, P.A. (2015) An efficient planar accordion-shaped micromixer: From biochemical mixing to biological application. *Scientific Reports*, 5, pp. 1–10.

Das, S., Banik, M., Chen, G., Sinha, S. and Mukherjee, R. (2015). Polyelectrolyte brushes: theory, modelling, synthesis and applications. *Soft Matter*, 11(44), 8550-8583.

Deen, W.M. (2016) *Introduction to chemical engineering fluid mechanics*. Cambridge University Press.

Demello, A.J. (2006) Control and detection of chemical reactions in microfluidic systems. *Nature*, 442(7101), pp. 394–402.

Dittrich, P.S. and Manz, A. (2006) Lab-on-a-chip: microfluidics in drug discovery. *Nature reviews Drug discovery*, 5(3), pp. 210–218.

Dubas, S.T. and Schienoff, J.B. (2001) Polyelectrolyte multilayers containing a weak polyacid: Construction and deconstruction. *Macromolecules*, 34(11), pp. 3736–3740.

Duffy, D.C., McDonald, J.C., Schueller, O.J. and Whitesides, G.M. (1998) Rapid Prototyping of Microfluidic Systems in Poly(dimethylsiloxane). *Analytical Chemistry*, 70(23), pp. 4974–4984.

Dundi, T.M., Raju, V.R.K. and Chandramohan, V.P. (2021) Numerical evaluation of swirl effect on liquid mixing in a passive T-micromixer. *Australian Journal of Mechanical Engineering*, 19(4), pp. 363–377.

Ebrahimi, S., Hasanzadeh-Barforoushi, A., Nejat, A. and Kowsary, F. (2014) Numerical study of mixing and heat transfer in mixed electroosmotic/pressure driven flow through T-shaped microchannels. *International Journal of Heat and Mass Transfer*, 75, pp. 565–580.

Engler, M., Kockmann, N., Kiefer, T. and Woias, P. (2004) Numerical and experimental investigations on liquid mixing in static micromixers. *Chemical Engineering Journal*, 101(1–3), pp. 315–322.

Gad-el-Hak, M. (1999) The Fluid Mechanics of Microdevices—The Freeman Scholar Lecture. *Journal of Fluids Engineering*, 121(1), pp. 5–33.

Gaikwad, H.S., Kumar, G. and Mondal, P.K. (2020) Efficient electroosmotic mixing in a narrow-fluidic channel: The role of a patterned soft layer. *Soft Matter*, 16(27), pp. 6304–6316.

Grassia, P. (2020) Viscous and electro-osmotic effects upon motion of an oil droplet through a capillary. *Journal of Fluid Mechanics*, 899, p. A31.

Greitzer, E.M., Tan, C.S. and Graf, M.B. (2007) Internal flow: concepts and applications.

Hadigol, M., Nosrati, R., Nourbakhsh, A. and Raisee, M. (2011) Numerical study of electroosmotic micromixing of non-Newtonian fluids. *Journal of Non-Newtonian Fluid Mechanics*, 166(17–18), pp. 965–971.

Haque, A., Nayak, A.K. and Bhattacharyya, S. (2021) Numerical study on ion transport and electro-convective mixing of power-law fluid in a heterogeneous micro-constrained channel. *Physics of Fluids*, 33(12).

Harnett, C.K., Templeton, J., Dunphy-Guzman, K.A., Senousy, Y.M. and Kanouff, M.P. (2008) Model based design of a microfluidic mixer driven by induced charge electroosmosis. *Lab on a Chip*, 8(4), p. 565.

Hay, N. and West, P.D. (1975) Heat Transfer in Free Swirling Flow in a Pipe. *Journal of Heat Transfer*, 97(3), pp. 411–416.

Hessel, V., Löwe, H. and Schönfeld, F. (2005) Micromixers—a review on passive and active mixing principles. *Chemical Engineering Science*, 60(8–9), pp. 2479–2501.

Huang, S.W., Wu, C.Y., Lai, B.H. and Chien, Y.C. (2017) Fluid mixing in a swirl-inducing microchannel with square and T-shaped cross-sections. *Microsystem Technologies*, 23(6), pp. 1971–1981.

Hunter, S.T. (1981) *Zeta Potential in Colloid Science: Principles and Applications*.

Jensen, K. (1998) Smaller, faster chemistry. *Nature*, 393(6687), pp. 735–737.

Jeong, G.S., Chung, S., Kim, C.B. and Lee, S.H. (2010) Applications of micromixing technology. *Analyst*, 135(3), pp. 460–473.

Jin, S.Y., Liu, Y.Z., Wang, W.Z., Cao, Z.M. and Koyama, H.S. (2006) Numerical Evaluation of Two-Fluid Mixing in a Swirl Micro-Mixer. *Journal of Hydrodynamics*, 18(5), pp. 542–546.

Johnston, B.M., Johnston, P.R., Corney, S. and Kilpatrick, D. (2004) Non-Newtonian blood flow in human right coronary arteries: steady state simulations. *Journal of Biomechanics*, 37(5), pp. 709–720.

Kaplan, W. (1981) *Advanced mathematics for engineers*.

Karniadakis, G., Beskok, A. and Aluru, N., (2005). Electroosmotic Flow in Nanochannels. *Microflows and Nanoflows: Fundamentals and Simulation*, pp.447-470.

Kaushik, P., Pati, S., Som, S.K. and Chakraborty, S. (2012) Hydrodynamic Swirl Decay in Microtubes with Interfacial Slip. *Nanoscale and Microscale Thermophysical Engineering*, 16(2), pp. 133–143.

Kaushik, P., Shyam, S. and Mondal, P.K. (2022) Mixing in small scale fluidic systems swayed by rotationality effects. *Physics of Fluids*, 34(6).

Khaydarov, V., Borovinskaya, E.S. and Reschetilowski, W. (2018) Numerical and Experimental Investigations of a Micromixer with Chicane Mixing Geometry. *Applied Sciences*, 8(12), p. 2458.

Kirby, B.J. (2010) Micro- and Nanoscale Fluid Mechanics: Transport in Microfluidic Devices. *Cambridge University Press*.

Kitoh, O. (1991) Experimental study of turbulent swirling flow in a straight pipe. *Journal of Fluid Mechanics*, 225, pp. 445–479.

Kiya, M., Fukusako, S. and Arie, M. (1971) Laminar Swirling Flow in the Entrance Region of a Circular Pipe. *Bulletin of JSME*, 14(73), pp. 659–670.

Kreith, F. and Sonju, O.K. (1965) The decay of a turbulent swirl in a pipe. *Journal of Fluid Mechanics*, 22(2), pp. 257–271.

Krishnaveni, T., Renganathan, T., Picardo, J.R. and Pushpavanam, S. (2017) Numerical study of enhanced mixing in pressure-driven flows in microchannels using a spatially periodic electric field. *Physical Review E*, 96(3), p. 033117.

Kumar, D., Mehta, S.K. and Mondal, P.K. (2023) Enhanced bio-fluids mixing by the soft polyelectrolyte layer-modulated electroosmotic vortices. *Physics of Fluids*, 35(7).

Kumar, D., Shakya, S.M.K. and Kaushik, P. (2020) Inlet swirl decay and mixing in a laminar micro-pipe flow with wall slip. *Physics of Fluids*, 32(2).

Kumar, V., Aggarwal, M. and Nigam, K.D.P. (2006) Mixing in curved tubes. *Chemical Engineering Science*, 61(17), pp. 5742–5753.

Lee, C.Y., Chang, C.L., Wang, Y.N. and Fu, L.M. (2011) Microfluidic Mixing: A Review. *International Journal of Molecular Sciences*, 12(5), pp. 3263–3287.

Li, F., Jian, Y., Xie, Z., Liu, Y. and Liu, Q. (2017) Transient alternating current electroosmotic flow of a Jeffrey fluid through a polyelectrolyte-grafted nanochannel. *RSC Advances*, 7(2), pp. 782–790.

Lobasov, A.S., Shebeleva, A.A., Shebelev, A.V. and Minakov, A.V. (2020) Numerical investigation of the mixing efficiency of fluids in the micromixer with a cylindrical section of a swirl flow. In: *AIP Conference Proceedings*, 2211, p. 080006.

Losey, M.W., Schmidt, M.A. and Jensen, K.F. (2001) Microfabricated Multiphase Packed-Bed Reactors: Characterization of Mass Transfer and Reactions. *Industrial & Engineering Chemistry Research*, 40(12), pp. 2555–2562.

Loucaides, N., Ramos, A. and Georghiou, G.E. (2012) Configurable AC electroosmotic pumping and mixing. *Microelectronic Engineering*, 90, pp. 47–50.

Maddahian, R., Kebriaee, A., Farhanieh, B. and Firoozabadi, B. (2011) Analytical investigation of boundary layer growth and swirl intensity decay rate in a pipe. *Archive of Applied Mechanics*, 81(4), pp. 489–501.

Majhi, M., Nayak, A.K. and Weigand, B. (2023) Electroosmotic mixing of non-Newtonian fluid in an optimized geometry connected with a modulated microchamber. *Physics of Fluids*, 35(3).

Mandal, P.K., Chakravarty, S., Mandal, A. and Amin, N. (2007) Effect of body acceleration on unsteady pulsatile flow of non-newtonian fluid through a stenosed artery. *Applied Mathematics and Computation*, 189(1), pp. 766–779.

Masliyah, J.H. and Bhattacharjee, S. (2006). *Electrokinetic and colloid transport phenomena*. John Wiley & Sons.

Matsunaga, T. and Nishino, K. (2014) Swirl-inducing inlet for passive micromixers. *RSC Advances*, 4(2), pp. 824–829.

Mehri, R., Mavriplis, C. and Fenech, M. (2018) Red blood cell aggregates and their effect on non-Newtonian blood viscosity at low hematocrit in a two-fluid low shear rate microfluidic system. *PLoS ONE*, 13(7).

Mehta, S.K., Mondal, B., Pati, S. and Patowari, P.K. (2022) Enhanced electroosmotic mixing of non-Newtonian fluids in a heterogeneous surface charged micromixer with obstacles. *Colloids and Surfaces A: Physicochemical and Engineering Aspects*, 648, p. 129215.

Mehta, S.K. and Mondal, P.K. (2023) Vortex-assisted electroosmotic mixing of Carreau fluid in a microchannel. *Electrophoresis*, 44(21–22), pp. 1629–1636.

Mehta, S.K. and Pati, S. (2022) Enhanced Electroosmotic Mixing in a Wavy Micromixer Using Surface Charge Heterogeneity. *Industrial and Engineering Chemistry Research*, 61(7), pp. 2904–2914.

Mehta, S.K., Pati, S. and Mondal, P.K. (2021) Numerical study of the vortex-induced electroosmotic mixing of non-Newtonian biofluids in a nonuniformly charged wavy microchannel: Effect of finite ion size. *Electrophoresis*, 42(23), pp. 2498–2510.

Mehta, S.K., Raj, A.R. and Mondal, P.K. (2023) Salinity Gradient-Induced Power Generation in Nanochannels: The Role of pH-Sensitive Polyelectrolyte Layers. *Langmuir*, 39(35), pp. 12302–12312.

Multiphysics, C. O. M. S. O. L. (2015). Version 5.2 [software]. Stockholm, Sweden: COMSOL AB.

Nayak, A.K. (2014) Analysis of mixing for electroosmotic flow in micro/nano channels with heterogeneous surface potential. *International Journal of Heat and Mass Transfer*, 75, pp. 135–144.

Nayak, A.K., Haque, A., Weigand, B. and Wereley, S. (2020) Thermokinetic transport of dilatant/pseudoplastic fluids in a hydrophobic patterned micro-slit. *Physics of Fluids*, 32(7).

Nguyen, N.T. and Wu, Z. (2005) Micromixers—a review. *Journal of Micromechanics and Microengineering*, 15(2), pp. R1–R16.

O'Brien, M.J., Bisong, P., Ista, L.K., Rabinovich, E.M., Garcia, A.L., Sibbett, S.S., Lopez, G.P. and Brueck, S.R.J. (2003) Fabrication of an integrated nanofluidic chip using interferometric lithography. *Journal of Vacuum Science & Technology B: Microelectronics and Nanometer Structures Processing, Measurement, and Phenomena*, 21(6), pp. 2941–2945.

Ottino, J.M. and Wiggins, S. (2004) Introduction: mixing in microfluidics. *Philosophical Transactions of the Royal Society of London. Series A: Mathematical, Physical and Engineering Sciences*, 362(1818), 923-935.

Pacheco, J.R. (2008) Mixing enhancement in electro-osmotic flows via modulation of electric fields. *Physics of Fluids*, 20(9).

Pandey, D., Mondal, P.K. and Wongwises, S. (2022) Chemiosomotic flow in a soft conical nanopore: harvesting enhanced blue energy. *Soft Matter*, 19(6), pp. 1152–1163.

Parcheen, R.R. and Steenbergen, W. (1998) An Experimental and Numerical Study of Turbulent Swirling Pipe Flows. *Journal of Fluids Engineering*, 120(1), pp. 54–61.

Patankar, S. V (1981) A calculation procedure for two-dimensional elliptic situations. *Numerical heat transfer*, 4(4), pp. 409–425.

Patankar, S. V (1980) *Numerical Heat Transfer and Fluid Flow*.

Patel, M., Kruthiventi, S.H. and Kaushik, P. (2020) Rotating electroosmotic flow of power-law fluid through polyelectrolyte grafted microchannel. *Colloids and Surfaces B: Biointerfaces*, 193(May), p. 111058.

Pati S. and Kumar, V. (2019) Effects of temperature-dependent thermo-physical properties on hydrodynamic swirl decay in microtubes. *Proceedings of the Institution of Mechanical Engineers, Part E: Journal of Process Mechanical Engineering*, 233(3), pp. 427–435.

Pati, S., Som, S.K. and Chakraborty, S. (2013) Thermodynamic performance of microscale swirling flows with interfacial slip. *International Journal of Heat and Mass Transfer*, 57(1), pp. 397–401.

Purcell, E.M. (1977) Life at low Reynolds number. *American Journal of Physics*, 45(1), pp. 3–11.

Qian, S. and Bau, H.H. (2002) A Chaotic Electroosmotic Stirrer. *Analytical Chemistry*, 74(15), pp. 3616–3625.

Reader-Harris M.J. (1994) The decay of swirl in a pipe. *International Journal of Heat and Fluid Flow*, 15(3), pp. 212–217.

Rezk, A.R., Qi, A., Friend, J.R., Li, W.H. and Yeo, L.Y. (2012) Uniform mixing in paper-based microfluidic systems using surface acoustic waves. *Lab on a Chip*, 12(4), pp. 773–779.

Sadeghi, M., Saidi, M.H., Moosavi, A. and Sadeghi, A. (2020) Unsteady solute dispersion by electrokinetic flow in a polyelectrolyte layer-grafted rectangular microchannel with wall absorption. *Journal of Fluid Mechanics*, 887, p. A13.

Sammarco, T.S. and Burns, M.A. (1999) Thermocapillary pumping of discrete drops in microfabricated analysis devices. *AIChE Journal*, 45(2), pp. 350–366.

Sánchez, S., Ascanio, G., Méndez, F. and Bautista, O. (2018) Theoretical analysis of non-linear Joule heating effects on an electroosmotic flow with patterned surface charges. *Physics of Fluids*, 30(11).

Sarma, R., Gaikwad, H. and Mondal, P.K. (2017) Effect of Conjugate Heat Transfer on Entropy Generation in Slip-Driven Microflow of Power Law Fluids. *Nanoscale and Microscale Thermophysical Engineering*, 21(1), pp. 26–44.

Shahsavari, S. and Mckinley, G.H. (2015) Mobility of power-law and Carreau fluids through fibrous media. *Physical Review E*, 92(6), p. 063012.

Sheikholeslami, M., Gorji-Bandpy, M. and Ganji, D.D. (2015) Review of heat transfer enhancement methods: Focus on passive methods using swirl flow devices. *Renewable and Sustainable Energy Reviews*, 49, pp. 444–469.

Shit, G.C., Mondal, A., Sinha, A. and Kundu, P.K. (2016) Electro-osmotic flow of power-law fluid and heat transfer in a micro-channel with effects of Joule heating and thermal radiation. *Physica A: Statistical Mechanics and its Applications*, 462, pp. 1040–1057.

Shtern, V. (2018) Cellular Flows: Topological Metamorphoses in Fluid Mechanics. *Cambridge University Press*.

Shyam, S., Mondal, P.K. and Mehta, B. (2021) Magnetofluidic mixing of a ferrofluid droplet under the influence of a time-dependent external field. *Journal of Fluid Mechanics*, 917, p. A15.

Stokes, J.R., Graham, L.J., Lawson, N.J. and Boger, D.V. (2001) Swirling flow of viscoelastic fluids. Part 2. Elastic effects. *Journal of Fluid Mechanics*, 429, pp. 117–153.

Stone, H.A., Stroock, A.D. and Ajdari, A. (2004) Engineering flows in small devices: Microfluidics toward a lab-on-a-chip. *Annual Review of Fluid Mechanics*, 36, pp. 381–411.

Storey, B.D., Edwards, L.R., Kilic, M.S. and Bazant, M.Z. (2008) Steric effects on ac electro-osmosis in dilute electrolytes. *Physical Review E*, 77(3), p. 036317.

Streets, A.M. and Huang, Y. (2013) Chip in a lab: Microfluidics for next generation life science research. *Biomicrofluidics*, 7(1).

Stroock, A.D., Dertinger, S.K., Ajdari, A., Mezic, I., Stone, H.A. and Whitesides, G.M. (2002) Chaotic Mixer for Microchannels. *Science*, 295(5555), pp. 647–651.

Stroock, A.D., Weck, M., Chiu, D.T., Huck, W.T., Kenis, P.J., Ismagilov, R.F. and Whitesides, G.M. (2000) Patterning Electro-osmotic Flow with Patterned Surface Charge. *Physical Review Letters*, 84(15), pp. 3314–3317.

Suzuki, H., Ho, C.M. and Kasagi, N. (2004) A chaotic mixer for magnetic bead-based micro cell sorter. *Journal of Microelectromechanical Systems*, 13(5), pp. 779–790.

Tabeling, P. (2007) Introduction to Microfluidics. *Oxford University Press*, pp. 1–312.

Talbot, L. (1954) Laminar Swirling Pipe Flow. *Journal of Applied Mechanics*, 21(1), pp. 1–7.

Tandon, V., Bhagavatula, S.K., Nelson, W.C. and Kirby, B.J. (2008) Zeta potential and electroosmotic mobility in microfluidic devices fabricated from hydrophobic polymers: 1. The origins of charge. *Electrophoresis*, 29(5), pp. 1092–1101.

Tian, W.-C. and Finehout, E. (2008) Microfluidic Systems for Cellular Applications. In: *Microfluidics for Biological Applications*. Boston, MA: Springer US, pp. 185–221.

Usefian, A., Bayareh, M., Shateri, A. and Taheri, N. (2019) Numerical study of electro-osmotic micro-mixing of Newtonian and non-Newtonian fluids. *Journal of the Brazilian Society of Mechanical Sciences and Engineering*, 41(5), p. 238.

Vasista, K.N., Mehta, S.K. and Pati, S. (2022) Electroosmotic mixing in a microchannel with heterogeneous slip dependent zeta potential. *Chemical Engineering and Processing - Process Intensification*, 176, p. 108940.

Villermaux, E., Stroock, A.D. and Stone, H.A. (2008) Bridging kinematics and concentration content in a chaotic micromixer. *Physical Review E*, 77(1), p. 015301.

Wang, H., Iovenitti, P., Harvey, E.C. and Masood, S. (2003) Passive mixing in microchannels by applying geometric variations. In *Microfluidics, BioMEMS, and Medical Microsystems*, 4982, pp. 282-289. SPIE.

Wang, J., Wang, J., Feng, L. and Lin, T. (2015) Fluid mixing in droplet-based microfluidics with a serpentine microchannel. *RSC Advances*, 5(126), pp. 104138–104144.

Whitesides, G.M. (2006) The origins and the future of microfluidics. *Nature*, 442(7101), pp. 368–373.

Whittaker, E.T. (1903) An expression of certain known functions as generalized hypergeometric functions. *Bulletin of the American Mathematical Society*, 10(3), pp. 125–134.

Wong, S.H., Ward, M.C. and Wharton, C.W. (2004) Micro T-mixer as a rapid mixing micromixer. *Sensors and Actuators B: Chemical*, 100(3), pp. 359–379.

Yao, S. and Fang, T. (2012) Analytical solutions of laminar swirl decay in a straight pipe. *Communications in Nonlinear Science and Numerical Simulation*, 17(8), pp. 3235–3246.

Yazdi, A.A., Sadeghi, A. and Saidi, M.H., (2015) Electrokinetic mixing at high zeta potentials: Ionic size effects on cross stream diffusion. *Journal of Colloid and Interface Science*, 442, pp. 8–14.

Yu, S.C.M. and Kitoh, O. (1994) A general formulation for the decay of swirling motion along a straight pipe. *International Communications in Heat and Mass Transfer*, 21(5), pp. 719–728.

Zaccone, A., Wu, H., Gentili, D. and Morbidelli, M. (2009) Theory of activated-rate processes under shear with application to shear-induced aggregation of colloids. *Physical Review E*, 80(5), p. 051404.

Zhang, J. and Kuo, X. (2018) Mixing Performance of a 3D Micro T-Mixer with Swirl-Inducing Inlets and Rectangular Constriction. *Micromachines*, 9(5), p. 199.

Zhang, J.W., Li, W.F., Xu, X.L., Liu, H.F. and Wang, F.C. (2019) Experimental investigation of three-dimensional flow regimes in a cross-shaped reactor. *Physics of Fluids*, 31(3).

Zhao, C. and Yang, C. (2011) Electro-osmotic mobility of non-Newtonian fluids. *Biomicrofluidics*, 5(1).

LIST OF PUBLICATIONS

Publications from the Present Thesis:

1. **Kumar, D.**, Mehta, S. K., and Mondal, P. K. (2024) Non-Newtonian solute mixing via protonic exchange of Polyelectrolyte layer: Unveiling formation of electroosmotic vortices, ***Soft Matter*** [**Revised Manuscript Under Review**].
2. **Kumar, D.**, and Mondal, P. K. (2024) Mixing of inelastic non-Newtonian fluids with inlet swirl, ***Journal of Fluid Mechanics*** 997, A20.
3. **Kumar, D.**, Mehta, S. K., and Mondal, P. K. (2023) Enhanced bio-fluids mixing by the soft polyelectrolyte layer-modulated electroosmotic vortices. ***Physics of Fluids*** 35(7), 072019.
4. **Kumar, D.**, Gaikwad, H. S., Kaushik, P., and Mondal, P. K. (2023) Swirl driven solute mixing in narrow cylindrical channel. ***Physics of Fluids*** 35(6), 063604.

Other Publication:

A: Journal Publications

1. Mehta, S. K., **Kumar, D.**, Mondal, P. K., and Wongwises, S. (2024) Characterisation of conjugate forced convection in a wavy solar power plant: The role of porous metallic blocks. ***Chemical Engineering and Processing - Process Intensification*** 196, 109615.
2. Mehta, S. K., **Kumar, D.**, Mondal, P. K., and Wongwises, S. (2023) Characterization of thermal-hydraulics in wavy solar power plant: effect of thermal dispersion. ***Microsystem Technologies*** 12(1).

B: Conference Publications/Book Chapters

1. **Kumar, D.**, and Mondal, P. K. (2024) Influence of Axial Wall Slip on Swirl Velocity in a Laminar Microtube Flow, ***in Springer, Singapore***, pp 333–345.
2. **Kumar, D.**, and Mondal, P. K. (2023) Numerical Investigation of Swirl flow in Enhancement of Mixing in Narrow Channel, ***in Springer, Singapore***, pp 91–96.